

UNIVERSIDADE DE SÃO PAULO

INSTITUTO DE FÍSICA

Hidrodinâmica Evento-por-evento para o LHC

Meera Vieira Machado

Orientador: Prof.^a Dra. Frederique Marie Brigitte Sylvie Grassi

Dissertação de Mestrado apresentada ao Instituto de Física, Universidade de São Paulo, para a obtenção do título de Mestre em Ciências

Banca Examinadora:

Prof.^a Dra. Frederique Marie Brigitte Sylvie Grassi (IFUSP)

Prof. Dr. Fernando Silveira Navarra (IFUSP)

Prof.^a Dra. Sandra dos Santos Padula (IFT/UNESP)

São Paulo
2015

FICHA CATALOGRÁFICA
Preparada pelo Serviço de Biblioteca e Informação
do Instituto de Física da Universidade de São Paulo

Machado, Meera Vieira

Hidrodinâmica evento-por-evento para o LHC / Event-by-event hydrodynamics for LHC. São Paulo, 2015.

Dissertação (Mestrado) – Universidade de São Paulo.
Instituto de Física. Depto. Física Matemática.

Orientador: Profa. Dra. Frederique Grassi

Área de Concentração: Física de Altas Energias.

Unitermos: 1. Hidrodinâmica; 2. LHC; 3. Colisões de íons pesados; 4. Evento-por-evento.

USP/IF/SBI-078/2015

UNIVERSIDADE DE SÃO PAULO

INSTITUTO DE FÍSICA

Event-by-event Hydrodynamics for LHC

Meera Vieira Machado

Supervisor: Prof. Dr. Frederique Marie Brigitte Sylvie Grassi

Masters dissertation submitted to the Physics
Institute, University of São Paulo, in partial fulfillment
of the requirements for the degree of Master of Sciences

Examination Committee:

Prof. Dr. Frederique Marie Brigitte Sylvie Grassi (IFUSP)

Prof. Dr. Fernando Silveira Navarra (IFUSP)

Prof. Dr. Sandra dos Santos Padula (IFT/UNESP)

São Paulo
2015

Acknowledgments

First and foremost, I would like to thank my parents Maria Zuleide Vieira de Sousa and José Wagner Borges Machado and my grandmother Rosa Vieira de Sousa for the endless support on my studies. Secondly, to Elmar van Cleynenbreugel, for providing me with love and friendship through the last two years. I am also grateful for my family in Brasília and Ceará, for giving me courage and be always there rooting for me, even being so far away. I appreciate the long term support and companionship of my friends in Brasilia, who have been with me through my child and adulthood, always offering a hand whenever I needed help.

From São Paulo, I would like to thank my friends in the Mathematical Physics Department (IFUSP), specially Arthur Eduardo da Mota Loureiro, for providing me with new insights in physics and even philosophy of science and being the closest I had to a family in this city. I am grateful to Thiago Razseja, Javier Lorca, Pablo Ibieta and Alessandra Brognára for their friendship when we had all just arrived.

I thank my office colleagues Leonardo de Avellar and Tania Torrejon for the interesting discussions on physics and other matters and for coping with me through these years.

I thank my supervisor, Prof. Dr. Frederique Grassi, for being patient and orienting me through this whole process, thus providing me with way more knowledge on science research than I had before. I also thank Professor Fernando Gardim and Dr. Danuce Dudek for the numerous discussions on the NexSPheRIO code, which helped a lot with my research. My thanks to Dr. Jacquelyn Noronha-Hostler, who not only provided me with her numerical codes, but also taught me a lot about harmonic flows and other observables. I am grateful to Prof. Sandra Padula for adding me to her IFT project so that I could make also use of UNESP's computational power. I thank Prof. Yojiro Hama for the brief, yet useful discussions on heavy-ion collisions and Prof. Wei-Liang Qian for helping me with NexSPheRIO.

I am truly grateful for the numerical support team of IFUSP, Prof. Jorge de Lyra and João Borges, without whom I would not have been able to perform such extensive numerical calculations and the NCC and Grid-UNESP personnel, for letting me use their computational power to also run the NexSPheRIO code.

I would also like to thank the Mathematical Physics Department's secretaries Amelia Genova, Cecilia Blanco and Simone Shinomiya for having done so much for me during all those years, as well as the CPG-IFUSP personnel, specially Andrea Wirkus, Éber De Patto Lima, Paula Mondini and Cláudia Conde for the attention and help with all the necessary procedures.

At last, I thank CNPq for the financial support.

Resumo

É feita uma análise de hidrodinâmica evento-por-evento para colisões de Pb-Pb à energia incidente de $\sqrt{s_{NN}} = 2.76$ TeV. Estudamos os efeitos de duas equações de estado sob as mesmas condições iniciais e desacoplamento: uma é caracterizada por um ponto crítico e a outra é baseada em cálculos de Lattice QCD (Cromodinâmica Quântica). Os observáveis de interesse são os espectros de partículas em termos da pseudo rapidez e momento transversal, assim como os coeficientes harmônicos de Fourier que, por sua vez, carregam as anisotropias iniciais do sistema durante toda a sua evolução. Tais observáveis são calculados e comparados com dados experimentais do Large Hadron Collider (LHC). Por fim, os cálculos baseados em parâmetros referentes às energias do LHC são comparados com trabalhos anteriores feitos com base em dados experimentais do Relativistic Heavy-Ion Collider (RHIC). Os principais métodos usados no caso anterior são aplicados a este trabalho, o que resulta em algumas diferenças entre os resultados dos dois tipos de colisão, desde a distribuição de energia inicial a temperaturas de freeze-out.

Abstract

We perform an event-by-event hydrodynamic analysis for Pb-Pb collisions at the incident energy of $\sqrt{s_{NN}} = 2.76$ TeV, also studying the effects of two equations of state under the same initial conditions and freeze-out scenario: one characterized by a critical point and the other based on Lattice QCD (Quantum Chromodynamics) calculations. The observables of interest are particle spectra in terms of pseudorapidity and transverse momentum, as well as flow harmonics, which are coefficients that carry information on the initial anisotropies of the system throughout its evolution. Those are computed and compared with experimental Large Hadron Collider (LHC) data. There are slight differences in the results for each equation of state, caused by their distinct features. Lastly, the LHC-based calculations are compared with previous works related to the Relativistic Heavy-Ion Collider (RHIC) experimental data. The main techniques of the latter are performed in this work, which results in differences between some aspects in the outcome for each collision type, from initial energy distributions to freeze-out temperatures.

Summary

1	Introduction	1
2	Hydrodynamics and the Collision	3
2.1	The Equations of Motion	3
2.2	Initial Conditions	6
2.3	Equations of State	8
2.3.1	Equation of State with Critical Point (CPEoS)	8
2.3.2	Lattice QCD Equation of State (LattEoS)	15
2.3.3	Comparison between EoS	17
2.4	Cooper-Frye Decoupling Mechanism	18
3	On NexSPheRIO	21
3.1	The SPH Method	21
3.2	Decoupling in SPH	27
3.3	The Code's Structure	28
4	Results	30
4.1	Centrality Classes	30
4.2	Particle Spectra	32
4.2.1	Pseudorapidity Distribution	33
4.2.2	Transverse Momentum Distribution	36
4.3	Flow Analysis	39
4.3.1	Event Plane Method	40
4.3.2	Results	40
4.4	Comparison with RHIC	50
5	Conclusion	56
A	Energy-momentum Tensor in any Reference Frame	58
B	Coordinates in Heavy-Ion Collisions	60
C	Relativistic Fluid's Action in a General Coordinate System	62
	References	67

Chapter 1

Introduction

The Big Bang theory is one of the most accepted explanations to the beginning of the Universe. Proposed by LeMaître, the latter would have expanded from a state of high energy density and extreme temperatures. Due to said conditions and the relative small distances, it is believed that millionths of seconds after the Big Bang, quarks and gluons were asymptotically free. Such state of matter is denoted Quark-Gluon Plasma. In the year of 2000, the European Organization for Nuclear Research (CERN) officially announced[1] that compelling evidence for the existence of a new state of matter had been found. This followed the analysis of many experimental data collected during 15 years of heavy-ion experiments at the Super Proton Synchrotron (SPS).

In the same year, the Relativistic Heavy-Ion Collider (RHIC) started accelerating gold atoms to a center-of-mass energy several times higher than before, reaching up to 200 AGeV in the following years. Later on, Brookhaven National Laboratory claimed to have come upon a medium where the relevant degrees of freedom, over nuclear volumes, are those of quarks and gluons, rather than of hadrons[2]. Such is the Quark-Gluon Plasma, a strongly interacting low viscosity fluid.

Built to smash lead atoms at even higher energies (2.76 ATeV) than its predecessors, the Large Hadron Collider (LHC) is the present of ultra-relativistic heavy ion collisions. Studies of the experimental data collected by the ALICE (A Large Ion Collider Experiment), CMS (Compact Muon Solenoid) and ATLAS (A Toroidal LHC Apparatus) detectors should give new insight on the QGP properties and perhaps even give signs of new physics.

When studying the collisions of heavy-ions, one should analyze each step separately. First the nuclei collide at relativistic energies, meaning that they are Lorentz contracted in the beam direction by a factor of $\gamma = (1 - v^2)^{-1/2}$, where v is their velocity in the laboratory frame. At such extreme temperature and energy density values, the Quark-Gluon Plasma is thus formed. The great pressure difference between its core and the vacuum surrounding it makes the QGP suffer an explosive collective expansion, eventually undergoing a phase transition to a pure hadronic state as the temperature cools down. At last, the produced hadrons reach the detectors, which is the only piece of concrete information that theoreticians and experimentalists have to study the whole evolution that precedes this final moment.

Reconstructing the steps of a heavy-ion expansion is no easy task and many models have been formulated throughout the years. Enrico Fermi was the first to propose the fruitful idea

of considering the formed matter in thermal equilibrium and apply statistical methods to its study[3]. His model was based on the statistical weights of each particle species and it failed to explain the high abundance of pions in relation to kaons. Following the former's main idea on thermal equilibrium, Landau suggested that matter expands according the hydrodynamic equations of motion before hadron emission occurs[4, 5]. From then on, the latter has been extensively applied in the realm of relativistic heavy-ion collisions, alongside with models of initial conditions, equations of state and freeze-out scenarios.

In this work we apply event-by-event hydrodynamics to simulate Pb-Pb collisions at $\sqrt{s_{NN}} = 2.76$ TeV and compare the resultant observables with LHC data from the ALICE, CMS and ATLAS detectors. We begin by presenting the necessary ingredients for the calculation: first, we outline the hydrodynamic equations of motion in section 2.1, followed by an analysis of the initial conditions generated by Nexus[6] at such high energies. Two equations of state are then discussed as well as the system's freeze-out mechanism.

With the main parts set, we proceed on employing the Smoothed-Particle Hydrodynamics (SPH) method to solve the hydrodynamic equations of motion using the variational principle. The aforementioned is the core of the **S**moothed-**P**article **h**ydrodynamic evolution of **R**elativistic Heavy-**I**On collisions (SPheRIO)[7, 8] numerical code; its outline is the subject of section 3.3.

Finally, we compare the results to some heavy-ion collision observables, such as charged particle production in terms of pseudorapidity and transverse momentum as well as flow anisotropies, lastly comparing them with previous works on RHIC, where we discuss the main similarities and differences between them.

Chapter 2

Hydrodynamics and the Collision

2.1 The Equations of Motion

It was previously stated that relativistic hydrodynamics can describe the dynamics of the expansion that follows a heavy-ion collision, due to the collective behavior of the produced matter. Hydrodynamics is a long-distance description of what can be either a classical or a quantum many-body system [9]. Therefore, the phenomena considered in such dynamics are macroscopic, meaning that a fluid is seen as a continuous medium [10]. Any infinitesimal fluid element is still large compared to the distance between the molecules in it. That is the continuum hypothesis. Such assumption implies that the typical scale of the hydrodynamic variables is way larger than the microscopic scale defined by the interactions between the fluid components[11]. Local thermodynamic equilibrium, the condition upon hydrodynamic relies, may thus prevail[12].

In order to obtain the equations of motion of relativistic hydrodynamics, it is necessary to inquire deeper into the conservation laws governing it. According to Noether's theorem, continuous symmetries in a theory lead to conserved quantities, which imply the existence of conserved currents [9]. For the case at hand, there is symmetry in spacetime translation, which leads to the conservation of total energy and momentum, whose associated conserved currents are the energy-momentum tensor $T^{\mu\nu}$. Additionally, the fluid may carry other conserved quantities such as baryon number or charge [13]. In the relativistic case, the number of particles is not conserved, since the energy is high enough for particle creation and annihilation to occur. The conservation of baryon number, for instance, leads to the conserved current J^μ . Thus we shall have:

$$\partial_\mu T^{\mu\nu} = 0, \tag{2.1}$$

$$\partial_\mu J^\mu = 0. \tag{2.2}$$

These are the conservation laws of a system described by relativistic hydrodynamics.

We shall consider the fluid in Minkowski space with metric $\eta^{\mu\nu} = \text{diag}(1, -1, -1, -1)$ as well as $c = \hbar = k_b = 1$. Its 4-velocity is defined by $u^\mu = \frac{dx^\mu}{d\tau}$, where τ is the proper time and $x^\mu(\tau)$ is the trajectory of the fluid element. Hence, taking $u^\mu = (u^0, \vec{u})$ we must have:

$$\begin{aligned}
u^0 &= \frac{dx^0}{d\tau} = \gamma, \\
\vec{u} &= \frac{d\vec{x}}{d\tau} = \gamma\vec{v},
\end{aligned} \tag{2.3}$$

where $\gamma = \frac{1}{\sqrt{1-v^2}}$ is the Lorentz Factor and \vec{v} is the velocity of a fluid element with respect to the laboratory rest frame. Consequently, the fluid velocity is normalized, $u^\mu u_\mu = u_0^2 - \vec{u}^2 = 1$.

As it was previously mentioned, the assumption of local thermodynamic equilibrium is valid for the system at hand. That means the fluid element has isotropic properties in its rest frame. For instance, energy and momentum flux are zero. A nonzero current would define a direction in space, violating isotropy [11, 12]. In ideal hydrodynamics, baryon flux must be zero in the proper frame[12].

We define the conserved current $J^\mu = (n^0, \vec{n})$, with n^0 as the baryon number density and \vec{n} as the baryon flux. If n is the baryon number density in the fluid's rest frame, then $J_{RF}^\mu = (n, 0)$. In order to obtain J^μ in a moving frame, it is necessary to do a Lorentz Transformation:

$$J^\mu = \Lambda^\mu_\nu J_{RF}^\nu. \tag{2.4}$$

Since $\Lambda^\mu_\nu = \frac{\partial x'^\mu}{\partial x^\nu}$:

$$\begin{aligned}
\Lambda^0_0 &= \gamma & \Lambda^i_0 &= \gamma v^i \\
\Lambda^0_j &= -\gamma v_j & \Lambda^i_j &= \delta_{ij} + v_i v_j \frac{\gamma - 1}{v^2},
\end{aligned} \tag{2.5}$$

with Λ^0_j and Λ^i_j conveniently chosen[13]. Therefore:

$$\begin{aligned}
J^0 &= \Lambda^0_\nu J_{RF}^\nu = \Lambda^0_0 J_{RF}^0 + \Lambda^0_i J_{RF}^i = \gamma n, \\
J^i &= \Lambda^i_\nu J_{RF}^\nu = \Lambda^i_0 J_{RF}^0 + \Lambda^i_j J_{RF}^j = \gamma n v^i, \\
\Rightarrow J^\mu &= (\gamma n, \gamma n v^i) \\
\Rightarrow J^\mu &= n u^\mu.
\end{aligned} \tag{2.6}$$

From $\partial_\mu J^\mu = 0$ and equation (2.6) above:

$$\begin{aligned}
\partial_\mu J^\mu &= \partial_\mu n u^\mu = 0, \\
\frac{\partial(n\gamma)}{\partial t} + \nabla \cdot (n\gamma\vec{v}) &= 0,
\end{aligned} \tag{2.7}$$

which is the continuity equation.

It is worth remarking that $J^\mu = n u^\mu$ is the simplest 4-vector we can write with the quantities n and u^μ , without accounting for their derivatives.

The conserved currents associated with energy-momentum conservation can be written as a tensor $T^{\mu\nu}$, where each value of ν indicates a component of the 4-momentum and μ corresponds to components of the conserved current [12]. Having established that, T^{00} becomes the energy density, T^{0j} is the momentum density, T^{i0} the energy flux along axis i and T^{ij} forms the momentum flux density tensor – also known as pressure tensor [10, 12].

Firstly, we shall define $T^{\mu\nu}$ in the fluid's proper frame. The components associated with momentum density and energy flux, T^{0j} and T^{i0} , thus disappear. $T^{00} = \epsilon$, where ϵ is the proper energy density. Since Pascal's Law is valid in this case, $T^{ij}da_j$ – momentum flux through a surface element da_j – equals the pressure acting in such surface, Pda_j . Hence, $T^{ij} = P\delta^{ij}$ and $T^{\mu\nu}$ acquires the form:

$$T_{RF}^{\mu\nu} = \begin{pmatrix} \epsilon & 0 & 0 & 0 \\ 0 & P & 0 & 0 \\ 0 & 0 & P & 0 \\ 0 & 0 & 0 & P \end{pmatrix}. \quad (2.8)$$

Secondly, consider an inertial frame in which the fluid appears to be moving with velocity \vec{v} . Under a Lorentz transformation $T^{\mu\nu}$ shall be written as:

$$T^{\mu\nu} = \Lambda^\mu_\alpha \Lambda^\nu_\beta T_{RF}^{\alpha\beta}. \quad (2.9)$$

Using equations (2.5) in the expression above (see Appendix A), we finally arrive at $T^{\mu\nu}$'s expression for ideal fluids at an arbitrary speed, \vec{v} :

$$T^{\mu\nu} = (\epsilon + P)u^\mu u^\nu - P\eta^{\mu\nu}. \quad (2.10)$$

It is worth noticing that $T^{\mu\nu} = T^{\nu\mu}$.

Under the perfect fluid hypothesis, the energy-momentum tensor and baryonic current take the forms depicted as equations (2.6) and (2.10). $\epsilon = \epsilon(x)$, $P = P(x)$, $u^\mu = u^\mu(x)$ and $n = n(x)$ are promoted to slowly varying fields. Additionally, an equilibrium equation of state supplies one with $P(T, \mu)$, from which the thermodynamic relations $s = \frac{\partial P}{\partial T}$, $n = \frac{\partial P}{\partial \mu}$ and $\epsilon = -P + Ts + \mu n$ evaluate ϵ, n and s – entropy density [9].

Given equation (2.1), the projection of $T^{\mu\nu}$ in the four-velocity's direction shall be $u_\nu \partial_\mu T^{\mu\nu} = 0$. Thus:

$$u_\nu \partial_\mu [(\epsilon + P)u^\mu u^\nu] - u_\nu \partial_\mu P \eta^{\mu\nu} = 0$$

Recalling that $u^\mu u_\mu = 1$,

$$\partial_\mu [(\epsilon + P)u^\mu] + (\epsilon + P)u^\mu u_\nu \partial_\mu u^\nu - u^\mu \partial_\mu P = 0$$

Since $u_\nu \partial_\mu u^\nu = 0$, one shall have:

$$\begin{aligned} \partial_\mu (\epsilon + P)u^\mu + (\epsilon + P)\partial_\mu u^\mu - u^\mu \partial_\mu P &= 0 \\ \Rightarrow u^\mu \partial_\mu \epsilon + (\epsilon + P)\partial_\mu u^\mu &= 0 \\ \Rightarrow u^\mu \partial_\mu (-P + Ts + \mu n) + (Ts + \mu n)\partial_\mu u^\mu &= 0. \end{aligned}$$

Equation (2.2) and $\partial_\mu P = s\partial_\mu T + n\partial_\mu \mu$ yield:

$$\begin{aligned} T(u^\mu \partial_\mu s + s\partial_\mu u^\mu) &= 0 \\ \Rightarrow \partial_\mu (su^\mu) &= 0, \end{aligned} \tag{2.11}$$

which is the conservation of entropy density current, $s^\mu = su^\mu$. Locally, entropy does not increase in ideal hydrodynamics [9]. Hence:

$$\partial_\mu T^{\mu\nu} = 0 \quad \partial_\mu J^\mu = 0$$

with the conserved currents defined as:

$$\begin{aligned} J^\mu &= nu^\mu \\ T^{\mu\nu} &= (\epsilon + P)u^\mu u^\nu - P\eta^{\mu\nu} \end{aligned}$$

consist in the Equations of Motion of Relativistic Ideal Hydrodynamics (EoM). Combined with the equation of state, $P(T, \mu)$ they form a closed system of equations.

2.2 Initial Conditions

The first stage in solving the hydrodynamic equations is setting their initial (IC) and boundary conditions. The latter demand that energy density and other thermodynamic variables tend to zero at large distances from the collision center or, in the case of a boost-invariant system, the collision axis[14].

When the nuclei collide, particles are created and they interact with each other through complex processes not completely understood. One then assumes that the system eventually reaches local thermodynamic equilibrium, since hydrodynamics strongly relies on such assumption. Having said that, $T^{\mu\nu}$, J^μ and u^μ generated by this microscopic dynamic may not coincide with those of local equilibrium. Thus, one shall define the local fluid rest frame by solving the following eigenvalue equation:

$$T^{\mu\nu} u_\nu = \epsilon u^\mu, \tag{2.12}$$

where u^μ is a normalized time-like eigenvector and ϵ the associated eigenvalue[15, 16]. The baryon density (and other number densities) in this frame can be calculated by contracting its respective current with the four-velocity:

$$n = J^\mu u_\mu.$$

Finally, the remaining thermodynamic quantities are obtained using the equation of state.

The assumption of *highly symmetric and smooth IC* was commonly used for many years in high-energy nuclear collisions. However, the system's finite size implies in large fluctuations varying from event to event at its initial stage. Their effects on observables – in particular, elliptic flow (Chapter 4) – were firstly accounted for by the NexSPheRIO group[16]. The

use of such fluctuating IC became mandatory with the observation of higher order flows (see Chapter 4), notably triangular flow, as suggested in [17, 18], their appearance from a wide range of centralities[19, 20] to even the most central collisions[21, 22] as well as factorization breaking[23], structures in two-particle correlations[24, 25], etc. This new approach is called *event-by-event hydrodynamics*.

In the event-by-event method, one solves the hydrodynamic EOM for each event and calculates the observables, taking their mean value at the end. This closely mimics what is done experimentally.

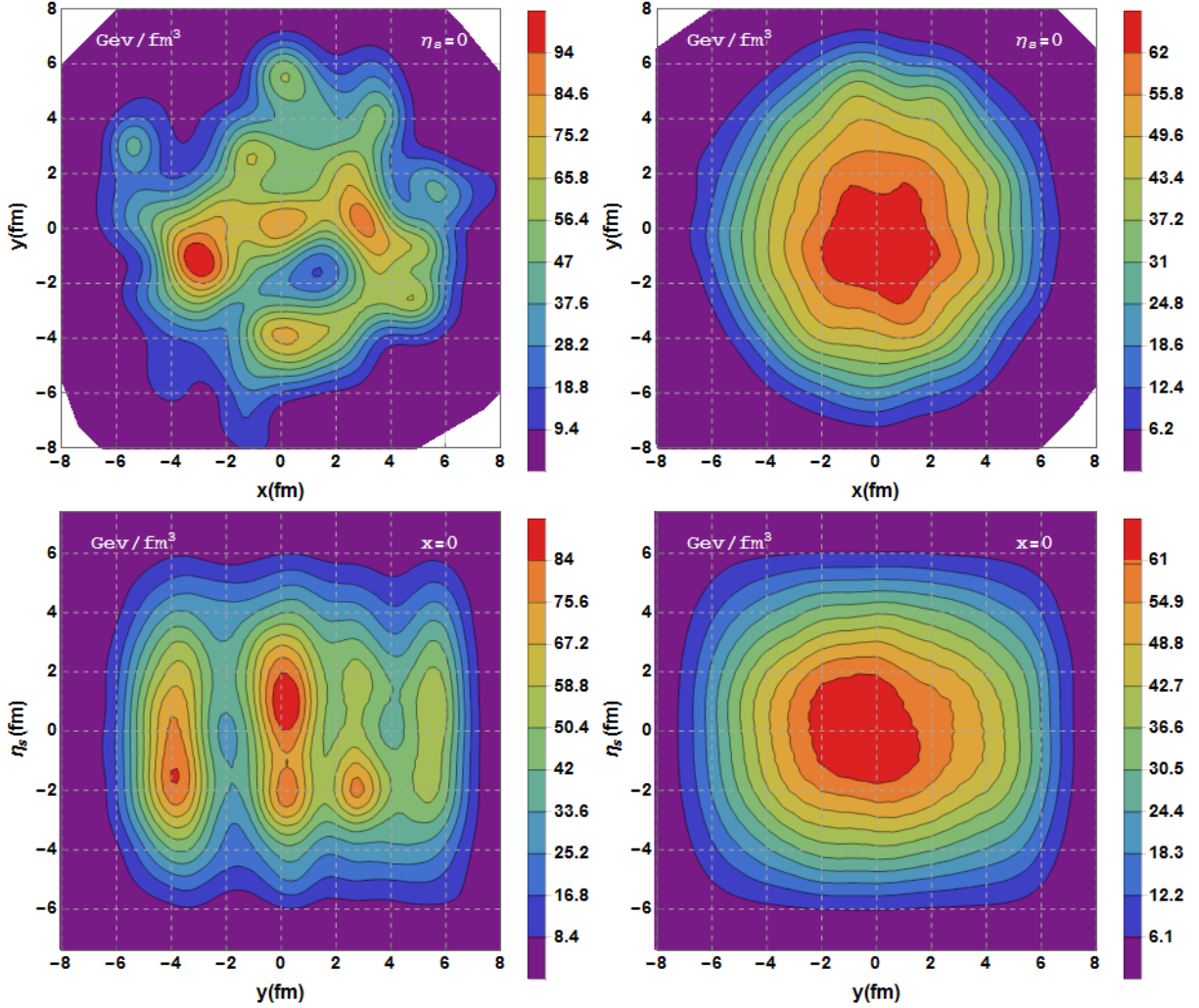


Figure 2.1: Initial conditions generated by Nexus[6] for central Pb-Pb collisions at 2.76A TeV. **Top:** energy density (in GeV/fm^3) measured in the transverse plane ($\eta_s = 0$) for one random event (left) and an average over 100 random ones (right). **Bottom:** energy density measured in the longitudinal plane ($x = 0$) for the same random event (left) and the average over 100 events (right).

In this work, we take the Nexus[6] event generator and adopt the event-by-event approach. The former is based on the effective field theory of Regge-Gribov, where the multiple interactions happening between hadrons are represented by exchanging phenomenological objects called *Pomerons*. The aforementioned Nexus code gives as output the energy-momentum tensor $T^{\mu\nu}(x)$, alongside with u^μ and the conserved currents $J_B^\mu(x)$, $J_Q^\mu(x)$ and $J_S^\mu(x)$, where B ,

S and Q represent baryon number, strangeness and electric charge, respectively. It provides the said quantities at a certain time τ_0 , when the system is supposedly in equilibrium and hydrodynamics dictates its evolution. In this work we take $\tau_0 = 1$ fm.

Figure 2.1 shows examples of energy densities of both single-event IC (left side) and smoothed ones (right side) for a central Pb+Pb collision at 2.76A TeV, where $\eta_s = \frac{1}{2} \ln(\frac{t+z}{t-z})$ is the space-time rapidity, which we shall discuss in more detail in Appendix B. It is worth noticing that the smoothed IC are an average over many single-events and an approximation of what was done prior to event-by-event calculations.

When taking the energy density graphs portrayed on the left side of Fig.2.1, it is easy to see the fluctuations characteristic of a single-event IC. Those are, in fact, due to geometrical fluctuations in the distribution of nucleons, as well as particle production resultant of collisions[6]. The right side, on the other hand, shows most of the energy concentrated on the center with its value decreasing continuously the further one goes to the edge. As previously mentioned, such fluctuations will carry their effects on the subsequent computations of observables.

We should remark that the **Nexus** code has an upper limit for the incident energy of colliding nuclei – caused by computational limitations –, which was found to be 2 TeV. However, it is rather simple to scale the 2 TeV IC to the actual LHC beam energy of 2.76 TeV, as we shall discuss in Chapter 4.

2.3 Equations of State

An equation of state (EoS) is defined as a functional relation between thermodynamic variables characterizing a medium[12]. In the realm of heavy-ion collisions, those quantities ϵ , P , T , μ_B , etc., which are representative of the hot and dense produced matter, cannot be directly measured. Hence, different EoS are used in the model calculations in order to determine the one that coherently reproduces the observables, thus leading to a correct description of the data[14, 26].

In this work we adopt two distinct EoS: the first is a parametrization with a critical point of a first-order phase transition equation of state (CPEoS)[16, 26], whereas the second is inspired in Lattice Quantum Chromodynamics results (LattEoS)[27]. The next step consists in a discussion of both EoS, followed by a comparison between them.

2.3.1 Equation of State with Critical Point (CPEoS)

The title's equation of state was primarily developed in [16] as a first-order phase transition type, which connected a high-temperature QGP phase with a low-temperature hadronic one. Later on, a critical end point was implemented in [26] with the purpose of incorporating what was then known about quark-hadron phase transition. The EoS was defined for $\mu \neq 0$.

With the quark-gluon plasma's cooling, the system reaches a confined phase where the degrees of freedom are bound states of quarks and gluons, usually hadrons[28]. Due to the non-perturbative nature of such system, describing its dynamics is no trivial task. In the regime of high energies, however, one may treat the particles and its interactions as a quantum ideal

gas[16]. By virtue of the wave function's symmetry properties, the former's quantum state is fully characterized by the set of occupation numbers[29]:

$$\{\bar{n}_1, \bar{n}_2, \dots, \bar{n}_j, \dots\} \equiv \{\bar{n}_j\}, \quad (2.13)$$

where \bar{n}_j represents the number of particles in orbital j . In the case of fermions, $\bar{n}_j = 0$ or 1, while for bosons, \bar{n}_j could assume any value from 0 to N , with N as the total number of particles. The energy of said system is given by:

$$E = \sum_j \varepsilon_j \bar{n}_j. \quad (2.14)$$

Taking the context of the grand canonical ensemble, which represents a system in thermodynamic equilibrium, the grand partition function has the following expression:

$$\ln \Xi = \pm \sum_j \ln\{1 \pm \exp(-\beta(\varepsilon_j - \mu))\} \quad (2.15)$$

and the sum is over all single-particle quantum states. Additionally, the \pm represents the statistics of Fermi-Dirac (+) and Bose-Einstein (-) and $\beta = 1/T$. In the thermodynamic limit:

$$\ln \Xi = \pm g \frac{V}{(2\pi)^3} \int d^3p \ln\{1 \pm \exp(-\beta(\varepsilon(p) - \mu))\}, \quad (2.16)$$

where g is degeneracy factor, V the systems volume and $\varepsilon(p) = \sqrt{p^2 + m^2}$, with p as the momentum of the particle and m as its mass. In the aforementioned limit, the pressure of particle j at temperature T with chemical potential μ_j is given by:

$$P_j(T, \mu_j) = \pm \frac{1}{\beta} \lim_{V \rightarrow \infty} \frac{1}{V} \ln \Xi. \quad (2.17)$$

Thus,

$$P_j(T, \mu_j) = \frac{\pm g_j}{\beta(2\pi)^3} \int d^3p \ln\{1 \pm \exp(-\beta(\varepsilon_j(p) - \mu_j))\}. \quad (2.18)$$

Integrating in spherical coordinates:

$$P_j(T, \mu_j) = \frac{\pm g_j}{\beta(2\pi)^3} 4\pi \int_0^\infty p^2 \ln(1 \pm e^{-\beta(\varepsilon_j(p^2) - \mu_j)}) dp.$$

Integrating by parts shall yield the following result:

$$P_j(T, \mu_j) = \frac{g_j}{6\pi^2} \int_0^\infty \frac{p^4}{\sqrt{p^2 + m_j^2}} \frac{1}{e^{\beta(\varepsilon_j - \mu_j)} \pm 1} dp, \quad (2.19)$$

with m_j as the j -th particle's mass.

The total pressure of a hadron gas has the subsequent expression:

$$P_{HG}(T, \mu) = \sum_j P_j(T, \mu_j), \quad (2.20)$$

which is a sum over all particle species and resonances. In order to get a practical application to hydrodynamics, we set all number densities save the baryonic one to be null everywhere[16]. Hence, $\mu_j = B_j \mu_B$, with B as the baryon number. The equation above becomes:

$$P_{HG}(T, \mu_B) = \sum_j \frac{g_j}{6\pi^2} \int_0^\infty \frac{p^4}{\sqrt{p^2 + m_j^2}} \frac{1}{e^{\beta(\varepsilon_j - B_j \mu_B)} \pm 1} dp. \quad (2.21)$$

The baryon number is defined as $B = \frac{1}{3}(q - \bar{q})$, where q and \bar{q} represent the numbers of quark and anti-quarks respectively. For mesons, $B = 0$ whereas for baryons $-1 < B < 1$. It is also important to remark that mesons are bosons while baryons are fermions. Knowing that, we shall rewrite P_{HG} :

$$P_{HG}(T, \mu_B) = \sum_{\substack{j \\ \{\text{fermions}\}}} \frac{g_j}{6\pi^2} \int_0^\infty \frac{p^4}{\sqrt{p^2 + m_j^2}} \frac{1}{e^{\beta(\sqrt{p^2 + m_j^2} - B_j \mu_B)} + 1} dp \\ + \sum_{\substack{j \\ \{\text{bosons}\}}} \frac{g_j}{6\pi^2} \int_0^\infty \frac{p^4}{\sqrt{p^2 + m_j^2}} \frac{1}{e^{\beta\sqrt{p^2 + m_j^2}} - 1} dp. \quad (2.22)$$

From the analysis of thermal models, it becomes clear that the ideal gas approach requires a modification to adjust the size of the system[16]. Since the volume to fit the particle abundances is found to be small, one should then introduce the excluded-volume correction, represented by the coupled equations below[16]:

$$P_{HG}(T, \mu_B) = \sum_{j=1} P_j^{id}(T, \bar{\mu}_j), \quad (2.23)$$

$$\bar{\mu}_j \equiv \mu_j - v_j P_{HG}, \quad (2.24)$$

where v_j is the excluded volume of the j -th hadron species and $P_j^{id}(T, \bar{\mu}_j)$ corresponds to the pressure in expression (2.19). The remaining thermodynamic variables are calculated with the relations:

$$n_B = \left(\frac{\partial P_{HG}}{\partial \mu_B} \right)_{V,T} \\ = \sum_j \left(\frac{\partial P_j}{\partial \mu_B} \right) \\ = \sum_j B_j n_j, \quad (2.25)$$

with n_j as the j -th particle baryon number density. As for energy and entropy densities:

$$s = \frac{\partial P_{HG}}{\partial T}, \\ \epsilon = -P_{HG} + Ts + \mu n_B.$$

In regard to the resonances included in the hadron gas, all meson and baryon masses smaller than 1.5 GeV and 2 GeV, respectively, are taken into consideration. Resonance widths are not included[16]. We shall move on to the equation for the QGP phase.

Quantum Chromodynamics (QCD) is thought to possess two striking features: asymptotic freedom and confinement. The first dictates that particle interactions weaken at shorter distances. The second, on the other hand, states that quarks and gluons cannot be found as isolated objects. However, as energy and temperature increase, a phase transition may occur to a state where the degrees of freedom correspond to the color charged particles themselves [14]. Such stage is the aforementioned Quark-Gluon Plasma.

Taking the QCD properties cited above into consideration, the MIT Bag Model[30] assumes that quarks and gluons are asymptotically free inside hadrons, which is a simple approach to describe the latter's structure. It proposes that strongly interacting particles consist of fields confined to a finite region of space that possesses a constant positive potential energy per unit volume, \mathcal{B} [31]. One calls such region a bag. Boundary conditions ensure that fields vanish outside it.

This MIT Bag description of a hadron as fields confined to a volume V could be extended as means of computing an EoS for the QGP phase[16]. In that case, the QGP will be taken as an ideal quark-gluon gas restricted by V , with total energy given by[30]:

$$\begin{aligned} E &= E_r + \mathcal{B}V \\ \Rightarrow \epsilon &= \epsilon_r + \mathcal{B}, \end{aligned} \quad (2.26)$$

where E_r and ϵ_r are, respectively, the gas internal energy and energy density. Additionally, the pressure will take the form:

$$P = P_r - \mathcal{B}. \quad (2.27)$$

Combining the expression above with (2.21) will yield the following equation for QGP pressure:

$$P_{QGP} = \sum_j \frac{g_j}{6\pi^2} \int_0^\infty \frac{p^4}{\sqrt{p^2 + m_j^2}} \frac{dp}{e^{\beta(\sqrt{p^2 + m_j^2} - \mu_j)} \pm 1} - \mathcal{B}. \quad (2.28)$$

The sum is over gluons and *up*, *down* and *strange* quarks. One may write it more explicitly as:

$$\begin{aligned} P_{QGP} &= \sum_{\{u, \bar{u}, d, \bar{d}, s, \bar{s}\}} \frac{g_j}{6\pi^2} \int_0^\infty \frac{p^4}{\sqrt{p^2 + m_j^2}} \frac{dp}{e^{\beta(\sqrt{p^2 + m_j^2} - B_j \mu_B)} + 1} \\ &\quad + \frac{g_G}{6\pi^2} \int_0^\infty \frac{p^3}{e^{\beta p} - 1} dp - \mathcal{B}, \end{aligned} \quad (2.29)$$

where $g_j = 2 \times 3$ and $g_G = 2 \times 8$. Then, neglecting the masses of the *up* and *down* quarks,

$$\begin{aligned} P_{QGP} &= \sum_{\{u, \bar{u}, d, \bar{d}\}} \frac{g_j}{6\pi^2} \int_0^\infty \frac{p^3 dp}{e^{\beta(p - B_j \mu_B)} + 1} + \frac{g_G}{6\pi^2} \int_0^\infty \frac{p^3}{e^{\beta p} - 1} dp \\ &\quad + \sum_{\{s, \bar{s}\}} \frac{g_j}{6\pi^2} \int_0^\infty \frac{p^4}{\sqrt{p^2 + m_j^2}} \frac{dp}{e^{\beta(\sqrt{p^2 + m_j^2} - B_j \mu_B)}} - \mathcal{B}. \end{aligned} \quad (2.30)$$

In this work we adopt the bag constant value as $\mathcal{B} = 380 \text{ MeV}/\text{fm}^3$ [16].

As the Quark-Gluon Plasma cools down, confinement wins over and, consequently, the degrees of freedom correspond to the formed hadrons. The type of phase transition between QGP and HG varies with the value of μ [26, 32].

Let $\mu \sim 0$. Current QCD simulations with non-zero quark masses indicate the transition as an analytical crossover[33]. Put differently, at a certain temperature interval, the thermodynamic variables rapidly change without any singularities.

Consider now the opposite: μ is large and finite. Many works, like [32, 34], show that a first order phase transition should occur. Such is characterized by a sharper change, a “jump” (for example in energy density) from one state to another[26]. For the physical strange quark mass, the said transitions for varying μ must connect, suggesting the existence of a critical end point C in the phase diagram, with attributed μ_c and T_c values.

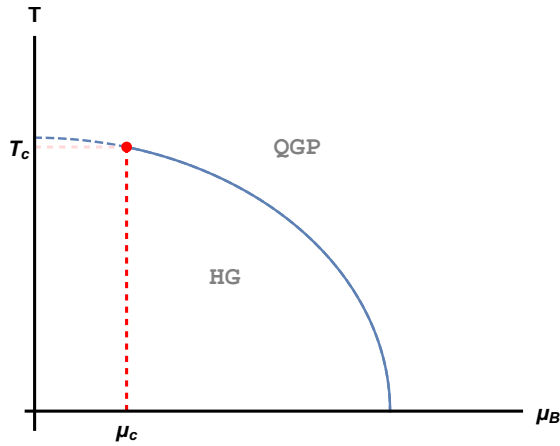


Figure 2.2: Illustrative μ_B - T phase diagram. Coordinate (μ_c, T_c) is the critical point, represented by the red dot. For $\mu_B < \mu_c$, the phase transition is of crossover type (dashed line); on the other hand, $\mu_B > \mu_c$, there is a first order phase transition (continuous line).

We introduce a phenomenological parameterization of the phase transition[26]:

$$(P - P_{QGP})(P - P_{HG}) = \delta(\mu_B), \quad (2.31)$$

with

$$\delta(\mu_B) = \delta_0 \exp \left[- \left(\frac{\mu_B}{\mu_c} \right)^2 \right]. \quad (2.32)$$

Combining both expressions above yields a second degree equation in P :

$$P^2 - (P_{QGP} + P_{HG})P + P_{QGP}P_{HG} - \delta(\mu_B) = 0,$$

with solutions:

$$P = \frac{1}{2} \left[(P_{QGP} + P_{HG}) \pm \sqrt{(P_{QGP} - P_{HG})^2 + 4\delta(\mu_B)} \right].$$

If $\mu_B \gg \mu_c$, $\delta(\mu_B)$ should approach 0. In that case, the solutions above would be $P = P_{QGP}$ (positive sign) and $P = P_{HG}$ (negative sign). As previously mentioned, for large values of μ_B , the phase transition should be of first order. Hence, $P_{HG}(T, \mu_B) = P_{QGP}(T, \mu_B)$ when both states are in equilibrium. When considering this situation, it is possible to choose either solution. For all subsequent calculations, we take the one with positive sign. Thus, by defining:

$$\lambda \equiv \frac{1}{2} \left[1 - \frac{(P_{QGP} - P_{HG})}{\sqrt{(P_{QGP} - P_{HG})^2 + 4\delta(\mu_B)}} \right], \quad (2.33)$$

one can write the pressure in terms of λ :

$$\begin{aligned} P &= \frac{1}{2} \left[-(P_{QGP} - P_{HG}) + 2P_{QGP} + \sqrt{(P_{QGP} - P_{HG})^2 + 4\delta(\mu_B)} \right] \\ &= \frac{1}{2} \sqrt{(P_{QGP} - P_{HG})^2 + 4\delta(\mu_B)} \left[1 - \frac{(P_{QGP} - P_{HG}) - 2P_{QGP}}{\sqrt{(P_{QGP} - P_{HG})^2 + 4\delta(\mu_B)}} \right] \\ &= \lambda \sqrt{(P_{QGP} - P_{HG})^2 + 4\delta(\mu_B)} + P_{QGP}. \end{aligned}$$

Adding and subtracting $\frac{2\delta(\mu_B)}{\sqrt{(P_{QGP} - P_{HG})^2 + 4\delta(\mu_B)}}$,

$$\begin{aligned} P &= P_{QGP} + \frac{2\delta(\mu_B)}{\sqrt{(P_{QGP} - P_{HG})^2 + 4\delta(\mu_B)}} + \lambda \sqrt{(P_{QGP} - P_{HG})^2 + 4\delta(\mu_B)} \\ &\quad - \frac{2\delta(\mu_B)}{\sqrt{(P_{QGP} - P_{HG})^2 + 4\delta(\mu_B)}} \\ &= P_{QGP} + \frac{2\delta(\mu_B)}{\sqrt{(P_{QGP} - P_{HG})^2 + 4\delta(\mu_B)}} + \frac{\lambda[(P_{QGP} - P_{HG})^2 + 4\delta(\mu_B)] - 2\delta(\mu_B)}{\sqrt{(P_{QGP} - P_{HG})^2 + 4\delta(\mu_B)}}. \end{aligned}$$

By using (2.33) and simplifying, one arrives at the following result:

$$P = \lambda P_{HG} + (1 - \lambda)P_{QGP} + \frac{2\delta(\mu_B)}{\sqrt{(P_{QGP} - P_{HG})^2 + 4\delta(\mu_B)}}. \quad (2.34)$$

In order to compute n_B , one must use the thermodynamic relation:

$$\begin{aligned} n_B &= \left(\frac{\partial P}{\partial \mu_B} \right)_T = \frac{\partial}{\partial \mu_B} (P_{HG} \lambda) + \frac{\partial}{\partial \mu_B} (1 - \lambda) P_{QGP} \\ &\quad + \frac{\partial}{\partial \mu_B} \left[\frac{2\delta(\mu_B)}{\sqrt{(P_{QGP} - P_{HG})^2 + 4\delta(\mu_B)}} \right]. \end{aligned} \quad (2.35)$$

We shall evaluate each term separately. Firstly:

$$\frac{\partial}{\partial \mu_B} (P_I \lambda) = \lambda n_I + P_I \frac{\partial \lambda}{\partial \mu_B},$$

where I could stand for either HG or QGP, and

$$\begin{aligned}\frac{\partial \lambda}{\partial \mu_B} &= -\frac{1}{2} \left\{ (n_{QGP} - n_{HG}) [(P_{QGP} - P_{HG})^2 + 4\delta(\mu_B)]^{-1/2} \right. \\ &\quad - \frac{1}{2} (P_{QGP} - P_{HG}) [2(P_{QGP} - P_{HG})(n_{QGP} - n_{HG}) \\ &\quad \left. + 4(-2)(\mu_B/\mu_c^2)\delta(\mu_B)] [(P_{QGP} - P_{HG})^2 + 4\delta(\mu_B)]^{-3/2} \right\}.\end{aligned}$$

Secondly, we take the derivative of the remaining term:

$$\begin{aligned}\frac{\partial}{\partial \mu_B} \left[\frac{2\delta(\mu_B)}{\sqrt{(P_{QGP} - P_{HG})^2 + 4\delta(\mu_B)}} \right] &= 2(-2) \left(\frac{\mu_B}{\mu_c^2} \right) \delta(\mu_B) [(P_{QGP} - P_{HG})^2 + 4\delta(\mu_B)]^{-1/2} \\ &\quad - \delta(\mu_B) \left[2(P_{QGP} - P_{HG})(n_{QGP} - n_{HG}) - 8 \left(\frac{\mu_B}{\mu_c^2} \right) \delta(\mu_B) \right] [(P_{QGP} - P_{HG})^2 + 4\delta(\mu_B)]^{-3/2}.\end{aligned}$$

Substituting the expressions above in (2.35) and simplifying shall result in:

$$n_B = \lambda n_{HG} + (1 - \lambda) n_{QGP} - \frac{2(\mu_B/\mu_c^2)\delta(\mu_B)}{\sqrt{(P_{QGP} - P_{HG})^2 + 4\delta(\mu_B)}}. \quad (2.36)$$

Knowing that $s = \frac{\partial P}{\partial T}$, we can compute the entropy density:

$$s = \frac{\partial}{\partial T} (P_{HG}\lambda) + \frac{\partial}{\partial T} (1 - \lambda) P_{QGP} + \frac{\partial}{\partial T} \left[\frac{2\delta(\mu_B)}{\sqrt{(P_{QGP} - P_{HG})^2 + 4\delta(\mu_B)}} \right] \quad (2.37)$$

We take each term's derivative separately:

$$\frac{\partial \lambda}{\partial T} = -\frac{1}{2} \left[\frac{(s_{QGP} - s_{HG})}{\sqrt{(P_{QGP} - P_{HG})^2 + 4\delta(\mu_B)}} - \frac{(P_{QGP} - P_{HG})(s_{QGP} - s_{HG})}{[(P_{QGP} - P_{HG})^2 + 4\delta(\mu_B)]^{3/2}} \right]$$

and

$$\frac{\partial}{\partial T} \left[\frac{2\delta(\mu_B)}{\sqrt{(P_{QGP} - P_{HG})^2 + 4\delta(\mu_B)}} \right] = \frac{(-2)\delta(\mu_B)(P_{QGP} - P_{HG})(s_{QGP} - s_{HG})}{[(P_{QGP} - P_{HG})^2 + 4\delta(\mu_B)]^{3/2}}.$$

By substituting in (2.37) and simplifying, we shall then have:

$$s = \lambda s_{HG} + (1 - \lambda) s_{QGP}. \quad (2.38)$$

Finally, we use $\epsilon = -P + Ts + \mu_B n_B$ to find the expression for energy density:

$$\epsilon = \lambda \epsilon_{HG} + (1 - \lambda) \epsilon_{QGP} - \frac{2[1 + (\mu_B/\mu_c)^2] \delta(\mu_B)}{\sqrt{(P_{QGP} - P_{HG})^2 + 4\delta(\mu_B)}}. \quad (2.39)$$

CPEoS is now complete and can be used as input in the EoM of hydrodynamics.

2.3.2 Lattice QCD Equation of State (LattEoS)

Lattice simulations of QCD are able to depict the dynamics of strongly interacting matter non-perturbatively. Hence, a lattice QCD-based equation of state should be a fundamental ingredient in the evolution of heavy ion collisions, particularly of the Quark-Gluon Plasma.

EoS computations on the lattice at finite temperatures are performed using a fixed temporal extent N_τ and the temperature is varied by changing lattice spacing $T = 1/(N_\tau a)$ [27]. Therefore, hadron masses, which are dependent on temperature, also alter with lattice spacing (a). Since with decreasing T , a increases, the result shows a discrepancy between lattice calculations and predictions of the hadron resonance gas (HRG) model – in this case, there is no excluded volume correction. Other differences arise due to the quark masses used in lattice QCD being a factor of two larger than the physical ones [27].

HRG model is an useful tool for studying the high number of particles produced in heavy ion collisions, up to a certain temperature limit. At the same time, lattice spacing for high T diminishes discretization errors, making lattice QCD calculations at such regime more accurate. The resulting EoS is an interpolation between hadron resonance gas at low T and lattice QCD at high T .

Energy and entropy density as well as pressure have their values computed by calculating the trace anomaly of the energy-momentum tensor, defined as $\Theta(T) \equiv T^{\mu\mu} = \epsilon - 3P(T)$. Alongside with $s = (\epsilon + P)/T$ for $n_B = 0$ (which is the case for the EoS at hand) and $s = \partial P/\partial T$, one should have:

$$\begin{aligned}\epsilon - 3P &= \Theta, \\ \epsilon + P &= T \frac{\partial P}{\partial T}.\end{aligned}$$

Subtracting one from the other:

$$\Theta = T \frac{\partial P}{\partial T} - 4P.$$

Multiplying by T^5/T^5 :

$$\begin{aligned}\Theta &= T^5 \frac{1}{T^4} \frac{\partial P}{\partial T} + T^5 P(-4) \frac{1}{T^5} \\ \Theta &= T^5 \frac{\partial(P/T^4)}{\partial T}.\end{aligned}\tag{2.40}$$

Hence, the pressure difference at temperatures T and T_{low} is expressed as the integral of the trace anomaly:

$$\frac{P(T)}{T^4} - \frac{P(T_{low})}{T_{low}^4} = \int_{T_{low}}^T \frac{dT'}{T'^5} \Theta(T').\tag{2.41}$$

If one chooses the lower integration limit sufficiently small, $P(T_{low})$ can be ignored due to exponential suppression. The remaining thermodynamic quantities, energy and entropy density are computed using $\epsilon(T) = \Theta(T) + 3P(T)$ and $s(T) = (\epsilon + P)/T$, respectively.

In the high temperature region, $T > 250$ MeV, the trace anomaly can be accurately calculated using lattice QCD. Since discretization effects influence lattice calculations at low temperatures, $T \lesssim 180$ MeV, the HRG model is used in that regime. Such is no longer reliable in the intermediate temperature region $180 \text{ MeV} \lesssim T < 250 \text{ MeV}$, whereas a could still have a large value. Therefore, one constrains the trace anomaly in this interval by the value of the entropy density at high T [27].

QCD calculations of entropy density on the lattice ($N_\tau = 6$ and $N_\tau = 8$) deviate from the ideal gas limit in 5-10% for $T = 800$ MeV [27, 35]. Hence, when parametrizing the trace anomaly, the entropy density was required to be below the ideal gas limit by either 5% or 10% [27]. In this work, we chose the EoS parameterization with s at 95% of the ideal value at the highest temperature ($T = 800$ MeV).

In the high T regime, $\Theta(T)$ can be represented by an inverse polynomial form. The following Ansatz was used [27]:

$$\frac{\Theta(T)}{T^4} = \frac{\epsilon - 3P}{T^4} = \frac{d_2}{T^2} + \frac{d_4}{T^4} + \frac{c_1}{T^{n_1}} + \frac{c_2}{T^{n_2}}. \quad (2.42)$$

The table below depicts the parameter values:

$d_2(\text{GeV}^2)$	$d_4(\text{GeV}^4)$	$c_1(\text{GeV}^{n_1})$	$c_2(\text{GeV}^{n_2})$	n_1	n_2	$T_0(\text{MeV})$
0.2660	2.403×10^{-3}	-2.809×10^{-7}	6.07×10^{-23}	10	30	183.8

Table 2.1: Parameter values for $\Theta(T)$ at high T .

where T_0 is the temperature at which the parameterization above matches the HRG model. Trace anomaly as well as its first and second derivatives are required to be continuous in order to such matching occur. The HRG result for $\Theta(T)$ is the following parameterization:

$$\frac{\epsilon - 3P}{T^4} = a_1 T + a_2 T^3 + a_3 T^4 + a_4 T^{10}, \quad (2.43)$$

with parameter values:

$a_1(\text{GeV}^{-1})$	$a_2(\text{GeV}^{-3})$	$a_3(\text{GeV}^{-4})$	$a_4(\text{GeV}^{-10})$	$P(T_{low})/(T_{low})^4$
4.654	-879	8081	-7.039×10^6	0.1661

Table 2.2: Parameter values for $\Theta(T)$ at low T .

Finally, the EoS for both regimes is calculated by integrating equations (2.42) and (2.43), as in expression (2.41). The temperature interval $170 \text{ MeV} < T < 220 \text{ MeV}$ defines the region of transition [27]. For $T < 170$ MeV, the LattEoS agrees with the HRG model, hence this choice of lower limit. Rapid rise of entropy and energy density stops roughly at 220 MeV, from then on the variations of the said quantities will become smooth.

The heavy-ion collisions happening in both LHC and RHIC (at 200 AGeV) are expected to have small μ , hence the use of the lattice-based EoS discussed in this section in hydrodynamic codes. The EoS depicted in [36] is a recent (2014) development, where P is Taylor-expanded in chemical potentials for the sake of extending lattice QCD calculations to the $\mu \neq 0$ case.

2.3.3 Comparison between EoS

Having presented both EoS used in this work, we shall proceed on comparing them. Such analysis comprises a discussion on three stages of the hydrodynamic expansion of two colliding nuclei: Quark-Gluon Plasma, Hadron Gas and the phase transition between them.

In the low temperature regime, both EoS at hand agree on the Hadron Gas (HG) approach, as it can be clearly seen in Fig.2.3. CPEoS makes use of the Grand Canonical Ensemble in order to calculate pressure and other thermodynamic quantities, by considering the produced particles as an ideal quantum gas. While LattEoS applies the same idea, it parameterizes the trace anomaly as to coincide with the HG model for low T . The matching, however, stops here.

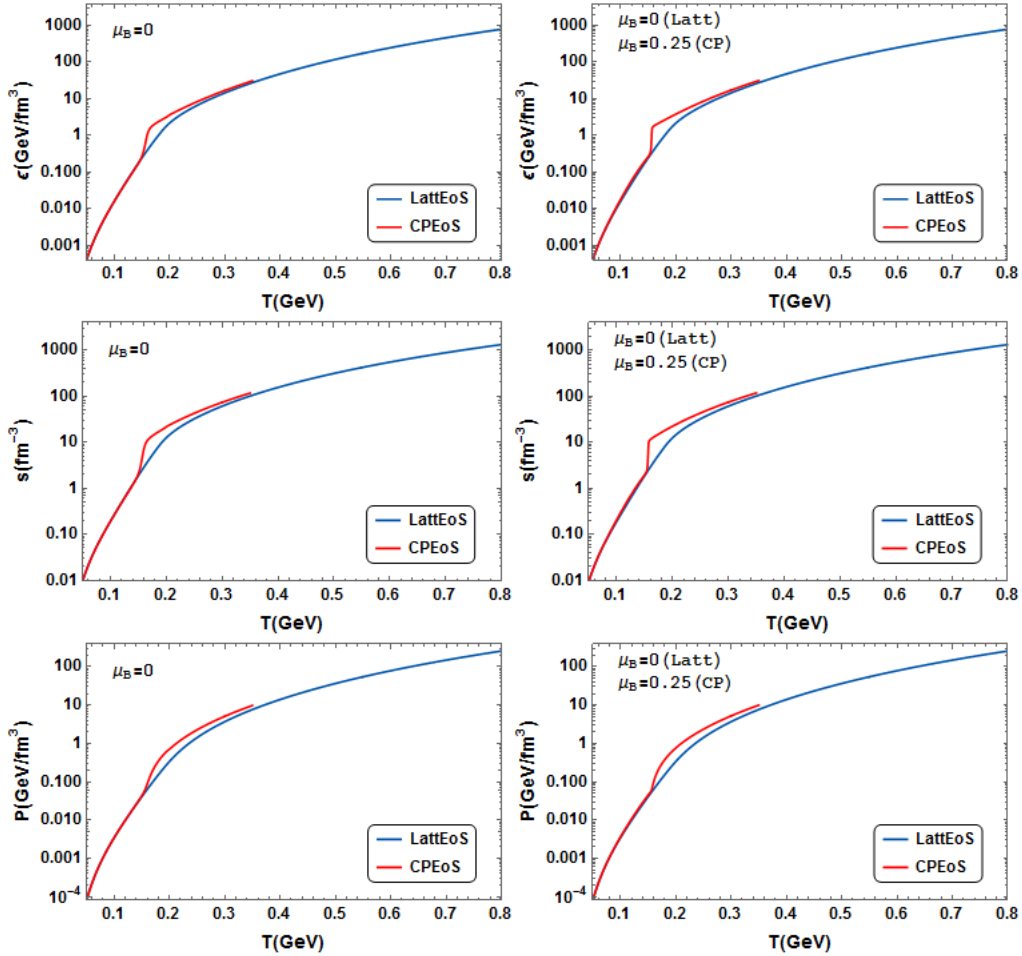


Figure 2.3: **Left column:** Comparison between LattEoS and CPEoS with $\mu_B = 0$ for ϵ , s and P as functions of T . Both base themselves in a HG model for low T , hence the curves coinciding in this regime. On the other hand, LattEoS utilizes lattice QCD whereas CPEoS employs the MIT Bag model for the QGP. **Right column:** Graphs of LattEoS for $\mu_B = 0$ and CPEoS for $\mu_B = 0.25$ as means of illustrating the sharper behavior of the latter's curve in the phase transition region.

Taking the QGP dominion (high T), LattEoS is defined up to the value of $T = 800$ MeV. Even though CPEoS is shown to only reach up to $T = 350$ MeV, we can easily make use of eq.(2.30) to compute thermodynamic quantities for collisions with higher multiplicity. Aside from that, the former utilizes lattice simulations of QCD, thus treating the QGP non-perturbatively, while the latter bases itself on the MIT Bag model, which considers the particles in such regime

as an ideal quark-gluon gas with a bag constant.

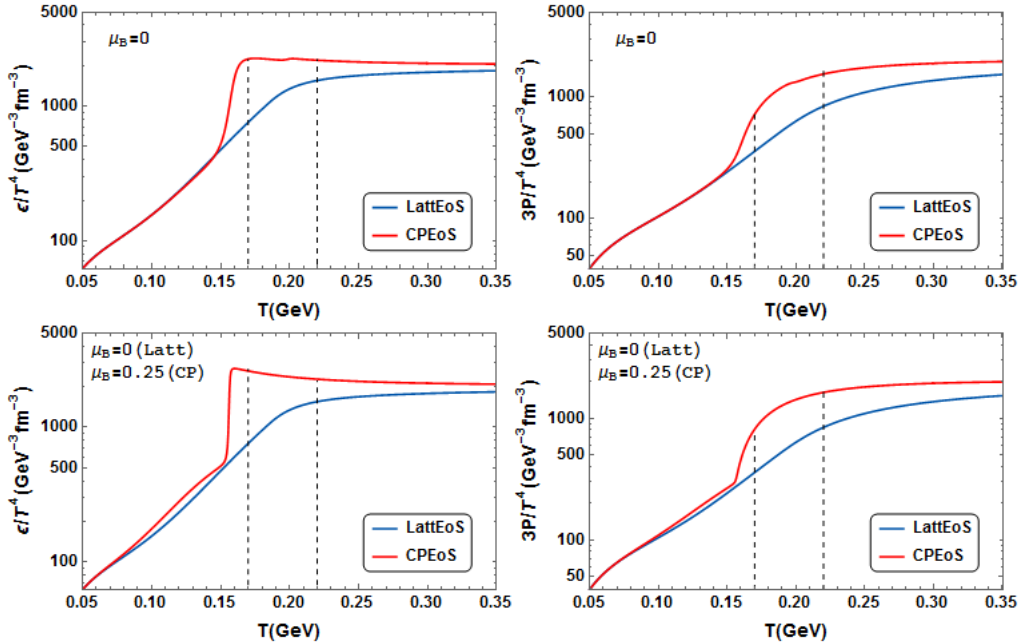


Figure 2.4: **First row:** Comparison between LattEoS and CPEoS with $\mu_B = 0$ for ϵ/T^4 and $3P/T^4$ as functions of T . The dashed lines represent the interval $170 \text{ MeV} < T < 220 \text{ MeV}$ which delimits the region where a phase transition could occur for LattEoS. **Second row:** Both EoS are plotted as means of comparing the differences in the phase transition region of CPEoS for $\mu_B = 0$ and $\mu_B = 0.25$. Furthermore, it is clear to see the slight discrepancy in the phase region between CPEoS at non-zero μ_B value and LattEoS.

As expected from the previous subsection on CPEoS, the equation's phase transition approaches a first order type for larger values of μ_B , whereas in the case $\mu_B = 0$ the curve is smoother as it is characteristic of a crossover type of transition. LattEoS, however, treats the said stage by constraining its trace anomaly by the value of entropy density at high temperatures (discussed in section 2.3.2). Hence the difference in slope for each curve.

Furthermore, there is discrepancy in the temperature interval delimiting the phase transition. For LattEoS, such is chosen between $170 \text{ MeV} < T < 220 \text{ MeV}$, represented by the dashed lines in Fig.2.4. In the CPEoS $\mu_B = 0$ case, for instance, the transition should occur between $T \sim 150 \text{ MeV}$ and $T \sim 168 \text{ MeV}$. It is worth remarking that for $\mu_B = 0.25$ the phase transition interval diminishes. When taking the graphs in the bottom row of Fig.2.4, the transition from HG to QGP should happen between $T \sim 153 \text{ MeV}$ and $T \sim 160 \text{ MeV}$. Aside from that, the low temperature region ceases to coincide perfectly with LattEoS.

The differences presented in this section have influence on determining certain parameters and computing results. Their effects shall be discussed in Chapter 4, where the latter is displayed.

2.4 Cooper-Frye Decoupling Mechanism

The expanding matter leads to the rapid increase in the mean free path of particles. That is to say, the system is changing from being strongly coupled to being weakly coupled until it

consists of substantially free streaming particles. Such stage in the evolution of matter is defined as thermal or kinetic freeze-out[14]. This work shall adopt the Cooper-Frye description[37] to model the said decoupling process. Other methods such as continuous emission and transport model will not be addressed.

The approach mentioned above assumes that the hadronic fluid suddenly stops interacting when the temperature falls to a decoupling value. Furthermore, it relies on the assumption of the particle momentum distribution being unaffected by the system's decoupling. In other words, the particle spectrum is evaluated on the freeze-out hypersurface σ characterized by:

$$T_{fo} = T(t, x, y, z), \quad (2.44)$$

where T_{fo} is called freeze-out temperature. We shall address how these isotherms are determined in Chapter 4.

In order to compute the momentum distribution of the particles crossing σ , one shall begin by portraying a many-body system as a collection of world lines. Let $d\sigma_\mu$ be the surface's normal four-vector at some space-time point x^μ and $Dp = 2\theta(p^0)\delta(p^2 - m^2)d^4p$ the four-volume in momentum space restricted to the mass-shell, centered on p^μ . The net number of lines transiting across $d\sigma_\mu$ is, thus, given by:

$$dN_W = f_W(x, p)p^\mu d\sigma_\mu Dp, \quad (2.45)$$

where $f_W(x, p)$ is the world line distribution function. Since σ is, in general, an arbitrary hypersurface, dN_W may not coincide with the net number of particles in said infinitesimal volume of the phase-space at a certain time, dN [38]. In other words, when σ is space-like, its normal vector is time-like and $d\sigma_\mu p^\mu > 0$, meaning that particles are leaving the surface. In such case, $dN_W = dN$. However, if σ is time-like, one can have either $d\sigma_\mu p^\mu > 0$ or $d\sigma_\mu p^\mu < 0$. In the latter, particles are actually returning to the fluid, causing $dN_W \neq dN$ [39]. In this work, with fluctuating initial conditions, the number of returning particles is assumed to be negligible [40].

With $dN_W = dN$, $f_W(x, p)$ should be the standard one-particle distribution function. In accordance to that, one has the following expression for the net number of particles crossing σ at a certain time t , with given four-momentum between p^μ and $p^\mu + Dp$:

$$dN = f(x, p)p^\mu d\sigma_\mu Dp, \quad (2.46)$$

whose integral

$$N = \int Dp \int_\sigma f(x, p)p^\mu d\sigma_\mu \quad (2.47)$$

counts the total number of emitted particles. One can also write it as the following:

$$\begin{aligned} N &= \int 2\theta(p^0)\delta(p^2 - m^2)d^4p \int_\sigma f(x, p)p^\mu d\sigma_\mu \\ &= \int 2\theta(p^0)\delta(p_0^2 - \vec{p}^2 - m^2)d^4p \int_\sigma f(x, p)p^\mu d\sigma_\mu \end{aligned}$$

Since $E^2 = \vec{p}^2 + m^2$, N can be expressed as:

$$N = \int 2\theta(p^0)\delta(p_0^2 - E^2)d^4p \int_{\sigma} f(x, p)p^{\mu}d\sigma_{\mu}.$$

Knowing that $\delta(x^2 - a^2) = \frac{1}{2|a|}(\delta(x + a) + \delta(x - a))$:

$$N = \int 2\theta(p^0)\frac{1}{2E}(\delta(p^0 + E) + \delta(p^0 - E))d^4p \int_{\sigma} f(x, p)p^{\mu}d\sigma_{\mu},$$

with $\theta(p^0) = 0$, if $p^0 < 0$ or $\theta(p^0) = 1$, if $p^0 > 0$, one shall finally have:

$$N = \int \frac{d^3p}{E} \int_{\sigma} f(x, p)p^{\mu}d\sigma_{\mu}. \quad (2.48)$$

Alternately, (2.48) can give the particle distribution in momentum space:

$$E \frac{dN}{d^3p} = \int_{\sigma} f(x, p)p^{\mu}d\sigma_{\mu}, \quad (2.49)$$

which is the said Cooper-Frye formula[37]. Due to the fluid being in local thermodynamic equilibrium as well as the assumption that there is no change in $f(x, p)$ during the decoupling process, the latter can be expressed as:

$$f(x, p) = \frac{g}{2\pi^3} \frac{1}{(e^{(p^{\mu}u_{\mu} - \mu_B)/T} \pm 1)}, \quad (2.50)$$

where the positive sign indicates a Fermi-Dirac distribution, while the negative one, a Bose-Einstein distribution; g is the degeneracy factor associated to the particle to be considered.

Chapter 3

On NexSPheRIO

3.1 The SPH Method

In Section 2.1, we derived a non-linear set of differential equations to describe ideal relativistic hydrodynamics. Due to their nature and the extremely complex medium caused by the IC fluctuations, it is no trivial task to solve those equations analytically, making numerical computation a desirable path to follow. In heavy-ion collisions, we take the hydrodynamic approach in order to infer information on its two main ingredients, the IC and EoS, from comparisons with experimental data. In this work, we adopt the Smoothed-particle Hydrodynamics (SPH) computational method, as introduced in [41] and [42] in order to study astrophysical problems. The aforementioned can lead to a very precise solution of the hydrodynamic equations[43].

The SPH approach allows the study of system configurations with any geometry, as well as the possibility of smoothing out unwanted local degrees of freedom. It is, therefore, a perfect fit to the variational formalism[7]. The basic idea of this method is to introduce a set of “particles” characterized by their Lagrangian coordinates $\{\vec{r}_i\}$, which move with the fluid. In order to achieve that, we shall begin by considering the physical extensive quantity A , with corresponding density distribution $a(\vec{r}, t)$. We can write the latter as:

$$a(\vec{r}, t) = \int a(\vec{r}', t) \delta(\vec{r} - \vec{r}') d^3 \vec{r}'. \quad (3.1)$$

In a first approximation, one should substitute $\delta(\vec{r} - \vec{r}')$ by a kernel function W , with finite support h and properties:

$$\int W(\vec{r} - \vec{r}'; h) d^3 \vec{r}' = 1, \quad (3.2a)$$

$$\lim_{h \rightarrow 0} W(\vec{r} - \vec{r}'; h) = \delta(\vec{r} - \vec{r}'), \quad (3.2b)$$

which allows for expressing $a(\vec{r}, t)$ as:

$$a(\vec{r}, t) \rightarrow \tilde{a}(\vec{r}, t) = \int a(\vec{r}', t) W(\vec{r} - \vec{r}'; h) d^3 \vec{r}'. \quad (3.3)$$

The density $\tilde{a}(\vec{r}, t)$ is a smoothed $a(\vec{r}, t)$. W introduces a short-wavelength cut-off filter in the Fourier representation of $\tilde{a}(\vec{r}, t)$ [7]. For a practical application, one may reduce the degrees of freedom, by replacing the integral in (3.3) with a sum over a finite and discrete set of points, $\{\vec{r}_i, i = 1, \dots, N\}$ [16]:

$$\tilde{a}(\vec{r}, t) \rightarrow a_{SPH} = \sum_i^N A_i W(\vec{r} - \vec{r}_i; h), \quad (3.4)$$

with weights A_i . Summing it all up:

$$a(\vec{r}, t) \rightarrow a_{SPH} = \sum_i^N A_i W(\vec{r} - \vec{r}_i; h). \quad (3.5)$$

The latter is an ansatz which approximates $a(\vec{r}, t)$ as a sum of finite dynamic “particles” with coordinates \vec{r}_i , carrying the quantity A_i . Due to property 3.2a,

$$\int a_{SPH}(\vec{r}, t) d^3\vec{r} = \sum_i^N A_i,$$

with

$$A_{tot} = \sum_i^N A_i$$

as the total amount of A in the system.

Since we deal with more than one extensive physical quantity in hydrodynamics, we choose a conserved quantity as the reference density, ρ , when applying the aforementioned method. The representation of ρ in the SPH form is

$$\rho_{SPH}(\vec{r}, t) = \sum_i^N \varrho_i W(\vec{r} - \vec{r}_i(t); h), \quad (3.6)$$

where $\vec{r}_i = \vec{r}_i(t)$ is the trajectory of the i -th “SPH particle and the weights $\{\varrho_i\}$ are constant in time. In that case, the time derivative of ρ_{SPH} ,

$$\frac{\partial}{\partial t} \rho_{SPH}(\vec{r}, t) = \sum_i^N \frac{\partial}{\partial t} (\varrho_i W(\vec{r} - \vec{r}_i(t); h)),$$

takes the value

$$\begin{aligned} \frac{\partial}{\partial t} \rho_{SPH}(\vec{r}, t) &= \sum_i^N \varrho_i \frac{d}{dt} W(\vec{r} - \vec{r}_i(t); h) \\ &= - \sum_i^N \varrho_i \frac{d\vec{r}_i(t)}{dt} \cdot \nabla \cdot W(\vec{r} - \vec{r}_i(t); h). \end{aligned}$$

Since $\frac{d\vec{r}_i(t)}{dt} = \vec{v}_i(t)$, the expression above becomes:

$$\begin{aligned}
\frac{\partial}{\partial t} \rho_{SPH}(\vec{r}, t) &= - \sum_i^N \varrho_i \vec{v}_i(t) \nabla \cdot W(\vec{r} - \vec{r}_i(t); h) \\
&= - \nabla \cdot \sum_i^N \varrho_i \vec{v}_i(t) W(\vec{r} - \vec{r}_i(t); h) \\
&= - \nabla \cdot \vec{j}_{SPH}(\vec{r}, t),
\end{aligned}$$

where

$$\vec{j}_{SPH}(\vec{r}, t) = \sum_i^N \varrho_i \vec{v}_i(t) W(\vec{r} - \vec{r}_i(t); h) \quad (3.7)$$

is the SPH representation of ρ 's current density, $\vec{j} = \rho \vec{v}$. Therefore, ρ_{SPH} satisfies the continuity equation:

$$\frac{\partial}{\partial t} \rho_{SPH} + \nabla \cdot \vec{j}_{SPH} = 0, \quad (3.8)$$

as expected.

It is rather simple to calculate other extensive quantities, such as A . Taking a as its density, then the amount of A carried by particle i for the unit reference ρ is:

$$A_i = \varrho_i \left(\frac{a}{\rho} \right)_i, \quad (3.9)$$

so that the density distribution $a(\vec{r}, t)$ becomes:

$$a(\vec{r}, t) \rightarrow a_{SPH}(\vec{r}, t) = \sum_i^N \left(\frac{a}{\rho} \right)_i \varrho_i W(\vec{r} - \vec{r}_i(t); h). \quad (3.10)$$

Physically speaking, we are replacing a continuous fluid by a set of the so called ‘‘SPH particles’’. Moreover, we take the associated coordinates $\{\vec{r}_i(t)\}$ as variational degrees of freedom. Their equations of motion are thus obtained by minimizing the action for the hydrodynamic system.

Since we are interested in relativistic hydrodynamics, it is highly convenient to extend the variational procedure to a general coordinate system, as in Appendix C. Hence the action for a relativistic fluid motion (from (C.9)):

$$I = - \int d^4x \sqrt{-g} \epsilon, \quad (3.11)$$

with constraints for conserved entropy (C.10) and baryon (C.11) densities:

$$(su^\mu)_{;\mu} = \frac{1}{\sqrt{-g}} \partial_\mu (\sqrt{-g} su^\mu) = 0, \quad (3.12)$$

$$(nu^\mu)_{;\mu} = \frac{1}{\sqrt{-g}} \partial_\mu (\sqrt{-g} nu^\mu) = 0. \quad (3.13)$$

Let s^* and n^* be the entropy and baryon densities in a space-fixed frame. From expression (3.6), we may parameterize

$$\sqrt{-g}s\gamma = s^* \rightarrow s_{SPH}^* = \sum_i \nu_i W(\vec{r} - \vec{r}_i(\tau)), \quad (3.14)$$

$$\sqrt{-g}n\gamma = n^* \rightarrow n_{SPH}^* = \sum_i \beta_i W(\vec{r} - \vec{r}_i(\tau)), \quad (3.15)$$

Since

$$\int d^3\vec{r} W(\vec{r} - \vec{r}_i) = 1, \quad (3.16)$$

the total entropy and baryon number are

$$S = \int d^3\vec{r} \sqrt{-g}s\gamma = \sum_i \nu_i, \quad (3.17)$$

$$B = \int d^3\vec{r} \sqrt{-g}n\gamma = \sum_i \beta_i. \quad (3.18)$$

Analogously to (3.6), ν_i and β_i are, respectively, the amount of entropy and baryon number carried by the i -th particle.

Since it is expected that most of the energy content is of non-baryonic nature (mostly pions), particularly in mid-rapidity regions (definition on Chapter 4), n is not suitable to be used as the reference density (ρ) in SPH representation[8]. Instead, the role falls on s , which does not vanish in the region of interest. We have also stated in Appendix B that τ is a more convenient coordinate to employ in the study of heavy-ion collisions, hence $\vec{r}_i = \vec{r}_i(\tau)$. In a generalized coordinate system, we use the notation $\tau = x^0$ and $\gamma = u^0$. The latter's generalized expression can be computed using

$$\begin{aligned} u_\mu u^\mu &= 1, \\ g_{\mu\nu} u^\nu u^\mu &= 1. \end{aligned}$$

We take the metric tensor as

$$(g_{\mu\nu}) = \begin{pmatrix} g_{00} & 0 \\ 0 & -\mathbf{g} \end{pmatrix} \quad (3.19)$$

whose time-like coordinate is orthogonal to the space-like ones in order to unambiguously define the conserved quantity s [16]. Also, $-\mathbf{g}$ is the 3×3 space part of $g_{\mu\nu}$. In this case,

$$g_{\mu\nu} u^\nu u^\mu = g_{00} u^0 u^0 - g_{ij} u^i u^j = 1.$$

Since $u^i = \gamma v^i = u^0 v^i$,

$$\begin{aligned} g_{00} u^0 u^0 - g_{ij} v^i v^j u^0 u^0 &= 1 \\ u_0^2 (g_{00} - g_{ij} v^i v^j) &= 1, \end{aligned}$$

which yields

$$\gamma = \frac{1}{\sqrt{g_{00} - \vec{v}^T g \vec{v}}}. \quad (3.20)$$

We shall proceed on writing the action (3.11) in the SPH representation, by making use of (3.10) and (3.14):

$$I_{SPH} = - \int d\tau \int d^3\vec{r} \sum_i \nu_i \left(\frac{\sqrt{-g}\epsilon}{\sqrt{-g}s\gamma} \right)_i W(\vec{r} - \vec{r}_i(\tau)) \quad (3.21)$$

$$= - \int d\tau \sum_i \nu_i \left(\frac{\epsilon}{s\gamma} \right)_i. \quad (3.22)$$

Before moving on to the next step, we should define the specific volume V_i of S associated with particle i ,

$$V_i \equiv \frac{\nu_i}{s_i}, \quad (3.23)$$

and substitute it in I_{SPH} :

$$\begin{aligned} I_{SPH} &= - \int d\tau \sum_i \left(\frac{\epsilon V}{\gamma} \right)_i \\ &= - \int d\tau \sum_i \left(\frac{E}{\gamma} \right)_i, \end{aligned} \quad (3.24)$$

with $\epsilon_i V_i = E_i$.

After minimizing the action above, one gets the following equation of motion[8]:

$$\begin{aligned} \frac{d\vec{\pi}_i}{d\tau} &= - \sum_j \nu_i \nu_j \left[\frac{P_i}{\sqrt{-g}\gamma_i^2 s_i^2} + \frac{P_j}{\sqrt{-g}\gamma_j^2 s_j^2} \right] \nabla_i W_{ij} \\ &\quad - (\nabla_i g_{00} - \vec{v}_i^T g \vec{v}_i) \frac{\gamma_i \nu_i}{2} \left(\frac{\epsilon + P}{s} \right)_i \\ &\quad + \frac{\nu_i P_i}{\gamma_i s_i} \left(\frac{1}{\sqrt{-g}} \nabla_i \sqrt{-g} \right), \end{aligned} \quad (3.25)$$

with

$$\vec{\pi}_i = \gamma_i \nu_i \left(\frac{P + \epsilon}{s} \right)_i g \vec{v}_i. \quad (3.26)$$

From Appendix B, we gather a rather convenient set of variables for heavy-ion collisions, the *proper time*, *space-time rapidity* and cartesian coordinates x and y :

$$\tau = \sqrt{t^2 - z^2}, \quad (3.27)$$

$$\eta_s = \frac{1}{2} \ln \left(\frac{t+z}{t-z} \right), \quad (3.28)$$

$$\vec{r}_T = \begin{pmatrix} x \\ y \end{pmatrix}, \quad (3.29)$$

respectively. Furthermore,

$$\begin{aligned} t = \tau \cosh(\eta_s) &\Rightarrow dt = \cosh(\eta_s)d\tau + \tau \sinh(\eta_s)d\eta_s, \\ z = \tau \sinh(\eta_s) &\Rightarrow dz = \sinh(\eta_s)d\tau + \tau \cosh(\eta_s)d\eta_s. \\ &\Rightarrow dt^2 - dz^2 = d\tau^2 - \tau^2 d\eta_s^2 \end{aligned}$$

Since $g_{\mu\nu}dx^\mu dx^\nu = \eta_{\mu\nu}d\xi^\mu d\xi^\nu$, with ξ^μ being coordinates in Minkowski space,

$$g_{\mu\nu}dx^\mu dx^\nu = dt^2 - dx^2 - dy^2 - dz^2 = d\tau^2 - dx^2 - dy^2 - \tau^2 d\eta_s^2.$$

From the metric tensor depicted in (3.19),

$$g_{00} = 1, \tag{3.30}$$

$$\mathbf{g} = \begin{pmatrix} 1 & 0 & 0 \\ 0 & 1 & 0 \\ 0 & 0 & \tau^2 \end{pmatrix}, \tag{3.31}$$

$$\sqrt{-g} = \tau. \tag{3.32}$$

The parametrization (3.14) will thus become

$$\tau \gamma_i s_i = s_i^* = \sum_j \nu_j W(q_{ij}),$$

where

$$q_{ij} = \sqrt{(x_i - x_j)^2 + (y_i - y_j)^2 + \tau^2((\eta_s)_i - (\eta_s)_j)^2}.$$

Finally, the SPH equation of motion takes the form

$$\frac{d\vec{\pi}_i}{d\tau} \equiv \frac{d}{d\tau} \begin{pmatrix} \vec{\pi}_T \\ \pi_{\eta_s} \end{pmatrix}_i = -\frac{1}{\tau} \sum_j \nu_i \nu_j \left[\frac{P_i}{\gamma_i s_i^2} + \frac{P_j}{\gamma_j s_j^2} \right] \nabla_i W_{ij}, \tag{3.33}$$

with

$$\vec{\pi}_T = \gamma \nu \left(\frac{P + \epsilon}{s} \right) \vec{v}_T, \tag{3.34}$$

$$\pi_{\eta_s} = \gamma \nu \left(\frac{P + \epsilon}{s} \right) \tau v_{\eta_s}, \tag{3.35}$$

where $\vec{v}_T = \frac{d\vec{r}_T}{d\tau}$ and $v_{\eta_s} = \frac{d\eta_s}{d\tau}$. Since

$$\vec{v}^T \mathbf{g} \vec{v} = \begin{pmatrix} v_x & v_y & v_{\eta_s} \end{pmatrix} \begin{pmatrix} 1 & 0 & 0 \\ 0 & 1 & 0 \\ 0 & 0 & \tau \end{pmatrix} \begin{pmatrix} v_x \\ v_y \\ v_{\eta_s} \end{pmatrix} = \vec{v}_T^2 + \tau^2 v_{\eta_s}^2,$$

the Lorentz factor (3.20) becomes

$$\gamma = \frac{1}{\sqrt{1 - \vec{v}_T^2 - \tau^2 v_{\eta_s}^2}}. \tag{3.36}$$

The ordinary equations of motion presented above yield the velocities and positions of the SPH particles as a function of the expansion time, τ . They allow for computing the evolution of all thermodynamic quantities, by taking also the equation of state and the parameterization of the conserved quantity, s^* , alongside with its current, $j^* = \vec{v}s^*$.

3.2 Decoupling in SPH

Having derived the fluid's equations of motion in the SPH formalism, it becomes clear that such method should also be extended to the Cooper-Frye formula defined in Chapter 2,

$$E \frac{dN}{d^3p} = \int_{\sigma} d\sigma_{\mu} p^{\mu} f(u_{\mu} p^{\mu}, T, \mu_B).$$

In order to compute the momentum distribution of SPH particles crossing the surface σ , we shall begin by approximating the expression above to a sum over all given particles in the system

$$E \frac{dN}{d^3p} = \sum_j (\Delta\sigma n_{\mu})_j p^{\mu} f(p^{\mu}(u_{\mu})_j, T_{f\sigma}, (\mu_B)_j), \quad (3.37)$$

where $\Delta\sigma_j$ is a hypersurface element, $(n_{\mu})_j$ its normal vector and

$$f(p^{\mu}(u_{\mu})_j, T_{f\sigma}, (\mu_B)_j) = \frac{g_j}{2\pi^3} [e^{(p^{\mu}(u_{\mu})_j - (\mu_B)_j)/T_{f\sigma}} \pm 1]^{-1}. \quad (3.38)$$

As (3.37) and (3.38) make explicit, the quantities with index j are inherent to the j -th particle when it is localized at σ , which in turn is defined by the isotherm $T_{f\sigma}$.

Aside from $\Delta\sigma_j$, all other quantities present in the expressions above can be computed rather directly from previously mentioned formulas by a method to be discussed in Chapter 4. Therefore, it becomes necessary to write $\Delta\sigma_j$ in terms of more convenient quantities. Take, for instance, a particle j in its proper frame (PF). In that case, $p^{\mu} \rightarrow p^0$, which implies that $p^{\mu}(n_{\mu}\Delta\sigma)_j \rightarrow p^0(n_0\Delta\sigma)_j$, when the particle reaches σ . Furthermore, $(n_0\Delta\sigma)_j$ can be identified as $(\Delta\sigma_0)_j^{PF}$, the proper hypersurface element.

Having established $(\Delta\sigma_0)_j^{PF}$, it is worth recalling from its definition, that it possesses only the time component. Henceforth,

$$|(\Delta\sigma_0)_j^{PF}| = V_j, \quad (3.39)$$

where V_j is the 3-dimensional volume of the j -th particle in its proper frame. We thus proceed on recovering $(\Delta\sigma_{\mu})_j$ through a Lorentz transformation,

$$\begin{aligned} (\Delta\sigma_{\mu})_j &= [\Lambda^0_{\mu}(\Delta\sigma_0)^{PF}]_j = [(\gamma, -\gamma v_i)(\Delta\sigma_0)^{PF}]_j \\ &= [u_{\mu}(\Delta\sigma_0)^{PF}]_j, \end{aligned}$$

where we used the set of equations (2.5). Contracting with u^{μ} on both sides, yield

$$(\Delta\sigma_0)_j^{PF} = (u^{\mu})_j(\Delta\sigma_{\mu})_j. \quad (3.40)$$

Then,

$$\begin{aligned}
V_j &= |(u^\mu)_j(\Delta\sigma_\mu)_j| = |(u^\mu n_\mu)_j| \Delta\sigma_j, \\
&\Rightarrow (\Delta\sigma)_j = \frac{V_j}{|(u^\mu n_\mu)_j|}.
\end{aligned}
\tag{3.41}$$

Rewriting (3.37),

$$E \frac{dN}{d^3p} = \sum_j \frac{\nu_j (n_\mu)_j p^\mu}{s_j |(u^\mu n_\mu)_j|} f(p^\mu (u_\mu)_j, T_{fo}, (\mu_B)_j),
\tag{3.42}$$

which is the Cooper-Frye formula in the SPH formalism. In order to reach the expression above, we made use of $V_j = \nu_j/s_j$.

3.3 The Code's Structure

Having presented the main ingredients, we shall move on to explain how they are assembled to yield results. Developed by a São Paulo-Rio de Janeiro collaboration, SPheRIO (**S**moothed-**P**article **h**ydrodynamic **e**volution of **R**elativistic heavy-**I**on collisions)[7, 8, 44], as its name suggests, is a SPH-based numerical code which describes the dynamics of heavy-ion collisions. A discussion on the essential elements of SPheRIO can be found in [16]. In particular, one usually employs the Nexus[6] event generator coupled to the said code, hence the name Nex-SPheRIO. As mentioned in section 2.2, we shall adopt the latter in this work.

Figure 3.1 is an outline of NexSPheRIO's flow chart. Its major blocks consist in the initial conditions, equations of motion, freeze-out scenario, hadron emission and decays plus resonances. Firstly, one should provide some input information, such as incident energy, the type of nuclei involved in the collision, impact parameter (more details on Chapter 4). Nexus makes use of those to calculate, at $\tau_0 = 1$ fm, the energy-momentum tensor, $T^{\mu\nu}$, and the conserved currents, J_I^μ , where I stands for baryon number(B), strangeness(S) and electric charge(Q). In this work, we impose the conditions $n_S = 0$ and $n_Q = 0$.

Secondly, SPheRIO, which is divided in three main blocks[40], will take Nexus's results of energy (ϵ) and baryon number (n_B^μ) densities as well as velocity (u^μ) in order to define the initial conditions of the SPH particles. Each of latter is a point in a pre-established SPH-particle lattice ($25 \times 25 \times 25$ in our case) and their IC correspond to the quantities ν_i , β_i and \vec{v}_i . The first two are non-dynamic values used to compute s^* (eq.3.14) and n^* (eq.3.15), respectively. The remaining one is calculated through relation (3.7). These steps sum up the first main block, SPheRIO(1). The subsequent part deals with the equations of motion depicted in (3.33). Alongside with either equation of state discussed in section 2.3, it is possible to work out the dynamics of v_i and all thermodynamic quantities associated with each SPH particle, until their temperatures become smaller than T_{fo} , thus ending SPheRIO(2)'s role. At last, Monte Carlo method is summoned in order to emulate hadron emission. Through the information on the variables associated with each SPH particle stored in the surface σ , SPheRIO(3) calculates the total number of particles emitted and their respective identities,

$$N = \int \frac{d^3p}{E} \sum_j \frac{\nu_j (n_\mu)_j p^\mu}{s_j |(u^\mu n_\mu)_j|} f(p^\mu (u_\mu)_j, T_{fo}, (\mu_B)_j),
\tag{3.43}$$

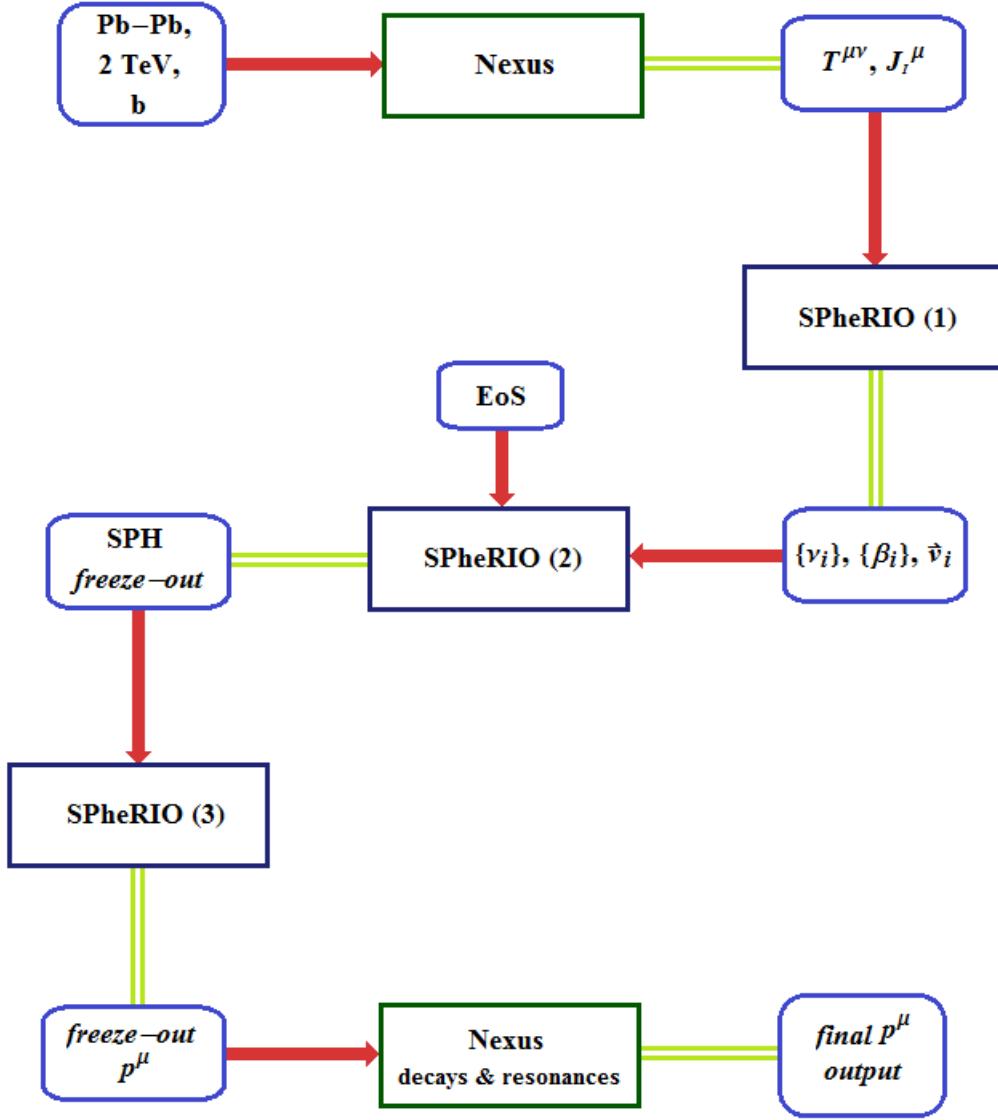


Figure 3.1: **NexSPheRIO's structure** - The soft-edged rectangles symbolize inputs/outputs and the ones with pointy edges are the main blocks. The red arrows represent the results input in each block, whereas the green lines lead to the output of each block. Pb-Pb are the colliding nuclei at incident energy 2 TeV (maximum allowed by Nexus); b is the impact parameter and it defines the chosen *centrality window* (to be discussed in Chapter 4).

which is (3.42) integrated. Moreover, the 4-momentum p^μ of each particle species is randomly chosen[40].

Lastly, the final result SPheRIO yields (p^μ values for each particle type) returns to Nexus. It then computes the particle decays and resonances, thus generating a new output of p^μ 's. The whole process is repeated as many times as the total number of events, hence the name *event-by-event method*. In the subsequent chapter, we shall calculate different observables by making use of the said output file, for both EoS and a couple of centrality windows. The freeze-out temperature (T_{fo}) is also an input parameter; Chapter 4 deals with the details of its definition.

Chapter 4

Results

4.1 Centrality Classes

In ultra-relativistic heavy-ion collisions, the energy involved is high enough to create particle-antiparticle pairs. Therefore, the energy binding nucleons inside nuclei as well as that of excited nuclear states may be ignored. As a result, only the spatial distribution of nucleons and their cross section value have relevance to the collision outcome. Those are responsible for the fluctuations in the initial energy density distribution observed and discussed in section 2.2. Considering that, we make use of simple geometric concepts (to be defined below) in order to study the initial moments of the colliding nuclei.

Assuming that all nucleons propagate parallel to each other along straight line trajectories, we may call the ones interacting as *participants*, whereas the ones who do not as *spectators*. Alongside with the number of binary nucleon-nucleon collisions, the numbers of participants and spectators comprise some of the overlapping nuclei geometrical properties. The volume of such interacting region as well as its cross section depend on the *impact parameter*, defined as the length of a vector connecting the nuclei centers in a plane transverse to the collision axis.

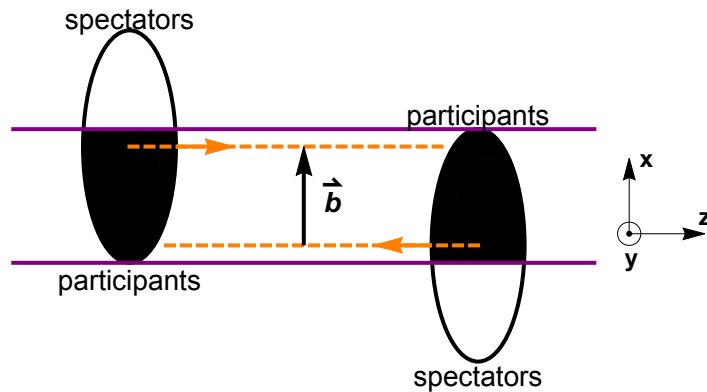


Figure 4.1: Schematic depiction of two colliding Lorentz-contracted nuclei seen from above. The region in black illustrates the participants, whereas white stands for the spectators. The z -axis is parallel to the accelerator beam and the *impact vector* \vec{b} , points in the x -axis direction. Axes x and z comprise the collision's *reaction plane*.

One can clearly see from Fig.4.1 that for central collisions, the centers of the colliding nuclei are brought closer together, thus making b approach zero. On the other hand, more peripheral collisions bring the nuclei centers further apart, hence increasing the value of b . In the field of

heavy-ion collisions, it is customary to introduce a quantitative measure called *centrality*, which is directly related to the impact parameter. The former is usually expressed as a percentage of the total nuclear interaction cross section σ_{cross}^{nucl} [45]. In a nucleus-nucleus collision with impact parameter b , the centrality percentile c takes the form

$$c = \frac{\int_0^b d\sigma_{cross}/db'db'}{\int_0^\infty d\sigma_{cross}/db'db'} = \frac{1}{\sigma_{cross}^{nucl}} \int_0^b \frac{d\sigma_{cross}}{db'} db', \quad (4.1)$$

where $d\sigma_{cross}/db'$ is the impact parameter distribution. The equation above may be simplified by replacing the cross section using the number of events, N :

$$c \approx \frac{1}{N} \int_0^b \frac{dN}{db'} db'. \quad (4.2)$$

Neither the numbers of participants, nor binary collisions, nor the impact parameter can be directly measured. Therefore, experimentalists from ALICE define c as the percentile of events corresponding to a particle multiplicity (number of particles produced in a collision) above a given threshold or an energy deposited in the Zero-Degree Calorimeters (ZDC) below a given value[45]. Since the latter is closely related to the number of participants N_p , we shall assign such parameter to describe each centrality. It is evident from Fig.4.1 that for $b \sim 0$, N_p is close to its maximum value, $2A$, where $A = 208$ is the atomic mass number of Pb^{208} . Additionally, for a given value b , $N_p = N_p(c)$, the number of participants for the correspondent centrality. We may thus rewrite eq.(4.2) in terms of N_p :

$$c \approx - \int_{2A}^{N_p(c)} \frac{dN}{dN_p'} dN_p', \quad (4.3)$$

where $\frac{1}{N} \frac{dN}{dN_p'} \rightarrow \frac{dN}{dN_p}$ is the normalized number of participants distribution – Fig.4.2 (left). The minus sign is due to the relation between b and N_p : the latter monotonically decreases while the former increases with less central collisions. Fig.4.2 (right) depicts the said relationship.

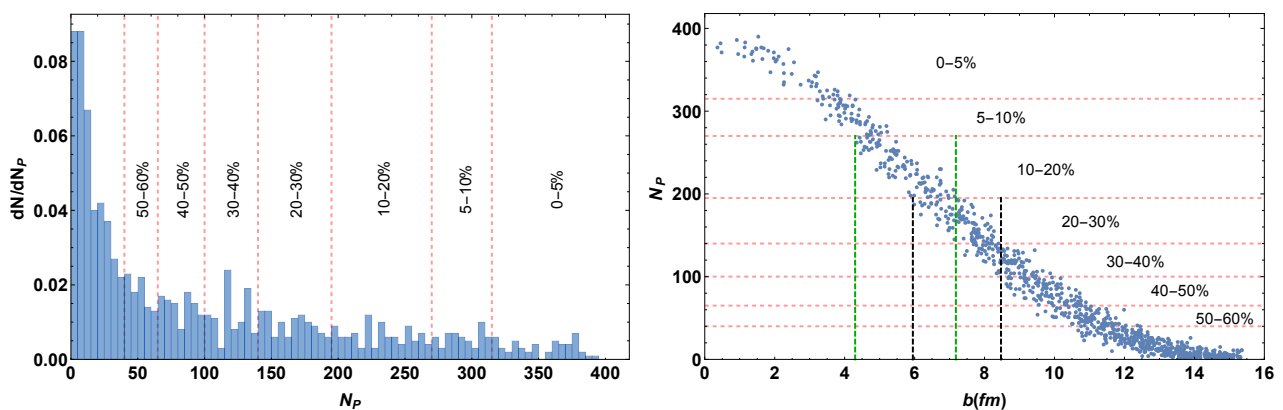


Figure 4.2: **Left:** Distribution of the number of participants (dN/dN_p); the red dashed lines mark the centrality classes in both graphs. **Right:** Number of participants (N_p) as a function of the impact parameter (b); the green and black dashed lines delimit b intervals for the centrality classes of 10–20% and 20–30%, respectively.

In order to calculate observables such as pseudo-rapidity and transverse momentum distributions (to be seen in the next section) and compare their results with the experimental data, it is necessary to divide the centrality classes according to ALICE-LHC's division, found

in [45, 46, 47]. Firstly, we employed the Nexus code to generate 1000 events with impact parameter values spanning from $b = 0$ to $b > 2R_{\text{Pb}}$, the latter being the nuclear radius of lead. The distribution of the number of participants was then computed: we counted the number of events for given intervals of N_p (Fig.4.2 left). From expression (4.3), it is possible to determine the value of N_p for each centrality class: taking 0–5%, for instance, one counts 5% of the events with higher multiplicity and checks the corresponding number of participants, thus obtaining $N_p(5\%) \sim 315$. For the next centrality class, 5–10%, one repeats the aforementioned procedure and excludes the previous window (0–5%), which gives $270 \lesssim N_p \lesssim 315$. Those steps are repeated for each centrality class.

As seen in section 3.3, the impact parameter b is an input value for NexSPheRIO, hence the importance of finding a b interval for each centrality class. After delimiting the centrality classes in the left side of Fig.4.2, those same divisions are made in the N_p vs. b graph (right side). The dashed black lines represent the b interval for the centrality class of 20–30%. Notice that they comprise more than just the events inside the 20–30% region. This issue is solved by also inputting the correspondent number of participants. Table 4.1 depicts the intervals of b and N_p for each centrality class.

Centrality(%)	Number of Participants(N_p)	Impact Parameter(b)
0–5%	416 – 315	0.00 – 4.19
5–10%	315 – 270	3.18 – 5.26
10–20%	270 – 195	4.30 – 7.18
20–30%	195 – 140	5.95 – 8.47
30–40%	140 – 100	7.39 – 10.22
40–50%	100 – 65	8.59 – 10.93
50–60%	65 – 40	9.48 – 12.49

Table 4.1: Centrality classes and their respective values of N_p and b .

The number of participants for each centrality class in the table above is in reasonable agreement with that determined by ALICE[45], except for the 5–10% bin, where their average N_p is higher. The intervals of b in Table 4.1 overlap, as explicitly shown by the dashed green and black lines of Fig.4.2 (right). Having defined such values, we shall move on to computing some observables (sections 4.2 and 4.3) for specific centralities and, subsequently, compare the results with the experimental data of ALICE, CMS and ATLAS.

4.2 Particle Spectra

Having presented all necessary ingredients and set the input parameters b and N_p for each centrality class, we shall employ the event-by-event method and primarily run NexSPheRIO to analyze the charged hadron production of ultra-relativistic heavy-ion collisions. In order to do that we calculate from the code’s output (all produced particles and the values of each of their \vec{p} components) the pseudorapidity and transverse momentum distributions. The latter,

as its name suggests, is the particle 3-momentum component in the x - y (transverse) plane, designated by p_T . The pseudorapidity variable, η , is defined as the following:

$$\eta \equiv \frac{1}{2} \ln \left[\frac{|\vec{p}| + p_L}{|\vec{p}| - p_L} \right] = -\ln \left(\tan \frac{\theta}{2} \right), \quad (4.4)$$

where $p_L = p_z$ is the 3-momentum longitudinal component and θ is the polar angle between the charged particle direction and the beam axis.

Subsections 4.2.1 and 4.2.2 discuss the aforementioned distributions for the centrality classes of 0–5% , 5–10%, 10–20% and 20–30% as well as both equations of state described in Chapter 2. The results are then compared with ALICE data from [46, 47].

4.2.1 Pseudorapidity Distribution

One way of analyzing particle production in heavy-ion collisions is by computing the pseudorapidity spectrum, as previously mentioned. Since the latter does not require particle identification, it presents itself as a viable candidate to compute the N_{ch} distribution.

LHC produced Pb-Pb collisions at a center-of-mass energy per nucleon pair of $\sqrt{s_{NN}} = 2.76$ TeV. Measurements of charged particle pseudorapidity density are performed using the full coverage of the ALICE detector, $-5.0 < \eta < 5.5$ [46]. However, as it was previously mentioned, the Nexus code is only able to run up to an energy beam of 2 ATeV. With the said energy as input, we have also selected the 20–30% centrality window and freeze-out temperature of $T_{fo} = 150$ MeV, in order to obtain the first results depicted in Fig.4.3 for both CPEoS (green) and LattEoS (red).

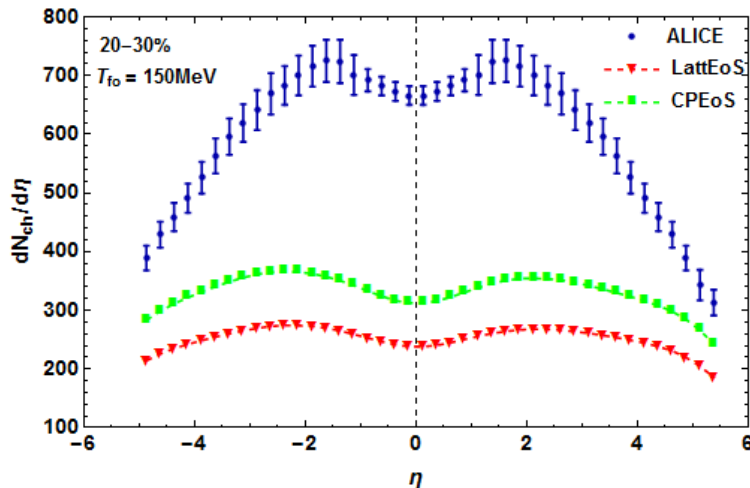


Figure 4.3: Pseudorapidity distribution of charged particles at incident energy 2 ATeV for the 20–30% centrality at $T_{fo} = 150$ MeV (both EoS) in comparison to the ALICE data[46].

Firstly, the Nexus initial conditions are input into SPheRIO without any corrections or being normalized. Due to that and the nuclei colliding at 2 TeV, the number of charged particles produced is considerably below the experimental data. There is also a difference in produced particle number between the EoS, as well as shape of the η distributions: the CPEoS result appears to be a little sharper than the one from LattEoS. We use the procedure described in [40] to fix this difference between simulated and observed charged particle numbers. It consists

in introducing a function dependent on η_s (spacetime rapidity) whose objective is to correct the initial energy density (ϵ_0) generated by Nexus along the longitudinal axis. In order to relate ϵ_0 with the pseudorapidity distribution of particles, we shall approximate

$$\eta = \frac{1}{2} \ln \left[\frac{|\vec{p}| + p_z}{|\vec{p}| - p_z} \right] \simeq \eta_s = \frac{1}{2} \ln \left[\frac{t + z}{t - z} \right], \quad (4.5)$$

which holds true at LHC energies. Such correction should preserve the fluctuations characteristic of an event initial energy density distribution.

The aforementioned function can be parameterized in the following way[40] and it is shown in Fig. 4.4 (left):

$$f(\eta) = \frac{e_0}{\exp [10^3(|\eta| - b_0)] + 1} + \frac{e_0 \exp [-f_0(|\eta| - b_0)^2]}{\exp [-10^3(|\eta| - b_0)] + 1}, \quad (4.6)$$

where the values of parameters e_0 , b_0 and f_0 are determined when fitting the NexSPheRIO results to the ALICE data i.e., through the difference between calculations and experimental data. We then insert the correction $f(\eta)$ in SPheRIO and compute again the pseudorapidity distribution for both EoS. After usually two iterations, we obtain Fig.4.4 (right).

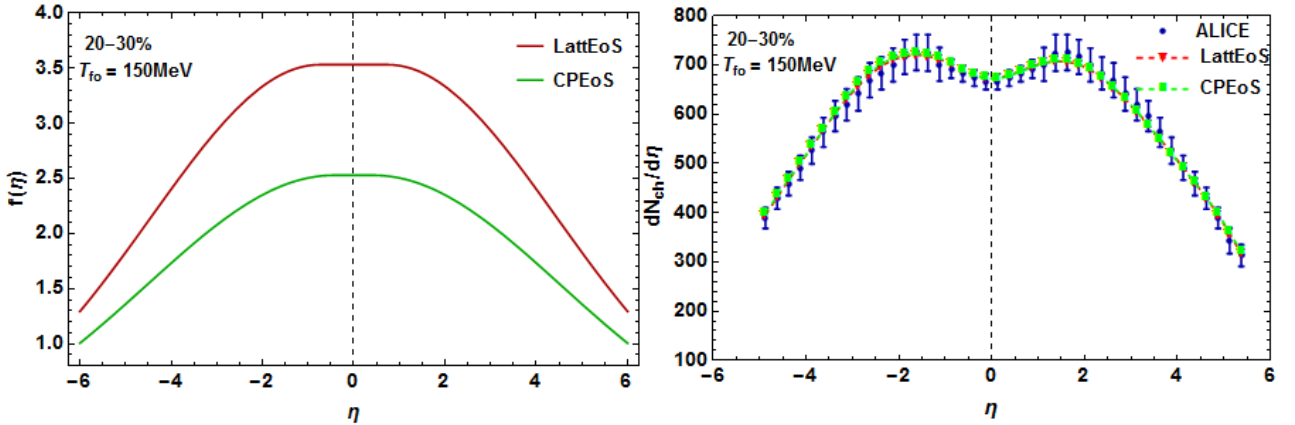


Figure 4.4: **Left:** Correction function $f(\eta)$ for both EoS. **Right:** Pseudorapidity distributions resultant of the adjusted initial energy density distribution. The LattEoS $f(\eta)$ has a flat region for $|\eta| \lesssim 0.9$, whereas the CPEoS $f(\eta)$ has the same for $|\eta| \lesssim 0.7$. Such discrepancy is related to their shapes when there is no correction; LattEoS' central plateau is closer in shape to the experimental data than CPEoS', hence its wider width.

The parameter values for LattEoS are $e_0 = 3.530$, $b_0 = 0.7455$ and $f_0 = 0.03633$ and for CPEoS they are $e_0 = 2.528$, $b_0 = 0.4347$ and $f_0 = 0.02972$. The behavior of $f(\eta)$ is characterized by a central flat area whose height equals e_0 and a rapid decrease to zero for higher $|\eta|$. With the corrected pseudorapidity distributions shown in Fig.4.4, it is now possible to compute other observables, such as transverse momentum distribution, flow, etc.

By repeating the same process discussed above for the other centralities and running NexSPheRIO with normalized initial conditions, we shall get the result depicted in Fig.4.5. A comparison is made with the ALICE data (the curves with error bars) for both equations of

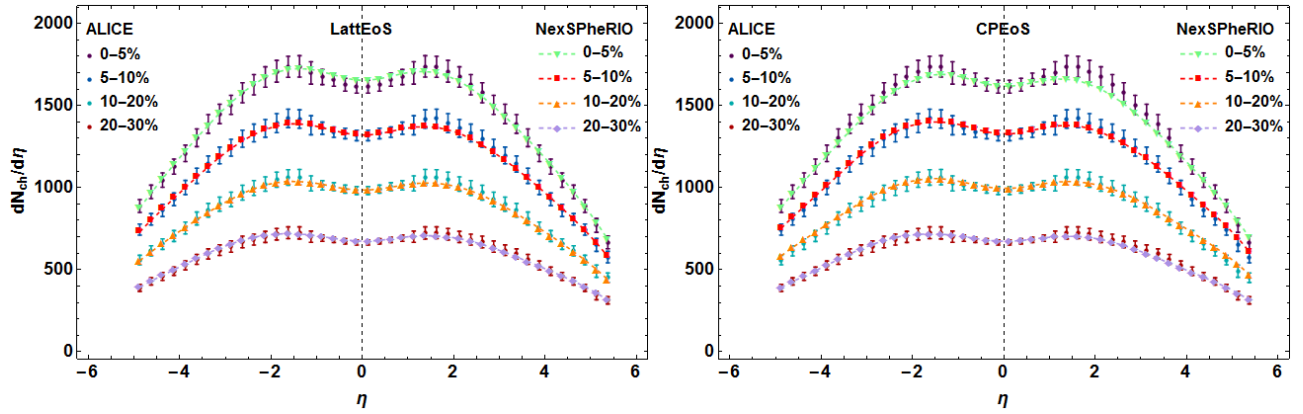


Figure 4.5: Distribution of charged particles in terms of the pseudorapidity for both LattEoS (left) and CPEoS (right) from the 0–5% to the 20–30% centrality. ALICE data corresponds to the curves with error bars, whereas the NexSPheRIO results are depicted in lighter colors (their respective legends are on the right side of each graph).

state (LattEoS on the left and CPEoS on the right).

It is worth remarking that each centrality class possesses different freeze-out temperatures among themselves and for each EoS. The details of determining T_{fo} will be discussed in the subsequent sections on transverse momentum distribution and flow. Table 4.2 shows the values of parameters e_0 , b_0 and f_0 for all centrality classes in Fig.4.5 as well as their freeze-out temperatures for both equations of state. We should notice that e_0 has a higher value for the LattEoS results (as expected from Fig. 4.3).

Centrality	LattEoS				CPEoS			
	e_0	b_0	f_0	$T_{fo} = \text{MeV}$	e_0	b_0	f_0	$T_{fo} = \text{MeV}$
0–5%	3.607	0.6333	0.04198	135	2.675	0.04852	0.02794	130
5–10%	3.701	0.6032	0.03825	140	2.716	0.3923	0.02911	135
10–20%	3.795	0.8437	0.04168	150	2.613	0.3788	0.02731	140
20–30%	3.530	0.7455	0.03633	150	2.528	0.4347	0.02972	140

Table 4.2: Parameter values and freeze-out temperature for centrality classes from 0–5% to 20–30% and both EoS. For LattEoS T_{fo} is higher than for CPEoS.

In order to compute other observables, one has to input the values depicted above for the chosen centrality (determined by b and N_p) and equation of state. Finally, we analyze the dependence of $f(\eta)$ on the freeze-out temperature for both EoS and the most central and peripheral collisions treated in this work. In Fig. 4.6, for the 0–5% window at $T_{fo} = 130$ MeV and 140 MeV for the CPEoS equation of state as well as $T_{fo} = 135$ MeV and 145 MeV for the LattEoS one. For the 20–30% case, the comparison is made with $T_{fo} = 140$ MeV and 150 MeV (CPEoS) as well as $T_{fo} = 150$ MeV and 160 MeV (LattEoS).

Since $f(\eta)$ is basically the same for the CPEoS at distinct T_{fo} , the latter may be treated

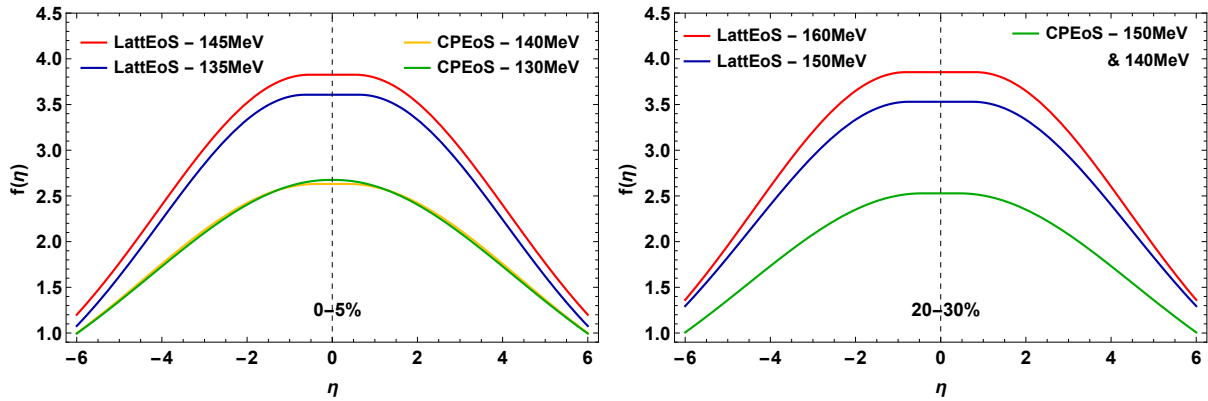


Figure 4.6: Parametrization function $f(\eta)$ for both 0–5% (left) and 20–30% (right), different freeze-out temperatures and both EoS. In the LattEoS and 0–5% CPEoS cases, the procedure discussed in this section was thoroughly followed, while for 20–30% CPEoS the same $f(\eta)$ was used, yielding the results on the right side of Fig.4.5 (140 MeV) and in Fig.4.4 (150 MeV).

as a free parameter when computing observables with such equation of state for any chosen centrality. In the LattEoS case, though, the functions are slightly different: the discrepancy between plateau heights is of approximately 0.2 for 0–5% and 0.3 for 20–30%. Therefore, one must always calculate new e_0 , b_0 and f_0 values whenever T_{fo} is changed while using LattEoS. From this point on, all quantities are obtained with normalized (corrected) initial conditions.

4.2.2 Transverse Momentum Distribution

The module of a particle 3-momentum $|\vec{p}| = p$ is, by definition,

$$p^2 = p_x^2 + p_y^2 + p_z^2 = p_T^2 + p_z^2, \quad (4.7)$$

where p_T and p_z are, respectively, the transverse and longitudinal components of \vec{p} , as already established. When manipulating expression (4.4), we find that

$$\frac{p_z}{p} = \frac{\sinh \eta}{\cosh \eta}.$$

Substituting (4.7) in the equation above yields the following relations:

$$p = p_T \cosh \eta, \quad (4.8)$$

$$p_z = p_T \sinh \eta. \quad (4.9)$$

It is clear that for $\eta \sim 0$ – also called *mid(pseudo)rapidity region* – $p \sim p_T$ and $p_z \sim 0$.

Since the transverse momentum and pseudorapidity are independent variables, it is only natural that analysis of hadron production should also be computed in terms of p_T . Furthermore, we may recall from the Cooper-Frye formula introduced in Chapter 2 that the particle momentum distribution, dN/d^3p , is dependent on the freeze-out temperature, which allows for further insight into the definition of T_{fo} values.

The ALICE Collaboration performs the measurements of charged particle p_T distributions in the pseudorapidity interval $|\eta| < 0.8$ [47] – basically the midrapidity region. Fig. 4.7 is a

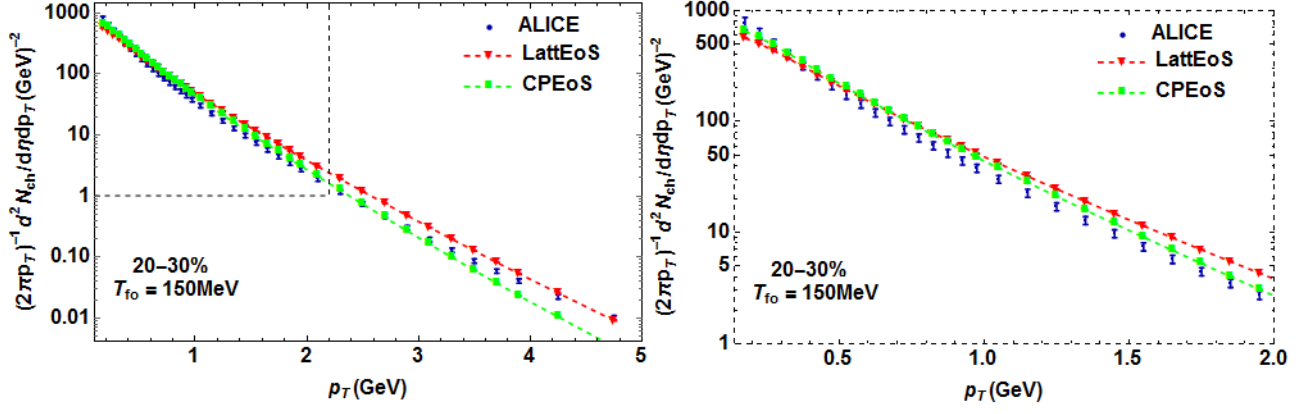


Figure 4.7: Transverse momentum distribution for LattEoS and CPEoS in the 20–30% centrality at $T_{fo} = 150$ MeV for $|\eta| < 0.8$. The points with error bars is the ALICE data from [47]. The graph on the right is the area encompassed by the dashed lines on the left graph zoomed in. In this work, it is of interest to analyze the low p_T region.

comparison between said experimental data and the NexSPHERIO results for both EoS in the 20–30% centrality at $T_{fo} = 150$ MeV.

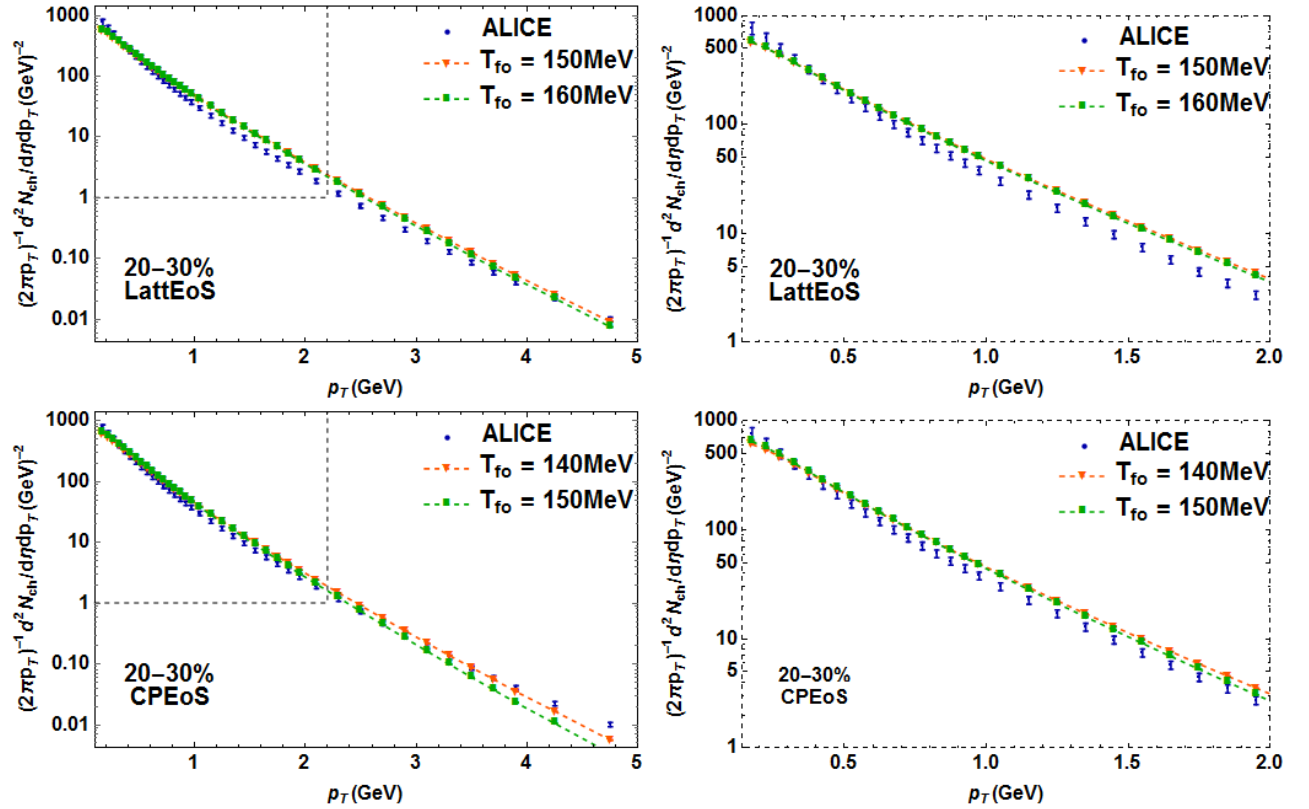


Figure 4.8: Transverse momentum distributions of charged particles for LattEoS (top row) and CPEoS (bottom row) at distinct freeze-out temperatures in the 20–30% centrality. The graphs on the right are augmentations of the areas contoured by the dashed lines on the left.

At the same freeze-out temperature, the EoS behave differently. The LattEoS curve being

above CPEoS at high p_T values means that it accelerates more the fluid than the latter. In compensation, the number of particles with $p_T \lesssim 0.58$ GeV for LattEoS is smaller than the CPEoS result's. Such discrepancy between these EoS is related to their difference in stiffness.

The next step consists in trying to pinpoint the best freeze-out temperature for each EoS, at all given centralities. Fig.4.8 shows a comparison between the ALICE and NexSPheRIO data at $T_{fo} = 150$ MeV and $T_{fo} = 160$ MeV for LattEoS (top) and at $T_{fo} = 140$ MeV and $T_{fo} = 150$ MeV for CPEoS (bottom). There is very little difference in the p_T distribution for LattEoS when changing temperatures. Its results at $p_T \lesssim 0.3$ GeV are slightly below the experimental data, while in the 0.6 GeV $\lesssim p_T \lesssim 3.7$ GeV interval at 160 MeV and the 0.6 GeV $\lesssim p_T \lesssim 4.2$ GeV interval at 150 MeV they are above it. The CPEoS curves are closer to data but also above in a mid p_T interval: 0.5 GeV $\lesssim p_T \lesssim 2.7$ GeV at $T_{fo} = 140$ MeV and 0.5 GeV $\lesssim p_T \lesssim 1.85$ GeV at $T_{fo} = 150$ MeV.

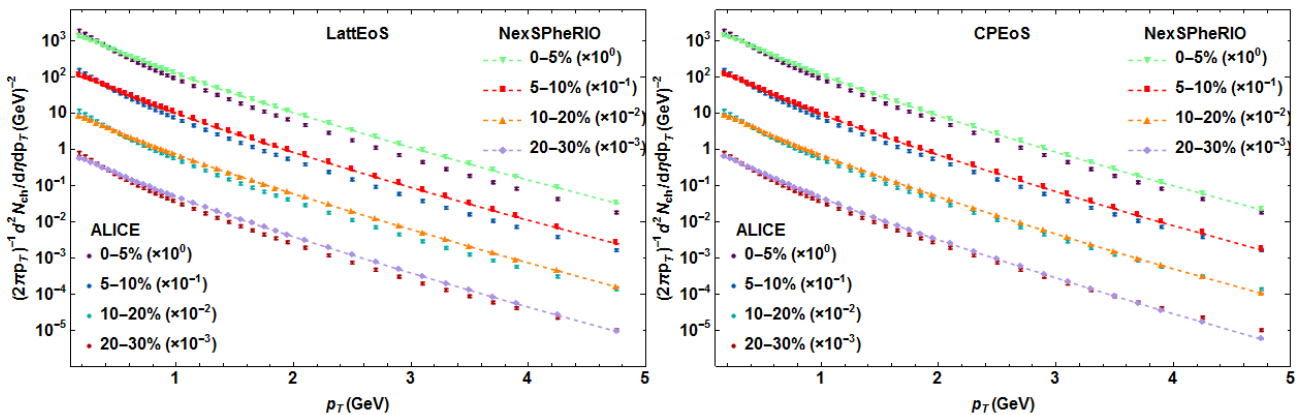


Figure 4.9: Transverse momentum distribution for both EoS in all centralities at the freeze-out temperatures depicted in Table 4.2. Comparison with ALICE data from [47]; some curves are multiplied by a power of 10, in order make the image clearer. The graphs on the right shows the same curves as the ones presented on the left for $p_T < 2$ GeV

This lack of sensitivity to T_{fo} can be understood as follows: the average p_T should decrease when the temperature is decreased (there is less thermal energy). At the same time, the fluid velocity has more time to increase and accelerate particles. These two opposing effects compete with each other.

We will see later that the flow coefficients $v_n(p_T)$ are sensitive to the freeze-out temperature. Said quantity must then be chosen to get a good fit for both the $v_n(p_T)$ curves and p_T distributions.

Fig.4.9 shows the p_T distributions in all centrality classes for colliding Pb-Pb nuclei at 2.76 TeV. It is worth noticing that as we approach the more central ones, further the NexSPheRIO calculations are from the experimental data at $p_T \gtrsim 2$ GeV. CPEoS leads to somewhat better results. The freeze-out temperatures are the ones shown in the Table 4.2; their values were chosen in order to fit only the $p_T \lesssim 2$ GeV region as well as adjust adequately the flow harmonics to be discussed in the next section.

4.3 Flow Analysis

When two nuclei collide, they form a highly interactive overlapping region, as depicted in Fig.4.10:

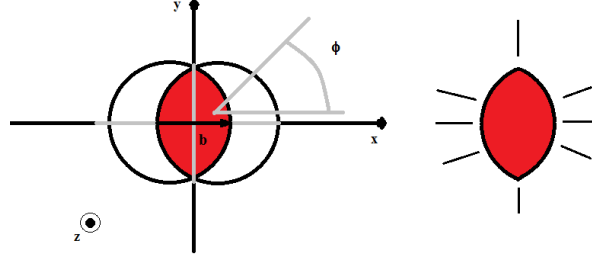


Figure 4.10: Schematic description of the overlapping region (red) resultant of a heavy-ion collision as viewed from the transverse plane, orthogonal to the beam. The azimuthal angle between the emitted particles and the x -axis is denoted by ϕ . The impact parameter vector (\vec{b}) and the z -axis span the reaction plane of the collision. It is worth noticing that the initial shape of the region in red changes with b .

Pressure gradients between the produced particles result in a preferred direction in particle emission: along the short distance of the almond-shaped overlap region. Due to this, the angular particle emission is not isotropic. This observed *azimuthal anisotropy* indicates a collective behavior in the system's evolution[48]. In addition to this, the granularities present in the IC will also cause more complicated anisotropies to arise in the angular particle distribution. The said anisotropies are quantified by expanding the differential particle yield azimuthal distribution in a Fourier series following the method in [49]:

$$E \frac{d^3 N}{d^3 p} = \frac{d^3 N}{p_T dp_T dy d\phi} = \frac{d^2 N}{p_T dp_T dy} \frac{1}{2\pi} \left(1 + \sum_{n=1}^{\infty} 2v_n(p_T, y) \cos [n(\phi - \psi_n)] \right). \quad (4.10)$$

E , ϕ , p_T and y are the particle's energy, azimuthal angle, transverse momentum and rapidity, respectively. The latter is defined as

$$y = \frac{1}{2} \ln \left[\frac{E + p_z}{E - p_z} \right]. \quad (4.11)$$

The event-plane angle, ψ_n points along the steepest pressure gradient for a given n . Moreover, $n = 2$ corresponds to an elliptic deformation, $n = 3$ to a triangular one, etc. Lastly, the coefficients $v_n = v_n(p_T, y)$ are the n -th harmonic differential flow and they are particularly sensitive to initial condition fluctuations. They are given by

$$v_n(p_T, y) = \langle \cos [n(\phi - \psi_n)] \rangle, \quad (4.12)$$

where $n = 1, 2, \dots$ and “ $\langle \rangle$ ” indicates an average over all particles in all events in the (p_T, y) bin under study. Additionally, v_1 , v_2 and v_3 are denoted *directed*, *elliptic* and *triangular* flow, respectively. The first is not studied in this work, because it requires a more complicated treatment when using NexSPheRIO[50].

In the subsequent sections, we shall present a method for extracting the v_n coefficients ($n = 2, \dots, 5$), called *event-plane method* and display its results for different centrality classes, which we compare with CMS and ATLAS measurements from [51, 52, 53].

4.3.1 Event Plane Method

The mentioned method makes use of the anisotropic flow itself to determine the event plane[49]. The latter contains both the direction of the beam and that of the maximal flow determined from the distributions of final-state particles. The event plane can also be computed independently for each v_n . We define the event flow vector Q_n and the event plane angle ψ_n from the n -th harmonic of the distribution as[54].

$$Q_n \cos(n\psi_n) = Q_{nx} = \int_{p_T^{min}}^{p_T^{max}} dp_T p_T^2 \int_0^{2\pi} d\phi \cos(n\phi) \frac{dN}{dy p_T dp_T d\phi}, \quad (4.13)$$

$$Q_n \sin(n\psi_n) = Q_{ny} = \int_{p_T^{min}}^{p_T^{max}} dp_T p_T^2 \int_0^{2\pi} d\phi \sin(n\phi) \frac{dN}{dy p_T dp_T d\phi} \quad (4.14)$$

and

$$\psi_n = \frac{1}{n} \arctan \left[\frac{Q_{ny}}{Q_{nx}} \right], \quad (4.15)$$

respectively.

The collective flow coefficients as functions of the transverse momentum have, then, the following expression:

$$v_n(p_T) = \frac{\int_0^{2\pi} d\phi \frac{dN}{dy p_T dp_T d\phi} \cos[n(\phi - \psi_n)]}{\frac{dN(p_T)}{dy p_T dp_T}}, \quad (4.16)$$

where $dN(p_T)/(dy p_T dp_T)$ is integrated over the azimuthal angle,

$$\frac{dN(p_T)}{dy p_T dp_T} = \int_0^{2\pi} d\phi \frac{dN(p_T)}{dy p_T dp_T d\phi}. \quad (4.17)$$

At last, the integrated v_n 's are given by

$$v_n = \frac{\int_{p_T^{min}}^{p_T^{max}} dp_T p_T \int_0^{2\pi} d\phi \frac{dN}{dy p_T dp_T d\phi} \cos[n(\phi - \psi_n)]}{\int_{p_T^{min}}^{p_T^{max}} dp_T p_T \frac{dN(p_T)}{dy p_T dp_T}}. \quad (4.18)$$

In view of the data used in the next section, it is assumed that $y \sim 0$ for all quantities so above $v_n(p_T)$ and v_n do not depend explicitly on y .

Aside from the event-plane method, others employed in the calculations of flow harmonics are the generating-function-based multiparticle cumulant[55] and the Lee-Yang zeros[56, 57].

4.3.2 Results

In this subsection, we present the NexSPheRIO results of the collective flow coefficients (v_2 , v_3 , v_4 and v_5) for six centrality classes, 0–5%, 5–10%, 10–15%, 15–20%, 20–25% and 25–30%, as delimited by the CMS Collaboration [51, 52]. Using the event-by-event analysis, we obtain the code's output of charged particle momenta for various nuclei-nuclei collisions at 2.76 TeV. We then proceed on calculating the differential number $\frac{dN_{ch}}{d\eta p_T dp_T d\phi}$ of hadrons within $|\eta| < 0.8$, subsequently employing the event-plane method discussed in the previous subsection

in order to obtain $v_n(p_T)$. CMS uses pseudorapidity (η) instead of rapidity (y) [51, 52]. For this specific case, we make $p_{Tmin} = 0.15$ GeV and $p_{Tmax} = 4.15$ GeV, though the graphs only show $v_n(p_T)$ within $0.3 \text{ GeV} < p_T < 2.2 \text{ MeV}$, which is an interval of great interest in hydrodynamic studies.

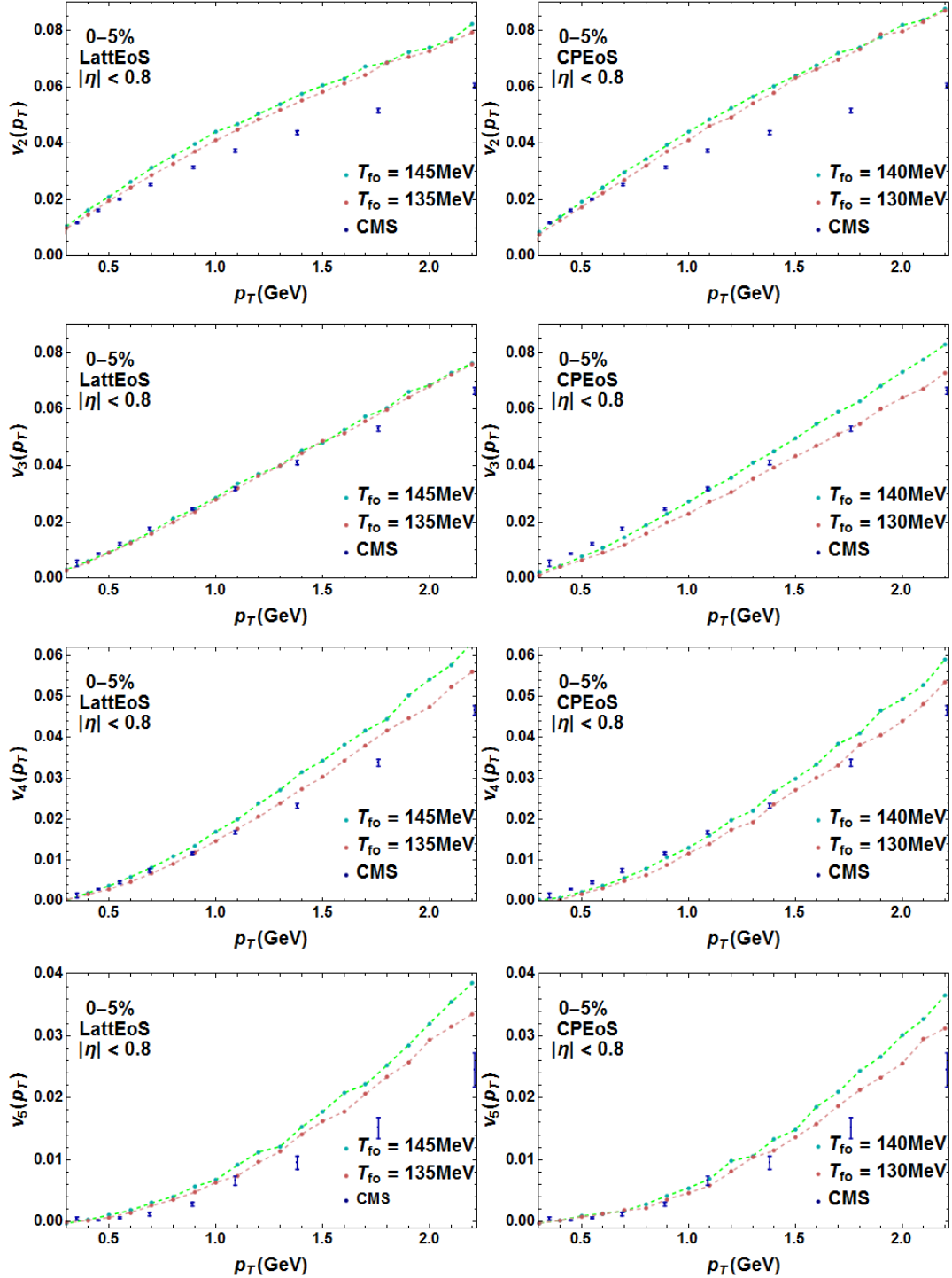


Figure 4.11: Harmonic flows as a function of the transverse momentum for both EoS, at different freeze-out temperatures, in the 0–5% centrality class within the pseudorapidity interval $|\eta| < 0.8$. The points with error bars correspond to the CMS Collaboration’s measurements discussed in [51, 52].

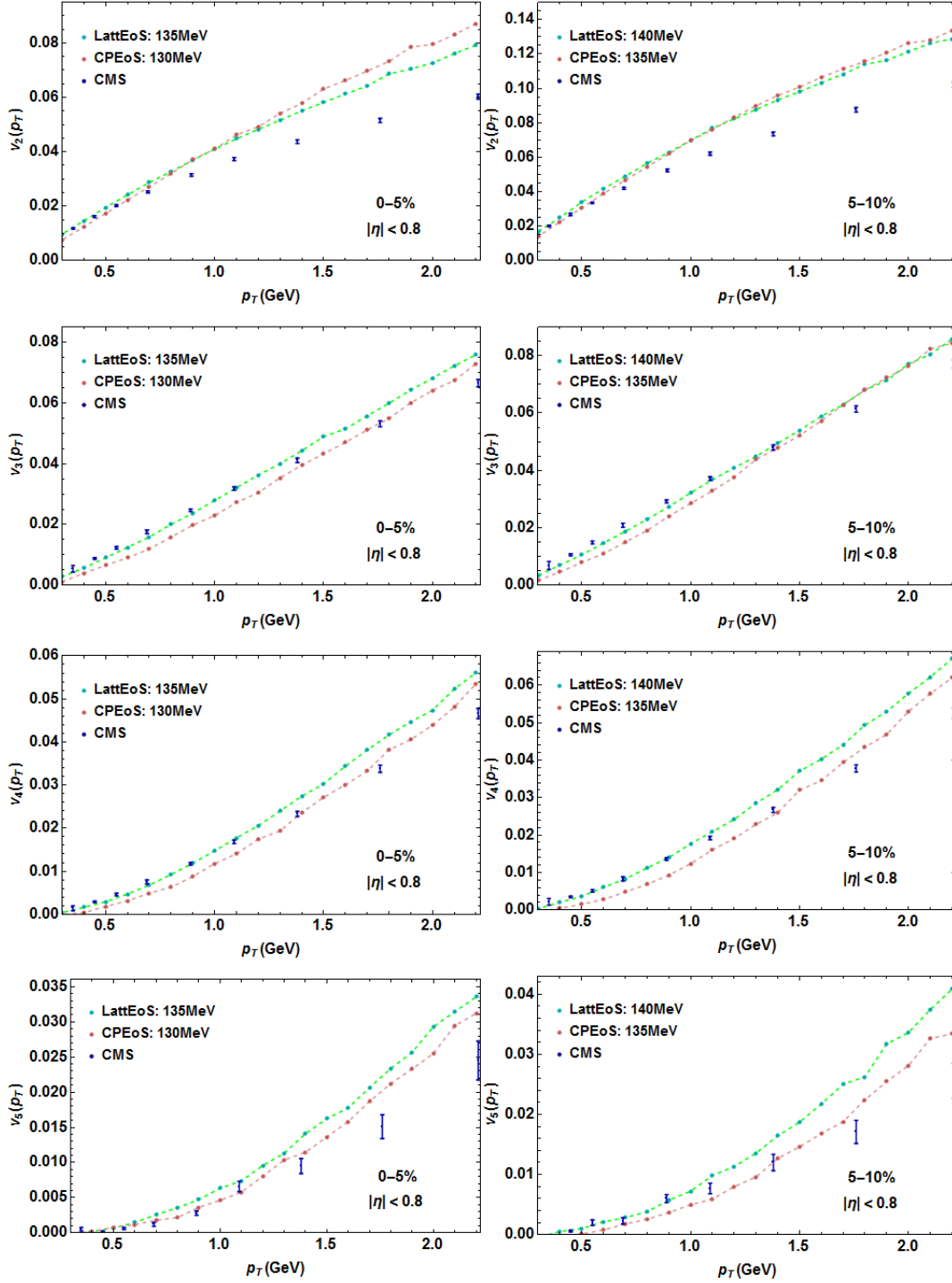


Figure 4.12: Collective flow coefficients as a function of the transverse momentum in the 0–5% and 5–10% centralities. The quantities in MeV units are the freeze-out temperatures correspondent to each EoS and centrality. We compare the NexSPheRIO results (dashed lines) to the CMS measurement (graphs with error bars) from [51, 52].

When analyzing the p_T spectra of particles, we mentioned that the freeze-out temperatures (Table 4.2) were calibrated also taking the flow harmonics into account. In order to study how

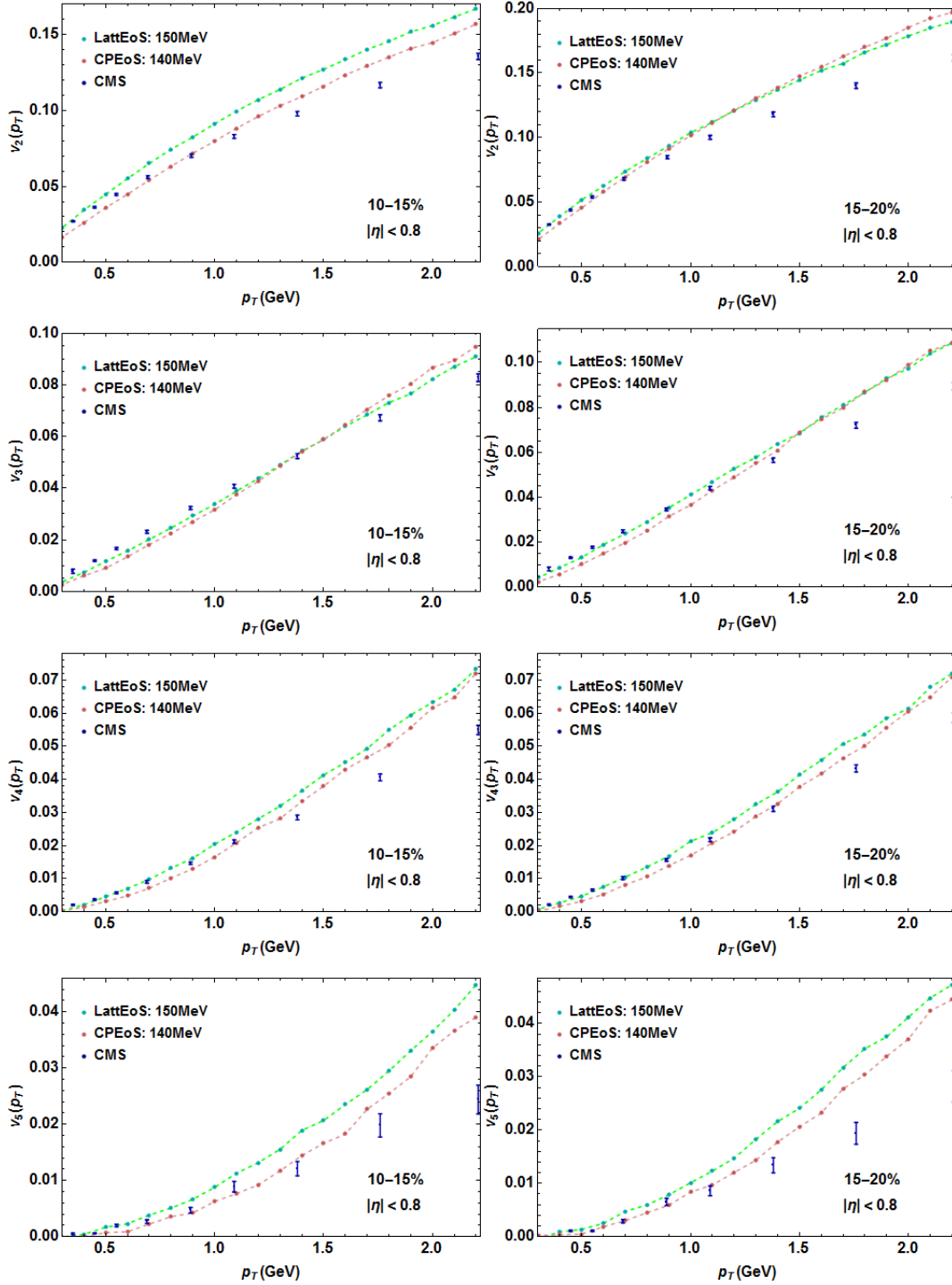


Figure 4.13: Harmonic flows from v_2 to v_5 as functions of p_T for LattEoS and CPEoS in the centrality classes of 10–15% and 15–20%. The results are compared to the CMS data.

they behave with changing T_{fo} , we computed $v_n(p_T)$ at $T_{fo} = 135$ MeV and 145 MeV for LattEoS as well as at $T_{fo} = 130$ MeV and 140 MeV for CPEoS in the 0–5% window. Fig. 4.11 shows the results of such calculations. Basically, higher freeze-out temperatures yield higher $v_n(p_T)$ values. Also, the difference between the v_3 results for the LattEoS is rather small.

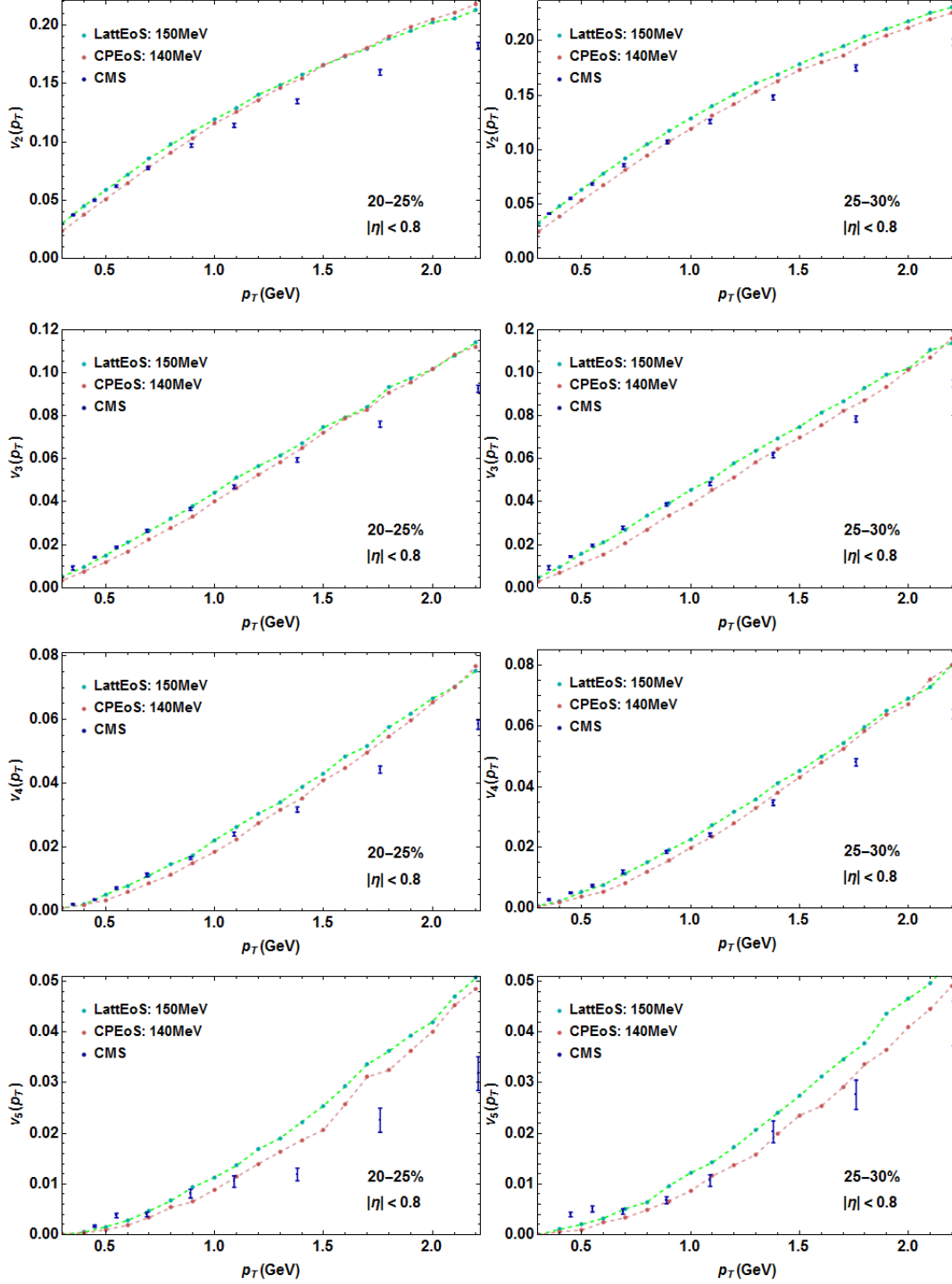


Figure 4.14: Comparison between the experimental $v_n(p_T)$ results from the CMS Collaboration and the ones calculated with NexSPheRIO for the 20–25% and 25–30% centrality classes using LattEoS and CPEoS.

CPEoS results are closer to the experimental curve for v_2 and v_5 at the low p_T region ($p_T \lesssim 1.0$ GeV) in comparison to the LattEoS. One could argue that, by setting the freeze-out temperature higher, the v_3 and v_4 results would get closer to the CMS data. However, such action also implies in distancing the v_2 and v_5 curves from the latter. We settle for $T_{fo} = 130$ MeV in this case.

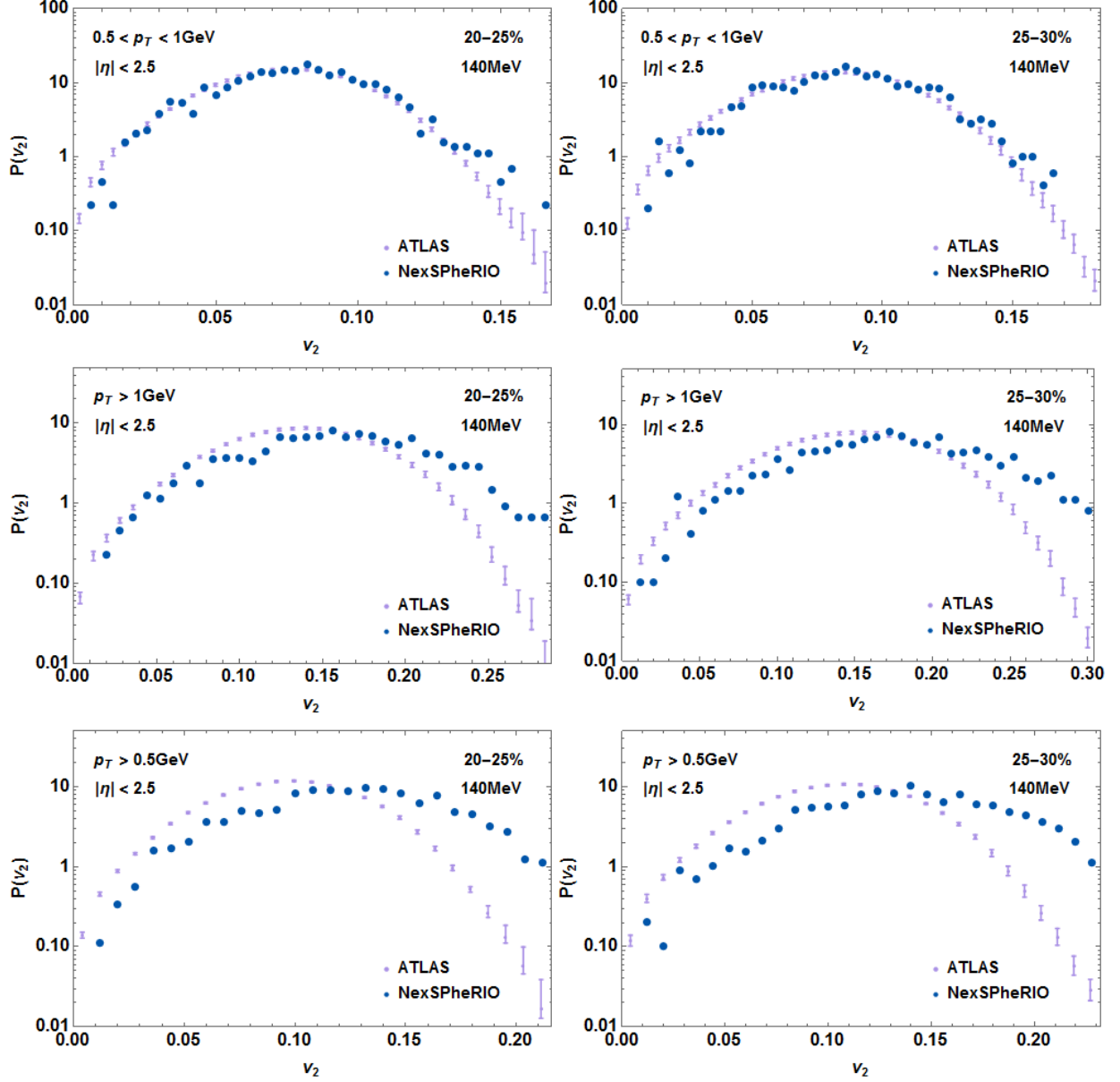


Figure 4.15: Integrated elliptic flow distribution for the centrality classes of 20–25% and 25–30% at $T_{fo} = 140$ MeV evaluated in $0.5 < p_T < 1$ GeV, $p_T > 1$ GeV and $p_T > 0.5$ GeV for the CPEoS. In light purple are the ATLAS measurements extracted from [53]. The pseudorapidity interval is $|\eta| < 2.5$.

On the other hand, LattEoS describes better the v_3 and v_4 coefficients at low p_T in contrast to the CPEoS. At this point, it is important to remark that, if we were to lower its T_{fo} in order to approximate the curves to the experimental v_2 result, the LattEoS p_T spectrum of 0–5% would distance itself from the ALICE measurements (at $p_T < 2.0$ GeV). A higher T_{fo} would fit better the latter, but worsen the elliptic flow result. Hence the importance of choosing a freeze-out temperature that yields reasonable results for both, instead of just one; $T_{fo} = 135$ MeV in this case.

Having discussed the sensitivity of the flow harmonics to changes in the freeze-out temperature for both EoS, we calculate $v_n(p_T)$ for all the centralities mentioned in the first paragraph.

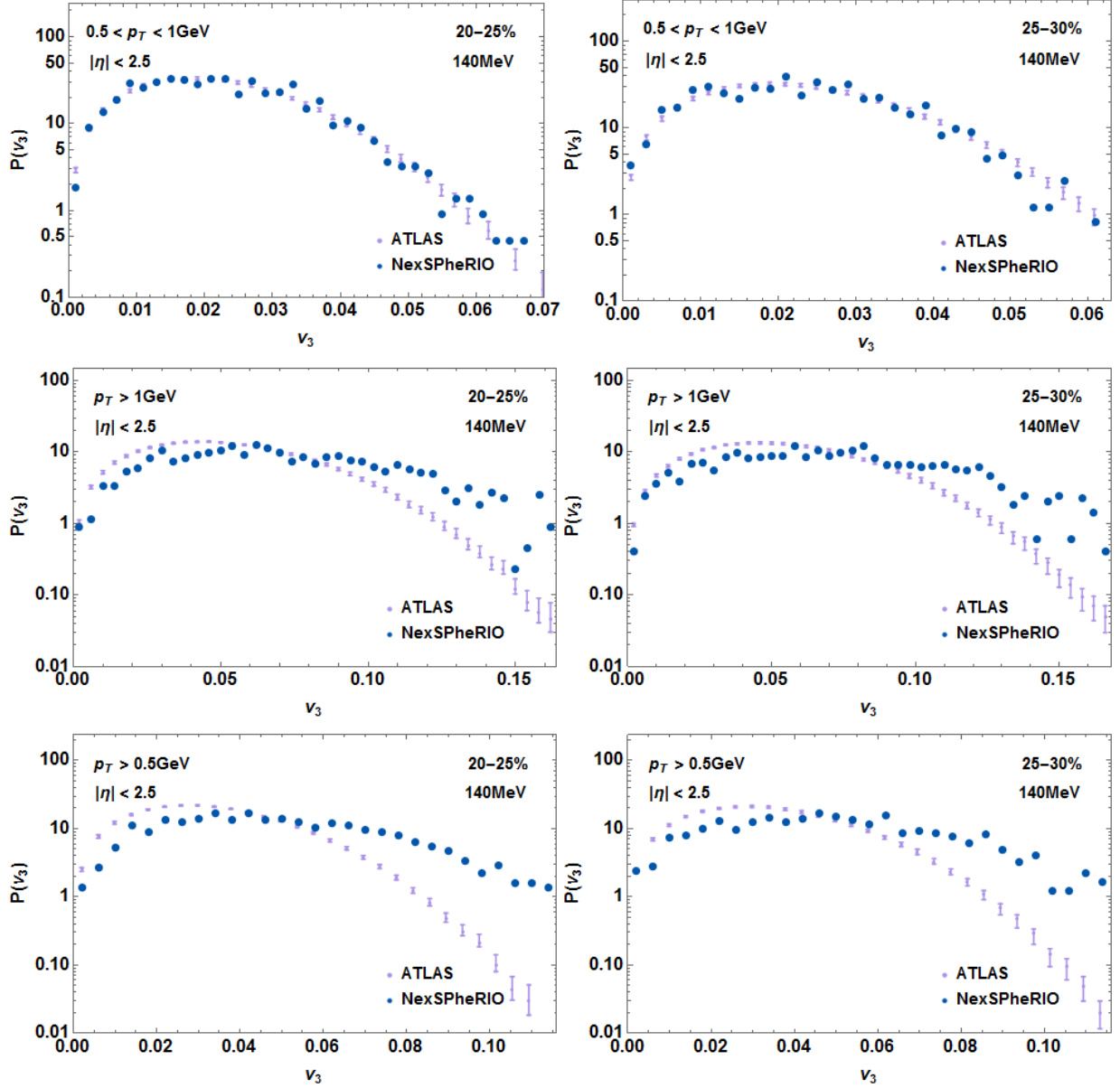


Figure 4.16: Integrated triangular flow distribution within $|\eta| < 2.5$ with CPEoS for 20–25% and 25–30% as well as the transverse momentum intervals $0.5 < p_T < 1 \text{ GeV}$, $p_T > 1 \text{ GeV}$ and $p_T > [0.5] \text{ GeV}$. We compare with ATLAS data; $T_{fo} = 140 \text{ MeV}$.

The values of T_{fo} are the ones from Table 4.2.

It is clear from Figs. 4.12, 4.13 and 4.14, that more central collisions have lower $v_2(p_T)$ values than peripheral ones. The initial geometry of the former is closer to that of a circle than an almond-shaped one, which is characteristic of latter. The values of $v_{n>2}(p_T)$ for all centrality classes as well as $v_2(p_T)$ for the 0–5% window are smaller, since they come from fluctuations.

Just like before, the LattEoS results fit better v_3 and v_4 , while the ones from CPEoS are closer to v_2 and v_5 . Similarly to the p_T spectra case, higher centrality classes yield results that are a little better adjusted to the experimental data. Additionally, the NexSPheRIO calculations are reasonably closer to the CMS measurements for $p_T \lesssim 1.0 \text{ GeV}$, just like in the

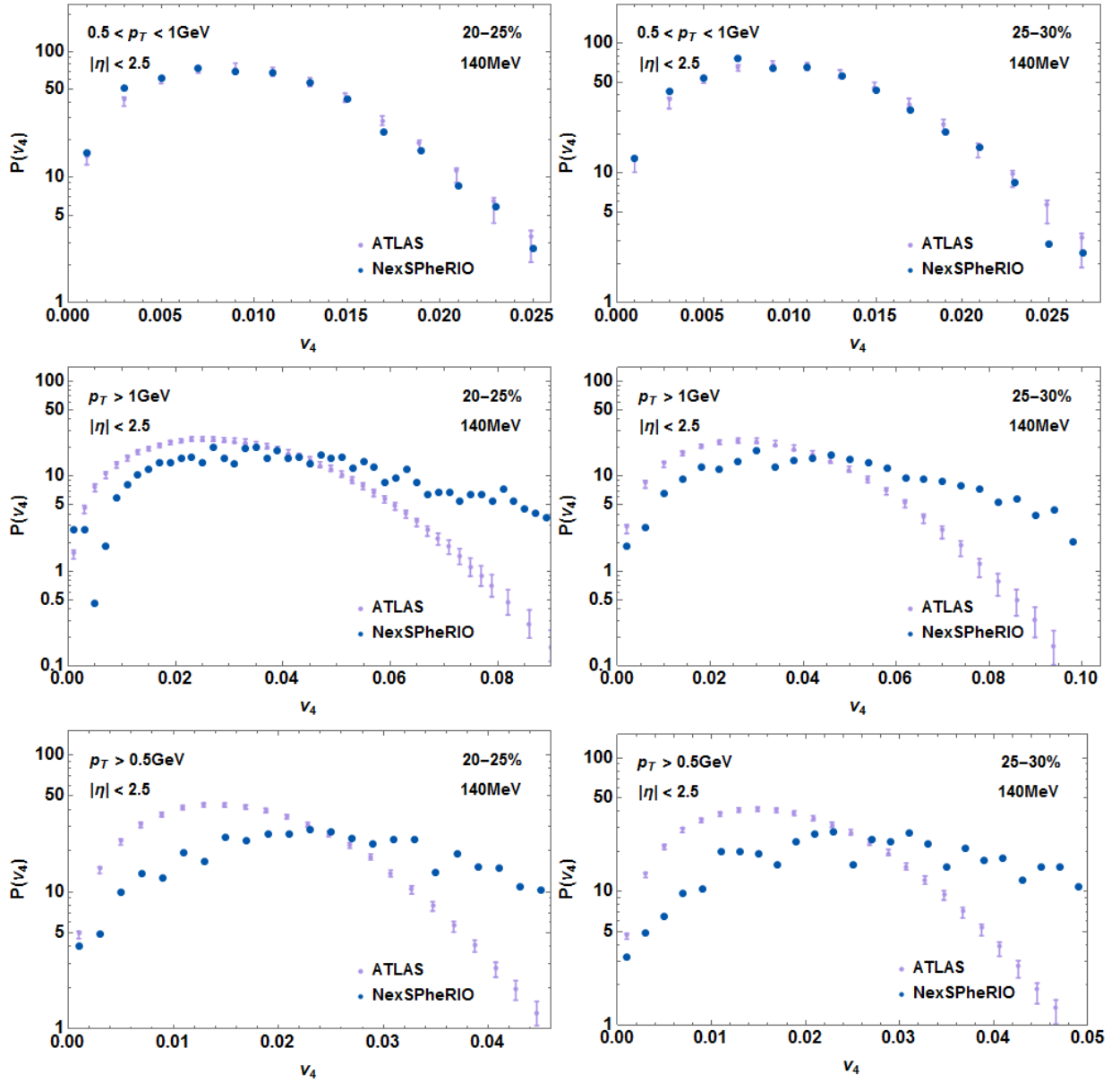


Figure 4.17: Distribution of the integrated collective flow coefficient, v_4 for 20–25% and 25–30% at $T_{fo} = 140$ MeV. Just like in the $P(v_2)$ and $P(v_3)$ calculations, we employed the CPEoS and computed the particle spectrum within the $0.5 < p_T < 1$ GeV, $p_T > 1$ GeV and $p_T > 0.5$ GeV intervals. ATLAS is represented by the light purple points; $|\eta| < 2.5$.

transverse momentum distribution comparisons.

So far, we have discussed $v_n(p_T)$ averaged over events. In order to study more closely the IC fluctuations, it is interesting to look at the p_T -integrated v_n 's. So, our last step in the flow analysis consists in computing the integrated v_n 's as in eq. (4.18). We then calculate the distributions of the flow harmonic coefficients v_n ($n = 2, 3, 4$) for charged particles with $0.5 \text{ GeV} < p_T < 1.0 \text{ GeV}$, $p_T > 1.0 \text{ GeV}$ and $p_T > 0.5 \text{ GeV}$ in the $|\eta| < 2.5$ interval, as measured by the ATLAS Collaboration in [53]. The aforementioned is performed for the 20–25% and 25–30% centrality classes with the CPEoS and $T_{fo} = 140$ MeV. We ran 1109 events for the former and 1233 for the latter.

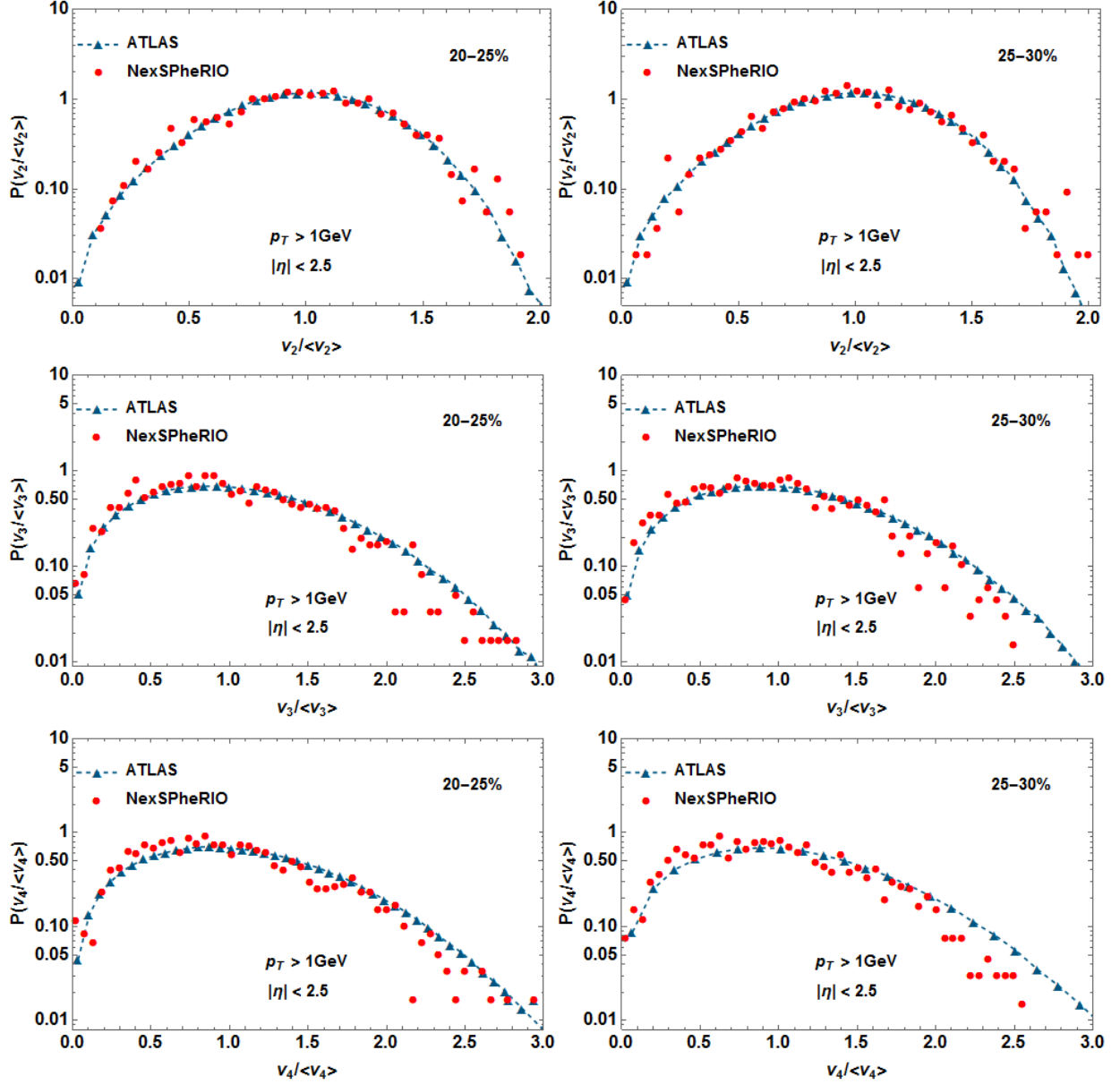


Figure 4.18: We present the distributions of the flow harmonics (v_2 , v_3 and v_4) rescaled by the mean for the 20–25% and 25–30% centralities, in the $p_T > 1$ GeV and $|\eta| < 2.5$ intervals. Comparison with ATLAS data[53].

It is clear from Figs. (4.15, 4.16, 4.17) that the NexSPheRIO results under the aforementioned conditions fit rather well the ATLAS measurements in the $0.5 < p_T < 1$ GeV region, for v_2 , v_3 and v_4 . In the end, not only the average values of v_n but also their fluctuations among events are reproduced.

In the $p_T > 1$ GeV and $p_T > 0.5$ GeV cases, we set $p_{Tmax} = 4.0$ GeV, since the number of particles with said transverse momentum is almost zero. NexSPheRIO results are reasonable for low values of v_2 and v_3 but underpredict data for low values of v_4 in both centralities. For larger values of these flow coefficients, there are too many events compared to the ATLAS data.

This is in agreement with the fact that the $v_n(p_T)$ curves are above data for larger p_T .

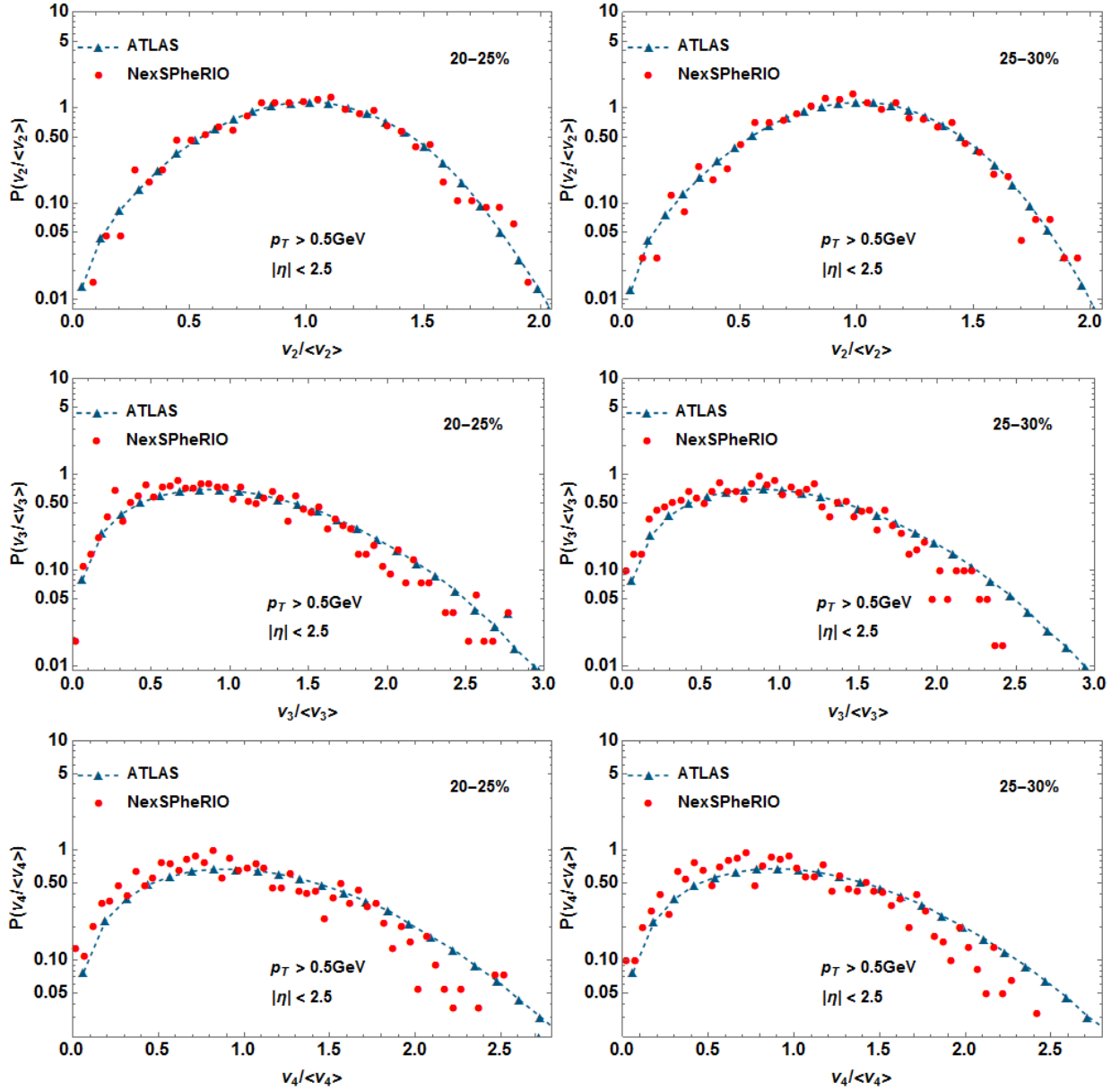


Figure 4.19: Distributions of the flow coefficients (v_2 , v_3 , v_4) rescaled by their own mean in comparison to the ATLAS data [53]. They are calculated within the $p_T > 0.5 \text{ GeV}$ and $|\eta| < 2.5$ intervals.

An interesting comparison can be made by rescaling the harmonic flow distributions by the mean, as in [58]. We plot $P(v_n / \langle v_n \rangle)$, where $\langle v_n \rangle$ is the mean value of v_n in the correspondent p_T interval, instead of $P(v_n)$.

The NexSPheRIO results fit the ATLAS measurements for $p_T > 1 \text{ GeV}$ and $p_T > 0.5 \text{ GeV}$ quite well, even for $n = 3, 4$, when $v_n / \langle v_n \rangle \lesssim 1.5$, as we can see from Figs. 4.18 and 4.19. However, these distributions tend to be a little too narrow.

In summary, we have shown that the Nexus model [6] alongside with the SPheRIO code

give good agreement with the ATLAS experimental data on $P(v_n)$ in the $0.5 < p_T < 1$ GeV interval for both centrality classes and all harmonic flow coefficients (v_2 , v_3 , v_4) distributions. The same can be said for the remaining transverse momentum intervals when the latter was rescaled by their own mean, as discussed above. We can thus conclude that NexSPHERIO has approximately the right fluctuations in its initial conditions to reproduce those seen in experimental data. The latter can be useful when comparing results from different initial condition generators (not treated in this work).

4.4 Comparison with RHIC

The Relativistic Heavy-Ion Collider (RHIC) is a pre-LHC particle accelerator that smashes gold nuclei against each other at incident energies up to 200 GeV. Its data have been extensively studied and still are until today. Due to their distinct initial settings, especially in the beam energy (of order ten), it is of great interest to make a comparison between both colliders.

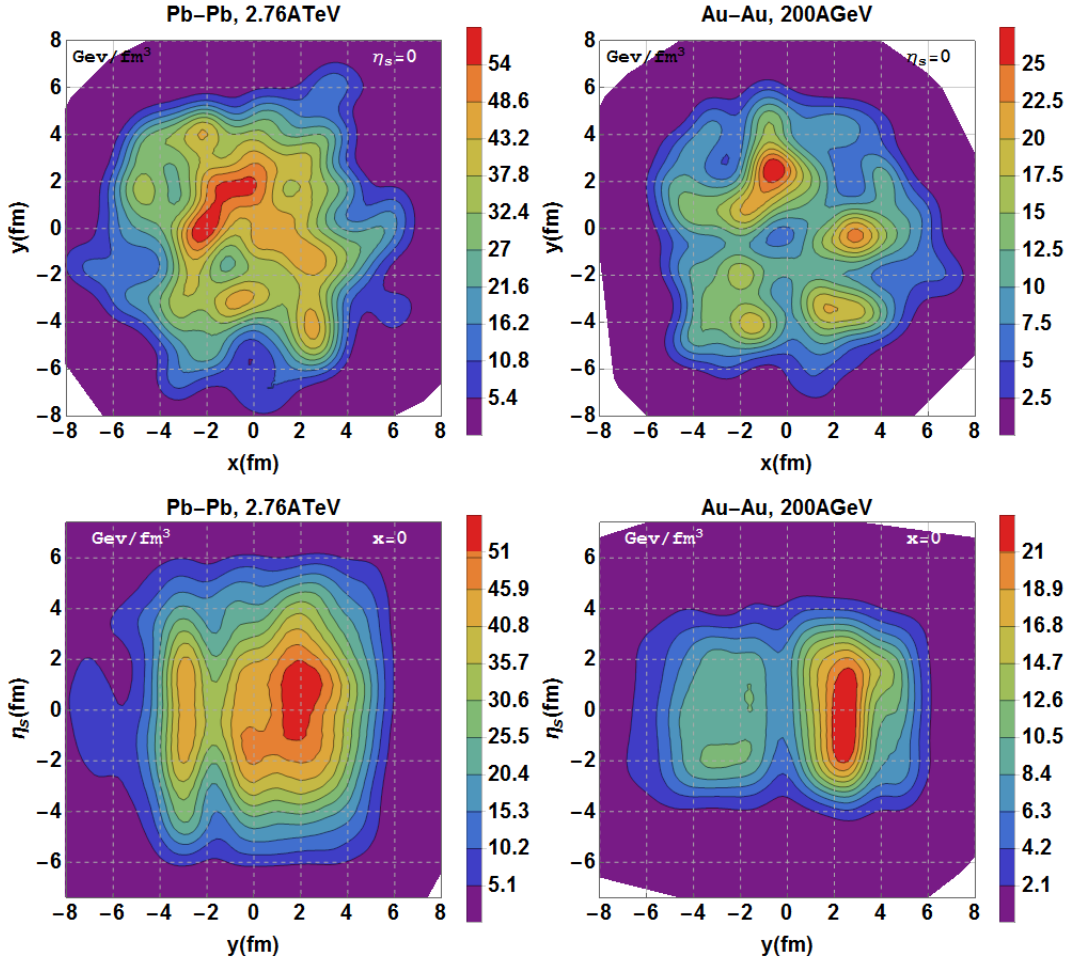


Figure 4.20: Comparison between Nexus single-event results for most central Pb-Pb collisions at incident energy 2.76 ATeV (left column) and most central Au-Au collisions at incident energy 200 AGeV (right column). The former’s number of participants is 387 and the latter’s is 345.

The first comparison made between LHC and RHIC calculations is that in the initial energy distributions generated by Nexus. The colliding lead nuclei in the former particle accelerator

have an atomic mass number of 208 each whereas the latter's gold nuclei possess a mass number of 197. The beam energy at LHC is of 2.76 ATeV, while for RHIC, it is 200 AGeV. Examples of normalized energy density for both cases are shown in Fig. 4.20.

In terms of overall structure, the LHC (left column) and RHIC (right column) based Nexus outputs are relatively similar: both present fluctuating energy density values, as expected from a single-event ϵ_0 distribution. On the other hand, the results for 2.76 TeV can reach peak values ~ 2 times higher than the ones from 200 GeV. The cause of such divergence is majorly due to the difference of order 10 between each case's incident energy, since the additional 42 participants would not cause ϵ to vary so much.

We can also analyze the differences between the original initial conditions generated by Nexus. Fig. 4.21 displays the results for the same events presented above. The highest energy density values reached in the Pb-Pb collision are now closer to the highest ones from the Au-Au case. The LHC ϵ_0 distribution is spread throughout a wider area than the RHIC one, reflecting the higher beam rapidities. We can conclude that the system's total energy in the LHC-based collision is higher than in the RHIC-based one.

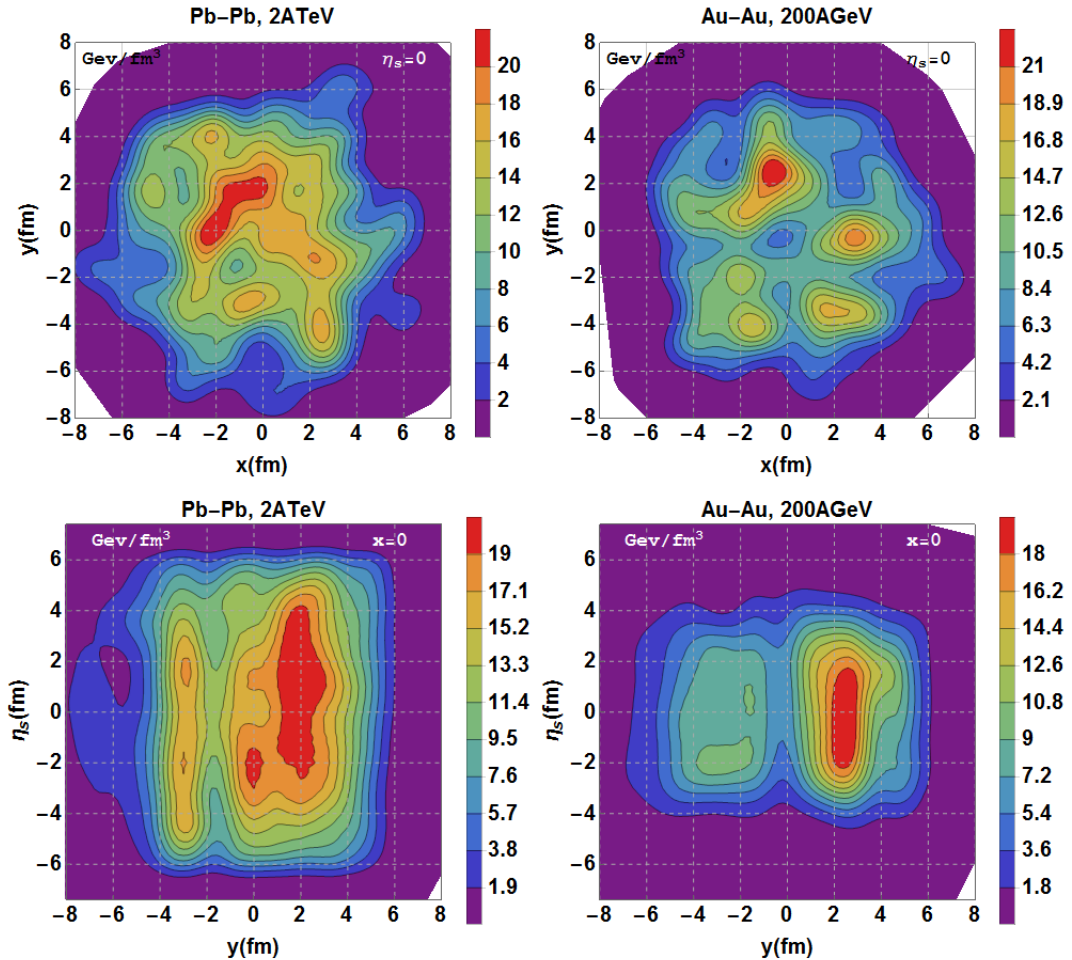


Figure 4.21: Non-normalized initial energy density generated by Nexus for a single Pb-Pb collision at 2 ATeV (left column) and for a single Au-Au collision at 200 GeV (right column). The events depicted above are the same as in Fig. 4.20

When taking the energy densities of each event in comparison to their respective normalized counterparts, we notice that the correction needed for the Pb-Pb results is greater than that of Au-Au results. The first has its normalized energy peak roughly twice as high as the originals, whereas the difference between ϵ_0 peaks for the latter is much smaller. Said situation can be clearly seen by comparing the $f(\eta)$ correction functions for both the LHC and RHIC cases, as we will subsequently discuss. In part, this is due to the fact that for LHC, NexSPheRIO is run at 2 ATeV, instead of 2.76 ATeV

Fig. 4.22 depicts the calculations of $dN_{ch}/d\eta$ using both corrected and original IC. The ALICE collaboration divides the centrality classes for Pb-Pb collisions at 2.76 ATeV in a different way than PHOBOS does for Au-Au collisions at 200 AGeV. Hence, we compare the results in the 20–30% and 15–25% centralities, respectively. The original LHC-based curve (dashed line) reaches up to $dN_{ch}/d\eta \sim 370$, whereas in the RHIC-based case the maximum value for the η distribution is $dN_{ch}/d\eta \sim 320$. We must, however, take a look at the whole picture. For $|\eta| = 5$, the Pb-Pb non-corrected result has $dN_{ch}/d\eta$ above 200, while for Au-Au its value is, approximately, 70. The latter’s curve decreases more rapidly than the former’s, meaning that the total number of produced charged particles in the 20–30% non-normalized Pb-Pb collisions is, as expected, quite above the 15–25% non-normalized Au-Au N_{ch} value. The Pb-Pb curve extends to large η ’s, as expected.

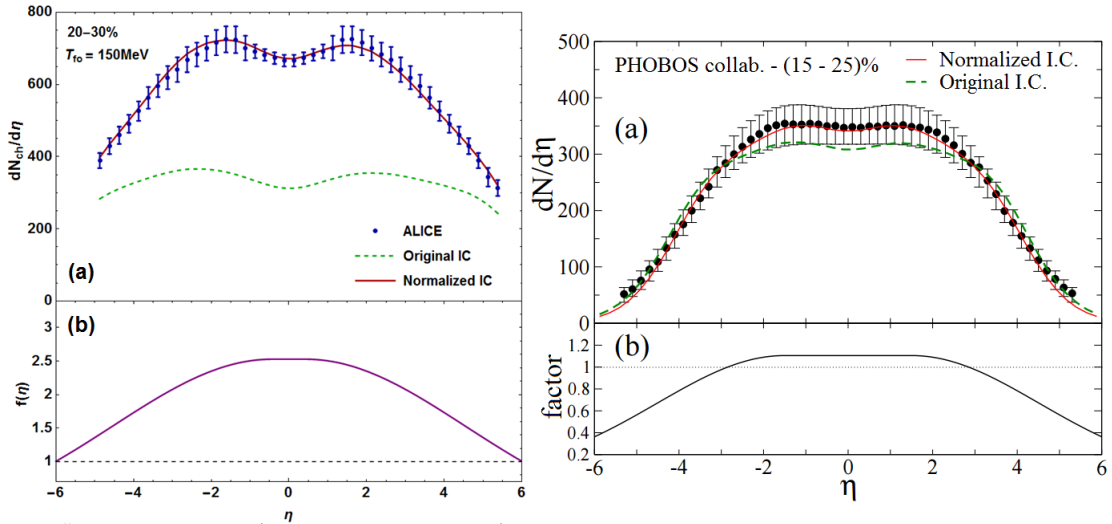


Figure 4.22: **(a)** Pseudorapidity distribution of charged particles for the 20–30% and 15–25% centralities in the LHC and RHIC cases, respectively. We show the results for normalized (continuous lines) and original (dashed lines) initial conditions in comparison with the experimental data. Both were calculated using the CPEoS. **(b)** Factor function $f(\eta)$ responsible for the uplift of the non-normalized distributions. The dashed black line represents $f(\eta) = 1$. The figure on the right was extracted from [40].

The need for a higher correction in the IC at LHC in relation to RHIC discussed above is also illustrated by the height of their respective $f(\eta)$.

After the IC rescaling, we can compare the normalized charged particle pseudorapidity distribution results for the remaining centrality classes (Fig. 4.23). The fits are of similar quality.

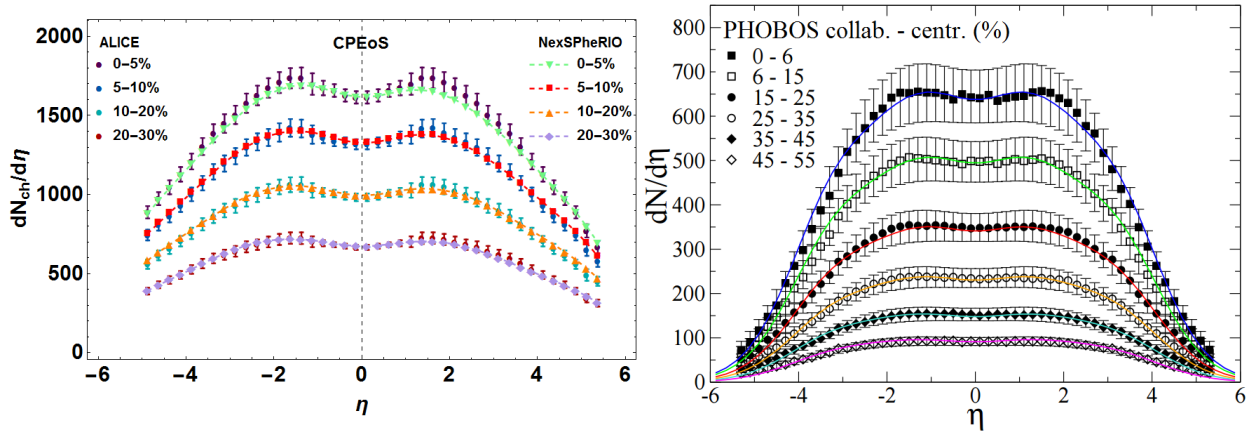


Figure 4.23: Final charged particle distributions in terms of η to all centrality classes studied in this work (left) and in reference [40] (right). Those are results for the CPEoS and we compare them to the measurements performed by ALICE (left) and PHOBOS[59] (right) collaborations.

We now turn our attention to the matter of transverse momentum distributions. Fig. 4.24 depicts their results for both lead and gold nuclei colliding at 2.76 ATeV and 200 AGeV, respectively. The first is analyzed within the $|\eta| < 0.8$ range and the latter in the $0.2 < y < 1.4$ interval, where y is the rapidity. CPEoS (CEP) and LattEoS (LQCD) were employed in the calculations.

One may notice that the behavior with EoS is quite similar for both cases. CPEoS fits the experimental data reasonably well until $p_T \sim 2$ GeV, while LattEoS remains slightly above.

The freeze-out temperature range for the LHC-based calculations goes from $T_{fo} = 130$ MeV (0–5%) to $T_{fo} = 140$ MeV (20–30%) in the CPEoS case and from $T_{fo} = 135$ MeV (0–5%) to $T_{fo} = 150$ MeV (20–30%) in the LattEoS case. According to [60], T_{fo} spans over values from 128.16 MeV (0–6%) to 136.96 MeV (25–35%) for both EoS in the RHIC-based case. Reference [40] has approximately the same result for the T_{fo} range as [60]. The LHC freeze-out temperatures have somewhat higher values than the RHIC ones. When considering the difference in initial energy and that the same EoS were used, one may conclude that the system’s expansion time in LHC collisions is longer than in RHIC’s.

The effect of the EoS on the $v_n(p_T)$ ’s is being studied by Dr. D. Dudek as a follow up of the $v_2(p_T)$ study in [60]. Results for these quantities in the CPEoS case were published in [62]. The results for $v_2(p_T)$ are worse than at RHIC for the most central windows, but $v_3(p_T)$ and $v_4(p_T)$ are better. In other centralities, results at LHC and RHIC are of comparable quality. Such differences can be seen in Fig.4.25. No p_T -integrated v_n distributions are available from RHIC.

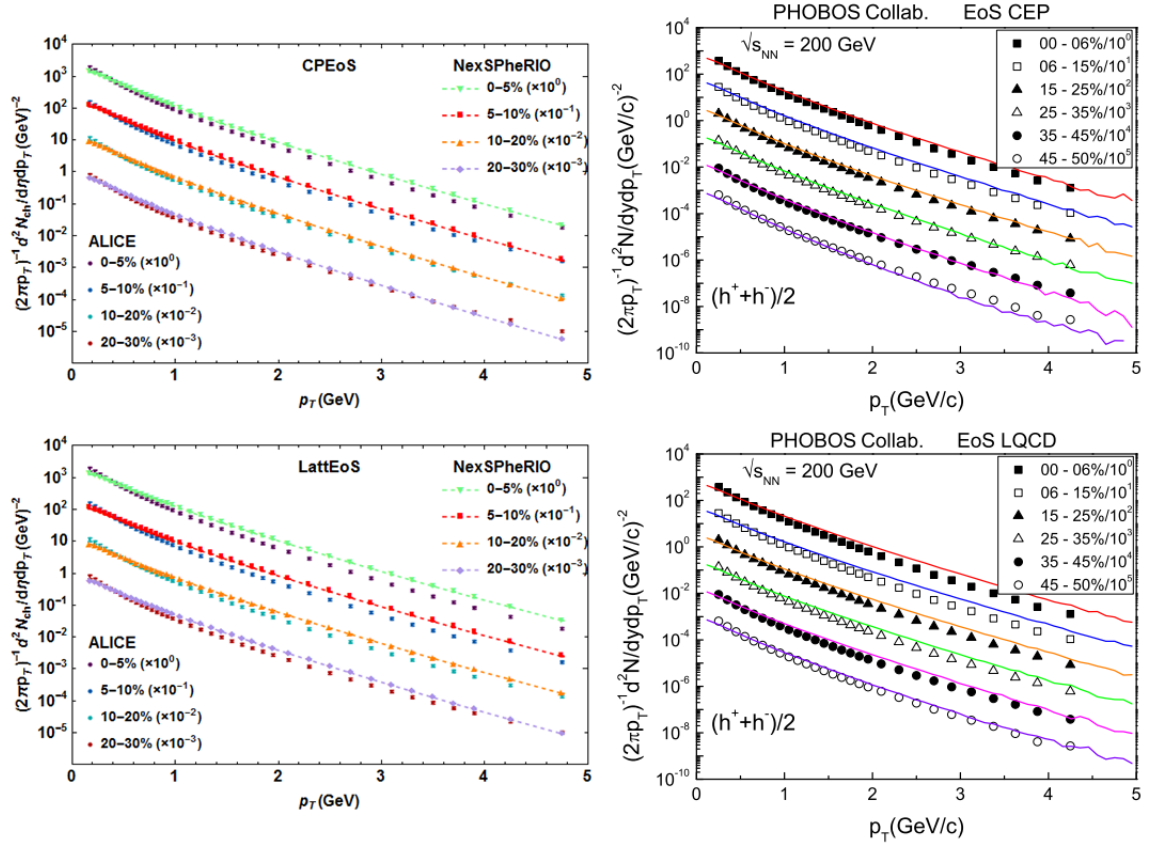


Figure 4.24: Transverse momentum distributions calculated using NexSPheRIO (both cases) for the lattice-based (bottom row) and critical point (top row) equations of state. We compare the results obtained from Pb-Pb collisions at 2.76 TeV (left column) with the ones from Au-Au collisions at 200 GeV (right column). The latter was extracted from the work in [60]. A comparison is made with the experimental data of ALICE[47] and PHOBOS[61].

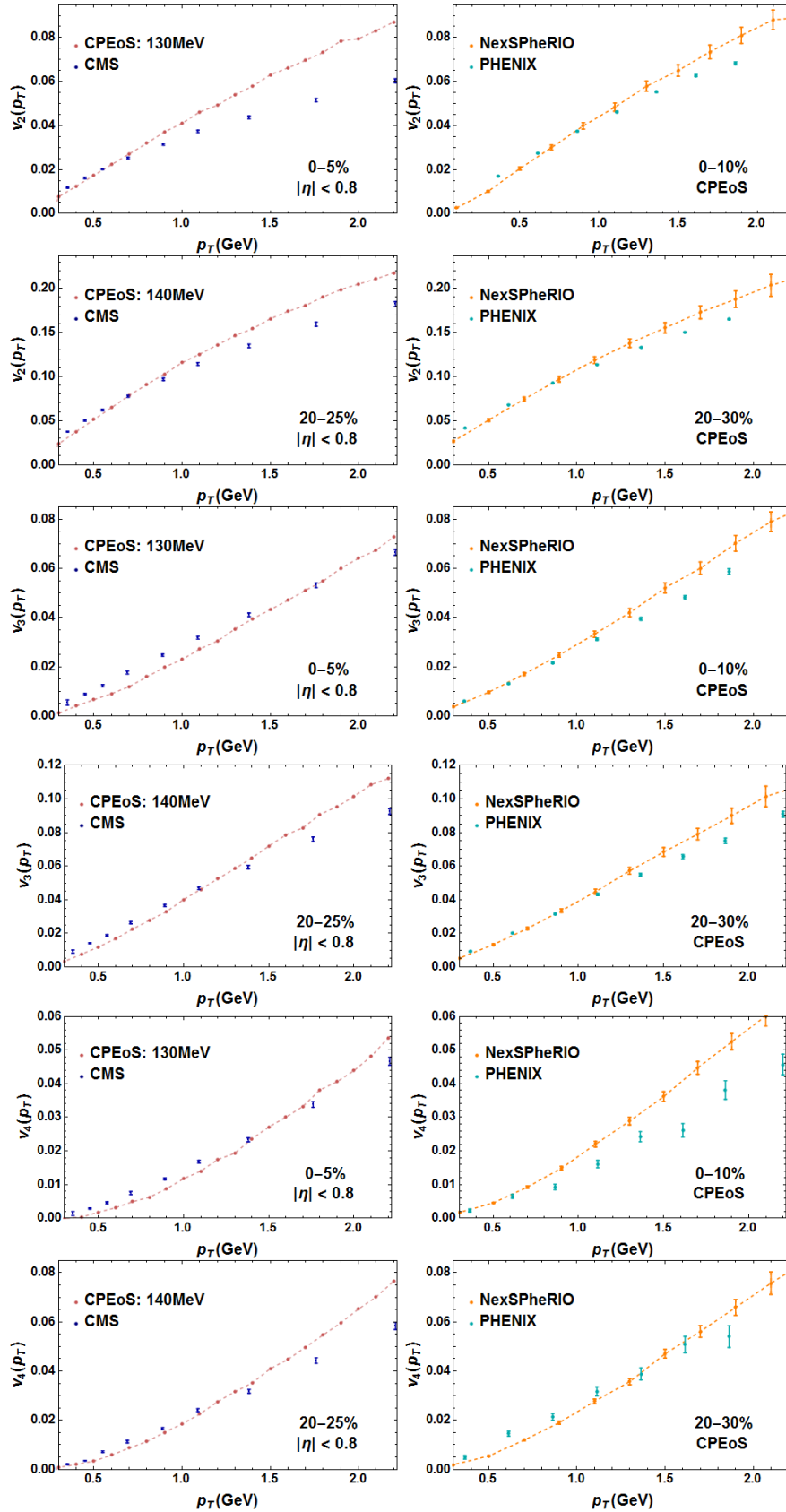


Figure 4.25: Comparison between the LHC (left) and RHIC (right) based calculations performed with NexSPheRIO using the CPEoS at the centralities of 0–5% and 20–25% for the former as well as 0–10% and 20–30% for the latter. The RHIC data was extracted from the work in [62].

Chapter 5

Conclusion

In this work, we applied event-by-event hydrodynamics in order to simulate the LHC heavy-ion experiments: lead nuclei colliding at incident energy of 2.76 ATeV. When performing such task, one must determine a set of ingredients, such as the system’s initial conditions (IC), the equation of state that dictates the relations between the thermodynamic variables and the freeze-out scenario. We generated the IC by making use of the Nexus model, which gives as output the energy-momentum tensor as well as the baryon, strangeness and electric charge currents. Secondly, two distinct EoS were discussed, one with $\mu_B \neq 0$, characterized by a critical point $((\mu_B)_c, T_c)$ where the phase transition changes from first-order to a crossover type (CPEoS) and a baryonless LatticeQCD-based one (LattEoS). Finally, we adopted the Cooper-Frye decoupling mechanism, for which the particles momenta freeze after crossing a hypersurface defined by the isotherm $T(t, x, y, z) = T_{fo}$. The next step consisted in solving the equations of motion of hydrodynamics (introduced in section 2.1) by making use of the SPH method.

With the main ingredients and computing method established, we moved on to making an analysis of the relation between impact parameter (b) and number of participants in a collision (N_p), in order to define their values for each centrality class. The latter were divided as in the ALICE collaboration [46, 47]. Being able to “choose” how central or peripheral a collision would be, we then ran the NexSPheRIO code at 2 ATeV, thus obtaining first the results on charged particle distributions in terms of pseudorapidity. Since the aforementioned had insufficient initial energy to produce the expected number of particles, we introduced a correction function dependent on η with the objective of normalizing the Nexus-generated IC to be usable at the 2.76 TeV beam energy. The parameters of $f(\eta)$ were calculated for the most central collisions (0–30%) and claimed different values for each EoS. The latter were also found to have distinct freeze-out temperatures at given centrality. The final $dN_{ch}/d\eta$ plots fit satisfactorily the ALICE experimental data.

The effect of T_{fo} in the particle spectra was then observed when we computed the charged particle distribution in terms of transverse momentum in the $|\eta| < 0.8$ region. The LattEoS curve ended up being less steep than the CPEoS one at a given freeze-out temperature. The former’s result fit the ALICE measurements reasonably well for $p_T \lesssim 1$ GeV, whereas the latter did the same for $p_T \lesssim 2$ GeV. They would adjust quite well to the experimental results in the region of interest ($p_T < 2$ GeV) the more peripheral were the centralities. The T_{fo} values were defined as to best fit the LattEoS and CPEoS curves to the ALICE data on p_T distribution, while still giving a reasonable result to the flow harmonics.

Having defined the correction function's parameters as well as the freeze-out temperature for each centrality class and EoS, we analyzed how the flow coefficients change with transverse momentum ($v_n(p_T)$). By employing the event-plane method, we obtained from the NexSPheRIO results on $\frac{dN_{ch}}{y p_T dp_T d\phi}$ ($|\eta| < 0.8$) the curves for the flow harmonics v_2 , v_3 , v_4 and v_5 as functions of p_T . We found that the $v_n(p_T)$ curves get higher with increasing T_{fo} , in a manner that, depending on the chosen value, the graphs could fit either v_2 and v_5 or v_3 and v_4 better. Such observation called for a calibration of T_{fo} , in order to obtain a result that would adjust reasonably to all p_T dependent quantities. Overall, the flow coefficient ($v_n(p_T)$) calculations for both EoS at all given centralities were in sensible agreement with the CMS measurements in the $p_T \lesssim 1$ GeV region.

After computing $v_n(p_T)$, we looked at integrated v_n ($n = 2, 3, 4$) distributions in the 20–25% and 25–30% centrality classes, using CPEoS, for three p_T intervals, $0.5 < p_T < 1$ GeV, $p_T > 1$ GeV and $p_T > 1$ GeV, as well as $|\eta| < 2.5$. In the case of $0.5 < p_T < 1$ GeV, the results adjusted well to the ATLAS collaboration measurements, for all flow harmonics at hand. Since the same cannot be said for the other two intervals, we rescaled by the mean value $\langle v_n \rangle$, thus calculating $P(v_n)/\langle v_n \rangle$. We find the curves to fit the rescaled ATLAS data reasonably, though they are a little too narrow for $n = 3, 4$. This type of calculation had never been done before for NexSPheRIO. It shows that not only the code leads to good results for the event-averaged $v_n(p_T)$'s, but also has the right amount of fluctuations in its IC to produce the correct v_n 's on an event-by-event basis.

Finally, we made comparisons of our results to previous NexSPheRIO calculations for RHIC, which are found in references [40, 60]. We begin by analyzing the Nexus-generated IC for the most central collisions in both cases. When they are normalized, the energy density peaks of Pb-Pb collisions at 2.76 ATeV reaches a factor 2 above e_0 that for Au-Au collisions at 200 AGeV. The correction that needs to be applied in order to get the normalized IC is larger at LHC than at RHIC (in part due to a technical limitation in NexSPheRIO). The quality of the fits to the pseudorapidity distributions then obtained is similar for both colliders.

Subsequently, we compared the results in charged particle distributions in terms of transverse momentum in the LHC and RHIC scenarios. We observe that the fits are of similar quality and share common characteristics for changes in centrality and equation of state. We then finally argued that the quality of the fits for the $v_n(p_T)$'s are not very different, except for $v_2(p_T)$ at the most central collisions.

All in all, the NexSPheRIO results of event-by-event hydrodynamics adjust well to the measurements performed by LHC detectors, ALICE, CMS and ATLAS. This is surprising: it is usually expected that gluon saturation effects should be manifest at LHC and the IC, unlike the Nexus' ones, should incorporate this. We note, however, that the present analysis must be extended to the remaining centralities and could be done for various particle types, instead of just charged particles. In addition, we could further the studies on LHC by calculating the Hambury-Brown-Twiss (HBT) and Ridge effects, as well as trying out a more sophisticated particle emission scenario: chemical freeze-out, along with continuous emission, transport model. At last, but not least, the effects of shear and bulk viscosities should be assessed.

Appendix A

Energy-momentum Tensor in any Reference Frame

The Lorentz transformation for a tensor is given by equation (2.9), $T^{\mu\nu} = \Lambda^\mu_\alpha \Lambda^\nu_\beta T_{RF}^{\alpha\beta}$ or, explicitly:

$$\begin{aligned} T^{00} &= \Lambda^0_0 \Lambda^0_0 T_{RF}^{00} + \Lambda^0_i \Lambda^0_j T_{RF}^{ij} \\ T^{i0} &= T^{0i} = \Lambda^0_0 \Lambda^i_0 T_{RF}^{00} + \Lambda^0_j \Lambda^i_k T_{RF}^{jk} \\ T^{ji} &= T^{ij} = \Lambda^i_0 \Lambda^j_0 T_{RF}^{00} + \Lambda^i_k \Lambda^j_l T_{RF}^{kl} \end{aligned} \quad (\text{A.1})$$

Considering the set of equations (2.5) and relation (2.8), the components above should be written as:

$$\begin{aligned} T^{00} &= \gamma^2 \epsilon + \gamma^2 v^2 P \\ T^{0i} &= \gamma^2 v^i \epsilon + \gamma v^k \left[\delta^{ik} + v^i v^k \frac{(\gamma - 1)}{v^2} \right] P \\ T^{ij} &= \gamma v^i \gamma v^j \epsilon + \left[\delta^{ik} + v^i v^k \frac{(\gamma - 1)}{v^2} \right] \left[\delta^{jk} + v^j v^k \frac{(\gamma - 1)}{v^2} \right] P \end{aligned} \quad (\text{A.2})$$

Knowing that $\frac{v^i v^k}{v^2} = \delta^{ik}$,

$$\begin{aligned} \Rightarrow T^{0i} &= \gamma^2 v^i \epsilon + \gamma v^k \delta^{ik} (1 + \gamma - 1) P = \gamma^2 v^i \epsilon + \gamma^2 v^i P = (\epsilon + P) \gamma^2 v^i \\ \Rightarrow T^{ij} &= \gamma^2 v^i v^j \epsilon + \delta^{ik} \gamma \delta^{jk} \gamma P = \gamma^2 v^i v^j \epsilon + \gamma^2 \delta^{ij} P \end{aligned}$$

Using $\gamma^2 - 1 = \gamma^2 \vec{v}^2$, one can manipulate T^{00} and T^{ij} :

$$\begin{aligned} \Rightarrow T^{00} &= \gamma^2 \epsilon + (\gamma^2 - 1) P = (\epsilon + P) \gamma^2 - P \\ \Rightarrow T^{ij} &= \gamma^2 v^i v^j \epsilon + \gamma^2 \delta^{ij} P + \delta^{ij} P \delta^{ij} P = \gamma^2 v^i v^j \epsilon + \delta^{ij} P + \delta^{ij} P (\gamma^2 - 1) \\ &= \gamma^2 v^i v^j \epsilon + \delta^{ij} P + P \gamma^2 \delta^{ij} v^2 = \gamma^2 v^i v^j \epsilon + \delta^{ij} P + \gamma^2 P v^i v^j \\ \Rightarrow T^{ij} &= (\epsilon + P) \gamma^2 v^i v^j + P \delta^{ij} \end{aligned}$$

Furthermore, $u^\mu = (u^0, \vec{u}) = \gamma(1, \vec{v})$. Thus,

$$\begin{aligned}
T^{00} &= (\epsilon + P)u^0u^0P \\
T^{0i} &= (\epsilon + P)u^0u^i \\
T^{ij} &= (\epsilon + P)u^iu^j + \delta^{ij}P
\end{aligned}
\tag{A.3}$$

Since $\eta^{\mu\nu} = \text{diag}(1, -1, -1, -1)$, one may write:

$$T^{\mu\nu} = (\epsilon + P)u^\mu u^\nu - P\eta^{\mu\nu} \tag{A.4}$$

Which is equation (2.10), the energy-momentum tensor for an ideal fluid in any inertial reference frame.

Appendix B

Coordinates in Heavy-Ion Collisions

The incident nuclei collide at $z = t = 0$ and we choose z as the collision axis. The hydrodynamic evolution follows, starting at a proper initial time, τ_0 . Particles are created around $z = t = 0$ and are supposed to travel with longitudinal velocity $v_z = z/t$. This prescription is boost invariant in the sense that for any Lorentz transformation along the z axis, the relationship still holds [12, 63]. Since all particles at a given z have the same speed, v_z , that is also the fluid velocity.

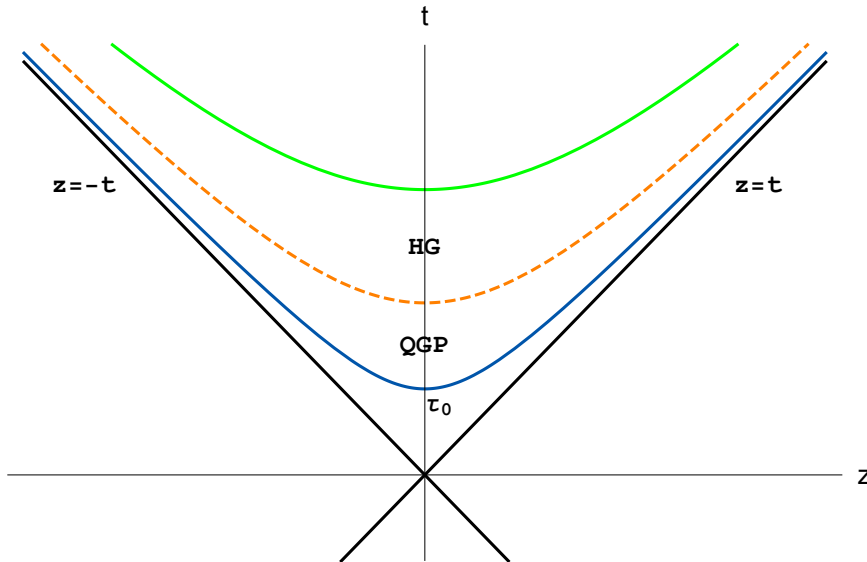


Figure B.1: Space-time diagram of the longitudinal evolution of the collision. The black lines ($z = t$ and $z = -t$) correspond to the nuclei trajectories, while the blue hyperbola represents the initial proper-time τ_0 . Dashed hyperbola illustrates the transition from QGP to HG and the green one is the end of the hydrodynamic expansion.

The beginning of the hydrodynamic expansion is delimited by the $\tau_0 = \sqrt{t^2 - z^2}$ hyperbola. As the value of proper-time changes, the stage of evolution corresponding to it will be represented in Fig.B.1 as another hyperbola, whose equation is $\tau = \sqrt{t^2 - z^2}$. In addition to proper time τ , we introduce η_s , defined as space-time rapidity:

$$t = \tau \cosh(\eta_s) \tag{B.1}$$

$$z = \tau \sinh(\eta_s) \tag{B.2}$$

When dividing (B.2) by (B.1), one should find an expression of η_s in terms of z and t .

$$\frac{z}{t} = \frac{\sinh(\eta_s)}{\cosh(\eta_s)} = \tanh(\eta_s)$$

Since $\tanh(\eta_s) = \frac{e^{\eta_s} - e^{-\eta_s}}{e^{\eta_s} + e^{-\eta_s}}$:

$$\frac{e^{\eta_s} - e^{-\eta_s}}{e^{\eta_s} + e^{-\eta_s}} = \frac{z}{t}$$

Consequently:

$$\begin{aligned} z(e^{\eta_s} + e^{-\eta_s}) &= t(e^{\eta_s} - e^{-\eta_s}) \\ e^{\eta_s}(t - z) &= e^{-\eta_s}(z + t) \\ \Rightarrow e^{2\eta_s} &= \left(\frac{t + z}{t - z}\right) \end{aligned}$$

Taking the natural logarithm on both sides:

$$\eta_s = \frac{1}{2} \ln \left(\frac{t + z}{t - z} \right) \tag{B.3}$$

Under a Lorentz boost in the z direction, τ is invariant and η_s is shifted by a constant (similarly to the particle rapidity). Alongside with $\tau = \sqrt{t^2 - z^2}$ and Cartesian coordinates x and y in the transverse plane, they are the variables used to depict the evolution of a heavy-ion collision.

Appendix C

Relativistic Fluid's Action in a General Coordinate System

Take a general coordinate system with

$$ds^2 = g_{\mu\nu} dx^\mu dx^\nu.$$

Under a general transformation, $x \rightarrow x'$, the hypervolume element becomes

$$d^4x'^\mu = \left\| \frac{\partial x'^\alpha}{\partial x^\beta} \right\| d^4x^\mu,$$

where $\left\| \frac{\partial x'^\alpha}{\partial x^\beta} \right\|$ is the Jacobian (J_β^α) determinant of the coordinate transformation[64]. Additionally, the metric tensor $g_{\mu\nu}$ may have the following expression:

$$\begin{aligned} g_{\mu\nu} &= \frac{\partial x'^\alpha}{\partial x^\mu} \frac{\partial x'^\beta}{\partial x^\nu} \eta_{\alpha\beta} \\ &= J_\mu^\alpha J_\nu^\beta \eta_{\alpha\beta} \end{aligned} \tag{C.1}$$

or, in matrix language, $(g_{\mu\nu}) = J^T \eta J$. If g is the determinant of 4×4 matrix $(g_{\mu\nu})$, one shall have $g = -(\det J)^2 \Rightarrow \det J = \sqrt{-g}$. Hence,

$$d^4x'^\mu = \sqrt{-g} d^4x^\mu, \tag{C.2}$$

which gives the general action

$$I = \int \mathcal{L} \sqrt{-g} d^4x, \tag{C.3}$$

where \mathcal{L} is a scalar Lagrangian density and $\sqrt{-g} d^4x$ is invariant.

We now proceed on presenting the covariant derivative of some contravariant vector V^μ , defined as

$$V^\mu_{;\nu} \equiv \frac{\partial V^\mu}{\partial x^\nu} + \Gamma^\mu_{\nu\alpha} V^\alpha, \tag{C.4}$$

from which we may derive the divergence, $V^\mu_{;\mu}$:

$$V^\mu_{;\mu} = \partial_\nu V^\mu + \Gamma^\mu_{\mu\alpha} V^\alpha. \tag{C.5}$$

The coefficients $\Gamma_{\nu\alpha}^{\mu}$ are known as components of the *affine connection* or as *Christoffel symbols* and can be written in terms of the metric tensor:

$$\Gamma_{\nu\alpha}^{\mu} = \frac{1}{2}g^{\sigma\mu} \left[\frac{\partial g_{\alpha\sigma}}{\partial x^{\nu}} + \frac{\partial g_{\nu\sigma}}{\partial x^{\alpha}} - \frac{\partial g_{\alpha\nu}}{\partial x^{\sigma}} \right], \quad (\text{C.6})$$

where

$$\begin{aligned} \Gamma_{\mu\alpha}^{\mu} &= \frac{1}{2}g^{\sigma\mu} [\partial_{\mu}g_{\alpha\sigma} + \partial_{\alpha}g_{\mu\sigma} - \partial_{\sigma}g_{\alpha\mu}] \\ &= \frac{1}{2}g^{\sigma\mu}\partial_{\alpha}g_{\mu\sigma}. \end{aligned}$$

Knowing that $\text{Tr}[M^{-1}\partial_{\lambda}M] = \partial_{\lambda}[\ln(\det M)]$ for an arbitrary matrix M ,

$$\Gamma_{\mu\alpha}^{\mu} = \frac{1}{2}\partial_{\alpha}\ln g = \frac{1}{\sqrt{-g}}\partial_{\alpha}\sqrt{-g}. \quad (\text{C.7})$$

Substituting the previous expression in (C.5) shall yield:

$$\begin{aligned} V^{\mu}_{;\mu} &= \partial_{\nu}V^{\mu} + \frac{1}{\sqrt{-g}}\partial_{\alpha}(\sqrt{-g})V^{\alpha} \\ &= \frac{1}{\sqrt{-g}}\partial_{\alpha}(\sqrt{-g}V^{\alpha}). \end{aligned} \quad (\text{C.8})$$

The Lagrangian for a relativistic fluid in motion can be taken as $L = -E$ [65], where E is the fluid's rest energy. Using (C.3) and $L = \int d^3x\mathcal{L}$ yields the action

$$I = - \int d^4x\sqrt{-g}\epsilon, \quad (\text{C.9})$$

where ϵ is the density distribution associated to E , such that $E = \int d^3x\epsilon$. From (C.8), we have the general forms for the constraints $\partial_{\mu}(su^{\mu}) = 0$ and $\partial_{\mu}(nu^{\mu}) = 0$ presented in Section 2.1:

$$(su^{\mu})_{;\mu} = \frac{1}{\sqrt{-g}}\partial_{\mu}(\sqrt{-g}su^{\mu}) = 0, \quad (\text{C.10})$$

$$(nu^{\mu})_{;\mu} = \frac{1}{\sqrt{-g}}\partial_{\mu}(\sqrt{-g}nu^{\mu}) = 0. \quad (\text{C.11})$$

References

- [1] CERN Press Release Feb. 10, (2000) <http://press-archive.web.cern.ch/press-archive/PressReleases/Releases2000/PR01.00EQuarkGluonMatter.html>;
- [2] Brookhaven National Laboratory, *Hunting the Quark Gluon Plasma (QGP) Formal Report - Results from the first 3 years at RHIC, Assessments by the experimental collaborations* (2005);
- [3] E. Fermi, *Prog. Theor. Phys.* **5**, 570 (1950);
- [4] L. D. Landau, *Izv. Akad. Nauk. SSSR Ser. Fiz.* **17**, 51 (1953);
- [5] S. Z. Belenkij, and L. D. Landau, *Usp. Fiz. Nauk* **56**, 309 (1955), from “Collected papers of L. D. Landau” (ed. D. Ter-Haar, Pergamon, Oxford, 1965) p. 665;
- [6] H. J. Drescher, F.M. Liu, S. Ostapchenko, T. Pierog, and K. Werner, *Phys. Rev. C* **65**, 054902 (2002);
- [7] C. E. Aguiar, T. Kodama, T. Osada, and Y. Hama, *J. Phys. G* **27**, 75 (2001);
- [8] T. Kodama, C. E. Aguiar, T. Osada, and Y. Hama, *J. Phys. G: Nucl. Part. Phys.* **27** (2001) 557-560;
- [9] P. Kovtun, *J. Phys. A: Math. Theor.* **45** (2012) 473001 [arXiv:hep-th/1205.5040];
- [10] L. D. Landau, and E. M. Lifshitz, *Fluid Mechanics*, ed. Pergamon Press (1987);
- [11] Lecture notes from the course *Fluidos Dissipativos Relativísticos e suas Recentes Aplicações em Física de Altas Energias - PGF5293-1/1*, Prof. Jorge Noronha (2013);
- [12] J.-Y. Ollitrault, *Eur.J.Phys.* **29**: 275-302 (2008) [arXiv:nucl-th/0708.2433];
- [13] S. Weinberg, *Gravitation and Cosmology: Principles and Applications of the General Theory of Relativity*, ed. John Wiley & Sons, Inc. (1972);
- [14] W. Florkowski, *Phenomenology of Ultra-Relativistic Heavy-Ion Collisions*, ed. World Scientific (2010);
- [15] S. Jeon, and U. Heinz, [arXiv:hep-ph/1503.03931] (2015);
- [16] Y. Hama, T. Kodama, and O. Socolowski Jr., *Brazilian Journal of Physics*, vol. **35**, no.1, p. 24 (2005);
- [17] B. Alver, and G. Roland, *Phys.Rev. C* **81**, 054905 (2010) [arXiv:nucl-th/1003.0194];

- [18] B. Alver, C. Gombeaud, M. Luzum, and J.-Y. Ollitrault, *Phys.Rev. C* **82**, 034913 (2010) [arXiv:nucl-th/1007.5469];
- [19] C. Gale, S. Jeon, B. Schenke, P. Tribedy, and R. Venugopalan, [arXiv:hep-ph/1210.5144] (2012);
- [20] B. Schenke, and R. Venugopalan, *Phys. Rev. Lett.* **113**, 102301 (2014) [arXiv:nucl-th/1405.3605];
- [21] G. Denicol, C. Gale, S. Jeon, J.-F. Paquet, and B. Schenke, [arXiv:nucl-th/1406.7792] (2014);
- [22] C. Shen, Z. Qiu, and U. Heinz, *Phys. Rev. C* **92**, 014901 (2015) [arXiv:nucl-th/1502.04636];
- [23] F. Gardim, F. Grassi, M. Luzum, and J.-Y. Ollitrault, *Phys. Rev. C* **87**, 031901(R) (2013) [arXiv:nucl-th/1211.0989];
- [24] J. Takahashi et al., *Phys. Rev. Lett.* **103**, 242301 (2009);
- [25] R. Andrade, F. Grassi, Y. Hama, W.-L. Qian, *Physics Letters B*, v. **712**, p. 226-230, (2012) [arXiv:nucl-th/1008.4612];
- [26] Y. Hama, R. P. G. Andrade, F. Grassi, O. Socolowsky Jr., T. Kodama, B. Tavares, and S. S. Padula, *Nucl.Phys. A* **774**, 169 (2006);
- [27] P. Huovinen, P. Petreczky, *Nucl.Phys. A* **837**, 26 (2010) [arXiv:hep-ph/0912.2541];
- [28] E. Megías, E. R. Arriola, and L. L. Salcedo, *Nucl. Phys. Proc. Suppl.* **234**, 313-316 (2013) [arXiv:hep-ph/1207.7287];
- [29] S. R. A. Salinas, *Introduction to Statistical Physics*, ed. Springer (2001);
- [30] A. Chodos, R. L. Jaffe, K. Johnson, C. B. Thorn, and V. F. Weisskopf, *Phys. Rev. D* **9**, 3471-95 (1974);
- [31] A. Chodos, R. L. Jaffe, K. Johnson, and C. B. Thorn, *Phys. Rev. D* **10**, 2599 (1974);
- [32] Z. Fodor and S. D. Katz, *JHEP* 0203, 014 (2002) [arXiv:hep-lat/0106002];
- [33] J. Casalderrey-Solana, H. Liu, D. Mateos, K. Rajagopal, and U. A. Wiedemann, [arXiv:hep-th/1101.0618] (2012);
- [34] K. Rajagopal, and F. Wilczek, [arXiv:hep-ph/0011333] (2000);
- [35] P. Petreczky, *Nucl. Phys. A* **830**, 11c-18c (2009) [arXiv:hep-ph/0908.1917];
- [36] P. Huovinen, P. Petreczky, and C. Schmidt, [arXiv:nucl-th/1407.8532] (2014);
- [37] F. Cooper, and G. Frye, *Phys. Rev. D* **10**, 186 (1974);
- [38] F. Debbasch, J.P. Rivet, and W.A. van Leeuwen, *Physica A* **301**, 181 (2001) [arXiv:astro-ph/0707.2499];
- [39] D. H. Rischke, [arXiv:nucl-th/9809044] (1998);

- [40] PhD Thesis: *Sobre a evolução hidrodinâmica da matéria nuclear criada em colisões de íons pesados relativísticos - um estudo com condições iniciais flutuantes*, Universidade de São Paulo (2011), R. P. G. Andrade;
- [41] L. B. Lucy, *Astrophys. J.* **82**, 1013 (1977);
- [42] R. A. Gingold and J. J. Monaghan, *Mon. Not. R. Astro. Soc.* **181**, 375 (1977);
- [43] J. Noronha-Hostler, J. Noronha, and F. Grassi, *Phys. Rev. C* **90**, 034907 (2014);
- [44] C. Aguiar, T. Kodama, Y. Hama, and T. Osada, *Nucl. Phys. A* **698** (2002) 639c, [arXiv:nucl-th/0102011];
- [45] ALICE Collaboration, *Phys. Rev. C* **88**, 044909 (2013) [arXiv:nucl-ex/1301.4361];
- [46] ALICE Collaboration, *Phys. Lett. B* **726**, 610-622 (2013) [arXiv:nucl-ex/1304.0347];
- [47] ALICE Collaboration, *Phys. Lett. B* **720**, 52-62 (2013) [arXiv:hep-ex/1208.2711];
- [48] J.-Y. Ollitrault, *Phys. Rev. D* **46**, 229 (1991);
- [49] A. M. Poskanzer, and S. A. Voloshin, *Phys. Rev. C* **58**, 1671 (1998) [arXiv:nucl-ex/9805001];
- [50] F. G. Gardim, F. Grassi, Y. Hama, M. Luzum, and J.-Y. Ollitrault, *Phys. Rev. C* **83**, 064901 (2011) [arXiv:nucl-th/1103.4605];
- [51] CMS Collaboration, *Phys. Rev. C* **87**, 014902 (2013) [arXiv:nucl-ex/1204.1409];
- [52] CMS Collaboration, *Phys. Rev. C* **89**, 044906 (2014) [arXiv:nucl-ex/1310.8651];
- [53] ATLAS Collaboration, *JHEP* **11**, 183 (2013) [arXiv:hep-ex/1305.2942];
- [54] J. Noronha-Hostler, G. S. Denicol, J. Noronha, R. P. G. Andrade, and F. Grassi, *Phys. Rev. C* **88**, 044916 (2013) [arXiv:nucl-th/1305.1981] (2013);
- [55] N. Borghini, P. M. Dinh, and J.-Y. Ollitrault, *Phys. Rev. C* **64**, 054901 (2001) [arXiv:nucl-th/010540];
- [56] R. S. Bhalerao, N. Borghini, and J.-Y. Ollitrault, *Nucl. Phys. A* **727**, 373 (2003);
- [57] N. Borghini, R. S. Bhalerao, and J.-Y. Ollitrault, *J. of Phys. G* **30**, S1213 (2004);
- [58] C. Gale, S. Jeon, B. Schenke, P. Tribedy, and R. Venugopalan, [arXiv:nucl-th/1209.6330] (2012);
- [59] B. B. Back et al., *Braz. J. Phys.* **34**, 829 (2004);
- [60] PhD thesis: *Efeitos da equação de estado em hidrodinâmica relativística através de alguns observáveis*, Instituto de Física Teórica - Universidade Estadual Paulista (2014), D. M. Dudek;
- [61] B. B. Back et al. [PHOBOS Collaboration], *Phys. Rev. B* **578**, 297 (2004);
- [62] F. G. Gardim, F. Grassi, M. Luzum, and J.-Y. Ollitrault, *Phys. Rev. Lett.* **109**, 202302 (2012) [arXiv:nucl-th/1203.2882];

- [63] J. D. Bjorken, *Phys. Rev. D* **27**, 140 (1983);
- [64] J. A. Peacock, *Cosmological Physics*, Cambridge University Press (1999);
- [65] H. T. Elze, Y. Hama, T. Kodama, M. Makler, and J. Rafelski, [arXiv:hep-ph/9809570] (1998);